

**Red Blood Cell Trans-Dispersion Revealing Biophysical Signatures in Malaria  
Parasitism**

by

Aline Teresa Santoso

B.A.Sc., University of Waterloo, 2012

A THESIS SUBMITTED IN PARTIAL FULFILLMENT OF  
THE REQUIREMENTS FOR THE DEGREE OF

MASTER OF APPLIED SCIENCE

in

The Faculty of Graduate and Postdoctoral Studies

(Mechanical Engineering)

THE UNIVERSITY OF BRITISH COLUMBIA

(Vancouver)

May 2015

© Aline Teresa Santoso, 2015

## Abstract

Red blood cell (RBC) deformability plays an important role in the pathogenesis of *Plasmodium falciparum* malaria, and therefore could potentially enable simple, rapid, and reagent-free biophysical assays. A key challenge, however, is that pathological cells often only represent a small fraction of the sample, which requires testing a large number of individual cells to enable their detection. Additionally, it is often desirable to perform multiple assays simultaneously, which require technologies capable of parallelized analysis. Traditional technologies for analyzing RBC deformability are limited by their experimental difficulty, extensive instrumentation requirements, as well as their lack of throughput and parallelizability. Here, a new microfluidic mechanism called trans-dispersion is developed to address these issues, enabling a high-throughput and parallelized analysis of RBC deformability.

The trans-dispersion mechanism transports single RBCs through a series of constrictions in a microfluidic channel, where their transit speed is a function of their deformability. This process is analogous to gel-electrophoresis, where the migration speed of molecules depends on their length. To ensure a sensitive and consistent measurement, the geometry of the constriction is sized such that the transiting cell forms a temporary seal with each constriction while supporting microchannels ensure consistent forces are applied to each deformation channel. After undergoing repeated deformations, the final position of each RBC, indicating its deformability, is determined using simple bright-field microscopy and automated image processing, and thereby resulting in a repeatable, high-throughput and parallelized process. The performance of this mechanism was evaluated by detecting changes in RBC deformability resulting from chemical degradation, malaria parasitism and exposure to anti-malarial drugs. This device can distinguish variation in RBC deformability following chemical degradation using small concentrations (0.0005%) of glutaraldehyde (GTA). *P. falciparum*-infected RBCs (iRBCs) show distinct deformability curves compared to the uninfected controls. The linear correlation between the parasitemia and the percentage of non-transiting cells could potentially be used to infer the parasitemia of clinical specimen. Furthermore, this device was able to simultaneously assess the efficacy of several antimalarial compounds; showing that rigidification of *P. falciparum*-iRBCs can potentially be used to evaluate antimalarial drug efficacy, as well as serve as a functional screen for new antimalarials.

## **Preface**

A version of Chapter 2, Chapter 4 and Chapter 5 are part of a manuscript currently in preparation: *A. Santoso, X. Deng<sup>a</sup> J. H. Lee, K. Matthews, E. Islamzada, S. McFaul, M-E. Myrand-Lapierre, M. Scott and H. Ma. Cell-phoresis of Red Blood Cells Revealing Biophysical Signatures in Malaria Parasitism.*

The mechanism described in Chapter 2 was originally developed by Quan Guo and Marie-Eve Myrand-Lapierre. Here, I adapted and improved the mechanism for high throughput measurement of red blood cell deformability associated with malaria parasitism. I conducted the majority of the experiments and wrote the majority of the manuscript. Dr. Hongshen Ma and Kerryn Matthews proofread the manuscript.

The silicon masters were fabricated with the help of Marie-Eve Myrand Lapierre and Jeong Hyun Lee. Emel Islamzada and Han Yuan helped in carrying out the soft lithography process of the microfluidic device. Richard Ross Ang developed the software to analyze the funnel pore size and Jeong Hyun Lee developed the image processing software in section 3.4. Xiaoyan Deng helped me in culturing the malaria parasites.

This work is approved by UBC Research Ethics Board under H10-01243 “Blood Collection for Microfluidic Cell Biomechanics and Cell Separation”.

## Table of Contents

Abstract.....	ii
Preface.....	iii
Table of Contents.....	iv
List of Tables .....	vii
List of Figures.....	viii
List of Abbreviations .....	xiii
Acknowledgements.....	xiv
Dedication.....	xv
Chapter 1: Introduction.....	1
1.1 Malaria .....	2
1.2 Review of previous techniques .....	5
1.2.1 Traditional techniques.....	5
1.2.2 Microfluidic techniques .....	7
1.3 Design concept and research goals.....	11
Chapter 2: Device Principle, Design and Operation.....	13
2.1 Fluidic plunger mechanism .....	14
2.2 Functional requirements for the trans-dispersion mechanism.....	16
2.2.1 Motivation.....	16
2.2.2 Constraints and challenges.....	17
2.3 Design of trans-dispersion device .....	21
2.3.1 Deformation microchannel .....	22
2.3.2 Loading microchannels.....	24
2.3.3 Bypass microchannels.....	26
2.3.4 Pressure attenuator .....	28

2.3.5	Optimization of the multiplexed trans-dispersion device .....	28
2.4	Device operation .....	30
2.4.1	Measurement process.....	30
2.4.2	Applied pressure waveform .....	30
2.4.3	Manifold to multiplex array .....	32
2.5	Device prototypes based on target cells .....	32
2.6	Relationship to previous work .....	33
Chapter 3:	Material and Methods .....	35
3.1	Fabrication of silicon masters/photolithography.....	35
3.2	Fabrication of PDMS devices/soft-lithography .....	37
3.3	Sample preparation.....	38
3.3.1	Healthy RBCs .....	38
3.3.2	Oxidatively damaged RBCs.....	39
3.3.3	Culture and synchronization of <i>P. falciparum</i> malaria.....	39
3.3.4	Purification of <i>P. falciparum</i> -infected RBCs and drug treatment .....	40
3.4	Experimental setup and protocol.....	41
3.5	Data analysis .....	45
3.6	Statistical analysis .....	46
Chapter 4:	Device Characterization.....	47
4.1	Direction of fluid flow.....	47
4.2	Healthy RBCs.....	48
4.3	Repeated deformations.....	49
4.4	Optimization of applied pressure waveform .....	50
4.5	Multiplexing error .....	53
4.6	Sensitivity.....	54

4.7	Throughput .....	55
Chapter 5: Biological Applications .....		56
5.1	<i>P. falciparum</i> -infected RBCs .....	56
5.1.1	Unsynchronized samples .....	56
5.1.2	Ring-stage synchronized sample.....	59
5.1.3	Non-transiting cells.....	60
5.2	Antimalarial drug response .....	61
5.3	Discussion .....	63
Chapter 6: Summary and Conclusions .....		66
6.1	Summary of thesis.....	66
6.2	Future work .....	67
References:.....		68

## List of Tables

Table 1-1: Traditional techniques used to measure RBC deformability. Deformability parameters are described in: Elongation Index EI; Deformability Index DI; Shear Modulus $\mu$ ; Young's Modulus E).....	6
Table 2-1: Natural variability (NV) between RBCs of the same sample, where NV is defined as the percentage uncertainty of the sample (standard deviation/mean). ....	25
Table 2-2: Differences in deformability due to disease pathology between healthy and diseased samples in different biological systems where PV is defined as the percentage difference between these two states. ....	25
Table 2-3: Details of device geometries based on the target cells.....	33
Table 3-1: Spin speed settings of SU8 photoresists to produce the desired layer thickness .....	37
Table 3-2: Summary of data analysis process for each experiment.....	46
Table 5-1: Individual concentrations and normalized deformability values for various antimalarial drug treatments (n = 616 for control and n $\geq$ 100 for iRBCs). ....	63

## List of Figures

Figure 1-1: Graphic representation of human and murine RBCs and the sizes of microcapillaries and inter-endothelial clefts of the spleen [6].....	1
Figure 1-2: Development of <i>P. falciparum</i> in human RBCs over 48 hours [18].....	3
Figure 1-3: (1) Normal RBCs. (2-18) Trophozoites (among these, 2-10 show ring-stage trophozoites). (19-26) Schizonts. Adapted from Coatney GR, Collins WE, Warren M, Contacos PG. The Primate Malaria. U.S. Department of Health, Education and Welfare, Bethesda, 1971.	3
Figure 1-4: (A) Histogram and (B) bar graph showing that <i>Plasmodium falciparum</i> iRBCs stiffen as parasites mature, adapted from Quan Guo's work [21].....	4
Figure 1-5: Wedged RBCs in tapered constrictions. RBCs move to different locations based on their deformability [9].....	8
Figure 1-6: (A) Deformability-based flow cytometer with triangular pillar arrays [42]. (B) Schematic of microfluidic system for electrical and mechanical characterization of RBCs [43].	9
Figure 1-7: (A) Overview of the transit pressure device developed by Guo <i>et al.</i> [45] (B) Magnified view of the row of constrictions. (C) Geometric representation of a RBC deforming through a funnel constriction. (D) Multiplexed version of the transit pressure device [46].....	10
Figure 2-1: The trans-dispersion mechanism. Position of the cells along the device is indicative of their transit speed and hence, their deformability. More deformable cells will travel further along the device than less deformable cells.....	13
Figure 2-2: Top and side sections of (A) a RBC at rest and (B) a RBC deforming through a microscale constriction [50].....	14
Figure 2-3: Fluidic plunger mechanism (A) The applied pressure is distributed across the microchannel when the cell is not deformed through the constriction [46]. (B) The applied pressure focuses across the cell when the cell is deformed through the constriction. (C) When a	

constant pressure is applied, the position of the cell along the funnel (insert) shows that the cell acts as a temporary seal against the constriction as it being deformed.....	15
Figure 2-4: Micrograph of a zoomed-in section of the trans-dispersion device, showing $N_F$ individual funnels (blue box) connected in series to form $N$ parallel deformation microchannels (red box) (scale bar = 75 $\mu\text{m}$ ). .....	17
Figure 2-5: Graphic representation of fluid streamlines in the loading and deformation microchannels and its associated hydrodynamic circuit when: (A) All deformation microchannels are unoccupied with cells and (B) only one deformation microchannel is unoccupied. ....	19
Figure 2-6: (A) Structure and components of the multiplexed trans-dispersion mechanism with individual RBCs loading into the deformation microchannels. (B) An equivalent hydrodynamic circuit of the multiplexed trans-dispersion mechanism. (C) Detailed design of deformation microchannel.....	22
Figure 2-7: (A) Pressure in the two loading microchannels ( $P_L$ ) as a function of distance. (B) Hydrodynamic circuit illustrating the principle of pressure attenuation. ....	26
Figure 2-8: (A) Pressure waveform applied across the device. (B) The trans-dispersion chip with 8 parallel trans-dispersion arrays. (C) 3D model of the trans-dispersion array. (D) Cross-section of the device showing the geometry of bypass, loading and deformation microchannel. (E) Detailed design of the deformation microchannel, where $N_F$ is the number of constrictions and $W$ is the constriction diameter. A two-stage device will have different pore size where $W_{0,1}$ is greater than $W_{0,2}$ .....	31
Figure 3-1: Schematic of the photolithography process .....	35
Figure 3-2: Schematic of the soft lithography process. ....	38
Figure 3-3: Illustration of the RBC pellet after centrifugation. ....	40
Figure 3-4: Magnetic purification of iRBCs to obtain late-stage iRBCs only.....	41

Figure 3-5: A photograph of the experimental system. The PC controls the pressure controller system and captures the final positions of the cells using the microscope and the camera. (1) Bandpass filter. (2) Photograph of the trans-dispersion device with manifold..... 42

Figure 3-6: Image processing software used to automatically detect RBCs. Red squares indicate automatic detection by the software while yellow squares indicate manual selection by the user. .... 44

Figure 3-7: Interface of the software used to measure the constriction size..... 45

Figure 4-1: Illustration of the two possible fluid flow directions in the deformation microchannel. .... 47

Figure 4-2: Correlation between the threshold pressure and the speed of each cell shows that forward flow produces a more consistent measurement of transit speed ( $r^2=0.66$ ,  $n=62$ ) than the reverse flow ( $r^2=0.24$ ,  $n=49$ )..... 48

Figure 4-3: Measured deformability of different donors shows variability between donors ( $n \geq 99$ ). .... 49

Figure 4-4: Constant speed is observed in 4 test parameters, which indicates the elastic properties of RBCs undergoing repeated deformations and the averaging effect of constriction geometry variations ( $n \geq 125$ ). Experiment is performed in triplicate with three different donors and each donor data is normalized to their corresponding 2 minutes at 100 mbar data point. .... 50

Figure 4-5: The applied pressure waveform is optimized by measuring the % difference between the mean-value of 0% and 0.0005% GTA-treated samples to maximize the sensitivity of the trans-dispersion mechanism ( $n \geq 102$ )..... 51

Figure 4-6: Shape of an RBC during deformation process: (A) at 75 mbar, the RBC goes back to its normal discoid shape after each deformation; (B) at 600 mbar, the RBC remains in its deformed, “bullet” shape, resulting in a loss of device capability to resolve the difference in RBC deformability..... 52

Figure 4-7: The optimized pressure waveform can be linearly extrapolated with the hydrodynamic resistance of the deformation microchannel since the normalized position of the cells linearly correlates with the resistance as shown in (A), when the applied pressure waveform is the same. The thickness of the deformation microchannel (B) is the dominant factor for its hydrodynamic resistance. However, the average pore size also changes the hydrodynamic resistance (C). ..... 53

Figure 4-8: Distribution of the measured position with the deformation microchannel array nearly empty (<10% occupancy, n = 281) and nearly full (>70% occupancy, n = 583), which shows no distinction (p=0.57). This triplicate sample was normalized based on the donor. .... 54

Figure 4-9: The sensitivity of all the trans-dispersion prototypes was evaluated with glutaraldehyde fixation using their individual optimized pressure waveform. Measured values are normalized to the mean of the control with n≥509 at each test condition (p<0.0001). ..... 55

Figure 5-1: The deformability patterns of RBCs parasitized with unsynchronized *P. falciparum*. Each sample is normalized to the mean of the control. The normalized mean of the sample decreases with increasing parasitemia level, with p<0.0001 for (\*) with respect to control (n=8575 for control and an n≥500 for 3% parasitemia level). (\*\*) was not significant. The mean and standard deviation was shown for each sample. .... 57

Figure 5-2: (A) The deformability profiles of RBCs parasitized with unsynchronized *P. falciparum* at increasing population fraction from least to most deformable. (B) Detailed deformability profile of (A) at 2% least deformable fraction shows significant difference between 0% and 0.2% parasitemia samples (p<0.0001). ..... 58

Figure 5-3: Deformability patterns of RBCs parasitized with synchronized *P. falciparum* at ring-stage show decreased mean normalized position occurring with increasing parasitemia level with p<0.0001 for (\*) (n=9074 for control and an n≥978 for 2% parasitemia level). (\*\*) and (\*\*\*) is significant with p=0.0053 and p =0.0479 respectively. .... 59

Figure 5-4: The deformability profiles of RBCs parasitized with ring-synchronized *P. falciparum* at increasing population fraction from least to most deformable. The detailed deformability

profile evaluated at 2% least deformable population (insert) shows a significance difference between 0% and 1% parasitemia samples ( $p < 0.0001$ )..... 60

Figure 5-5: A strong, positive correlation between parasitemia level and percentage of non-transiting cells is plotted at log-log scale ( $r^2 \geq 0.92$ ) and (insert) at linear scale. .... 61

Figure 5-6: Evaluating antimalarial drug efficacy. Antimalarial drug response ( $> 4 \times EC_{50}$ ) in late-stage RBC infected with *P. falciparum* parasites show decreased deformability for all antimalarial drugs ( $p < 0.0001$ ) except tetracycline ( $p = 0.54$ ) and DHIQ enantiomer, which is DHIQ negative control ( $p = 0.1$ ) with  $n \geq 100$  (for atovaquone) for all samples. .... 62

## **List of Abbreviations**

DNA = Deoxyribonucleic Acid

DHA = Dihydroartemisinin

DHIQ = Dihydroisoquinolone

GTA = Glutaraldehyde

PDMS = Polydimethylsiloxane

PBS = Phosphate Buffered Saline

RBCs = Red Blood Cells

iRBCs = infected Red Blood Cells

uRBCs = uninfected Red Blood Cells

SD = Standard Deviation

UV = Ultraviolet

## **Acknowledgements**

This project would not have been possible without the support of my family, friends and coworkers. In particular, I would like to offer my deepest gratitude

To my supervisor, Dr. Hongshen Ma for his continuous patience and support in guiding me through my study and research in UBC.

To my mentor Sarah McFaul and Marie-Eve Myrand Lapierre for sharing with me their knowledge in microfluidics and for answering my endless questions.

To Kerry, Xiaoyan, Xi, Quan, Chao, Richard and the rest of the members of the Multiscale Design Lab for their friendship and support in the lab.

To Dr. Karen C. Cheung and her students for their willingness to share the BioMEMS lab in AMPEL 146.

To my parents and sisters, whose love, trust and understanding helped me through this process.

*To my family*

*For their love and support*

## Chapter 1: Introduction

Normal human red blood cells (RBCs) are  $8\ \mu\text{m}$  in diameter but must squeeze through capillaries of less than half of their diameter, as well as through inter-endothelial clefts of the spleen and extrusion from the bone marrow measuring  $0.5 - 1.0\ \mu\text{m}$  in diameter (Figure 1-1) [1,2]. The extraordinary deformability of RBCs gives them the ability to repeatedly transit through the microvasculature of the human body and the loss of this capability leads to increased RBC destruction by the spleen [3]. Hence, the deformability of individual cells can be strongly coupled with the structure of the cell membrane, nucleus, and cytoskeleton [4,5], enabling this parameter to be used as a simple and quantitative evaluation of biological and morphological properties of the cell.

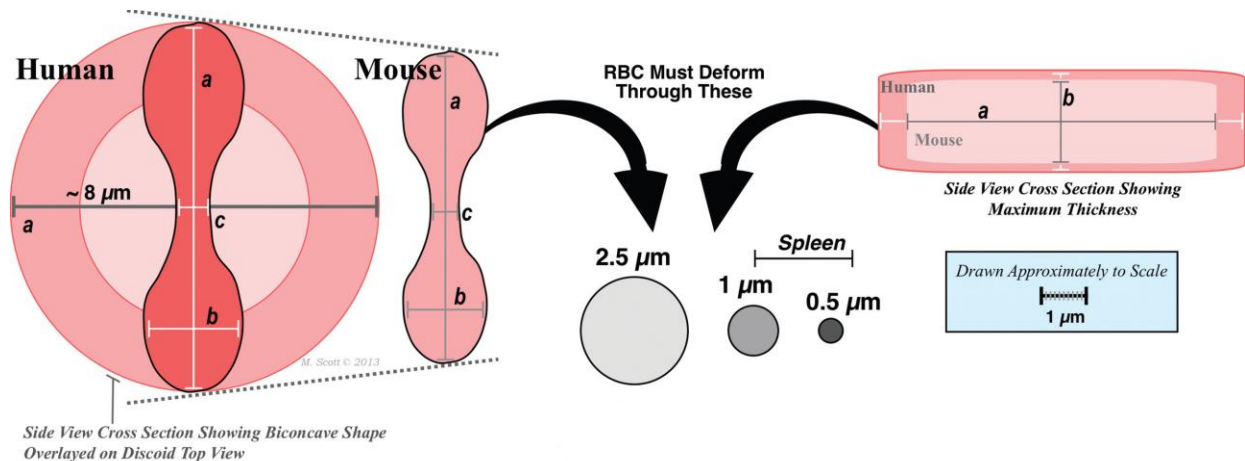


Figure 1-1: Graphic representation of human and murine RBCs and the sizes of microcapillaries and inter-endothelial clefts of the spleen [6].

Changes in red blood cell (RBC) deformability have been identified as a biomarker for the presence and status of a wide range of diseases including malaria [7–9], hemoglobinopathies [7,10,11] and micronutrient deficiencies [12–14] as well as for evaluating the efficacy of anti-malarial drugs [15]. The analysis of RBC deformability presents a potential tool for a simple, rapid, and label-free biophysical assay that can be used to analyze the status and severity of these diseases.

This thesis focuses on the development of a novel microfluidic mechanism to enable sensitive, high-throughput and massively parallel analysis of changes in cellular deformability

associated with malaria parasitism and anti-malarial drug treatments. We demonstrated that this device is able to consistently measure multiple individual RBCs independent of constriction position and occupancy while maintaining similar or better sensitivity compared to other techniques. This device has sufficient throughput and parallelizability to enable label-free biophysical detection of malaria infection, as well as a functional *in vitro* assay for antimalarial drug efficacy.

In this chapter, section 1.1 reviews the pathology of RBCs in malaria and discusses the current detection of this disease. Section 1.2 reviews the principle, operation and drawbacks of the current techniques to measure RBC deformability. Section 1.3 presents the device concepts and research goals of the thesis.

## 1.1 Malaria

Malaria, a disease that affects 500 million people worldwide and causes nearly 1-2 million annual deaths, is an important example of an infectious disease that dramatically decreases RBC deformability [16]. Malaria in humans is caused by five different protozoan parasites: *Plasmodium falciparum*, *Plasmodium vivax*, *Plasmodium malariae*, *Plasmodium ovale* and *Plasmodium knowlesi* [17]. Amongst these five parasites, *Plasmodium falciparum* is the most virulent and deadly human malaria parasite that causes the vast majority of infections.

The *P. falciparum* parasite is introduced into the human body via mosquito bite. It quickly travels to the liver where it infects hepatocytes, incubates and replicates for around 12 days, after which, the parasite is released into the circulation, where it invades and develops within RBCs. The malaria infected RBCs (iRBCs) transition through notable morphological changes from the ring-stage to the trophozoite and finally the schizont stage within 48 hours (Figure 1-2) [18]. Only ring-stage iRBCs are observed in the peripheral circulation of infected patients while mature-stage iRBCs (trophozoite and schizont) are sequestered in different organs. Ring-stage iRBCs include cells up to 24 hours post-infection (Figure 1-3).

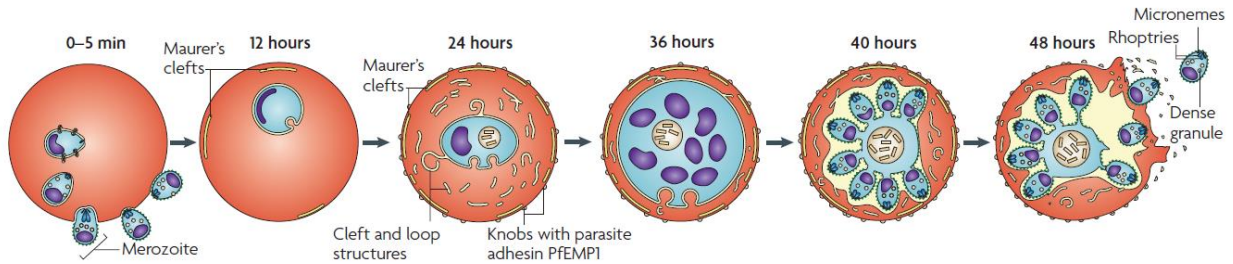


Figure 1-2: Development of *P. falciparum* in human RBCs over 48 hours [18].

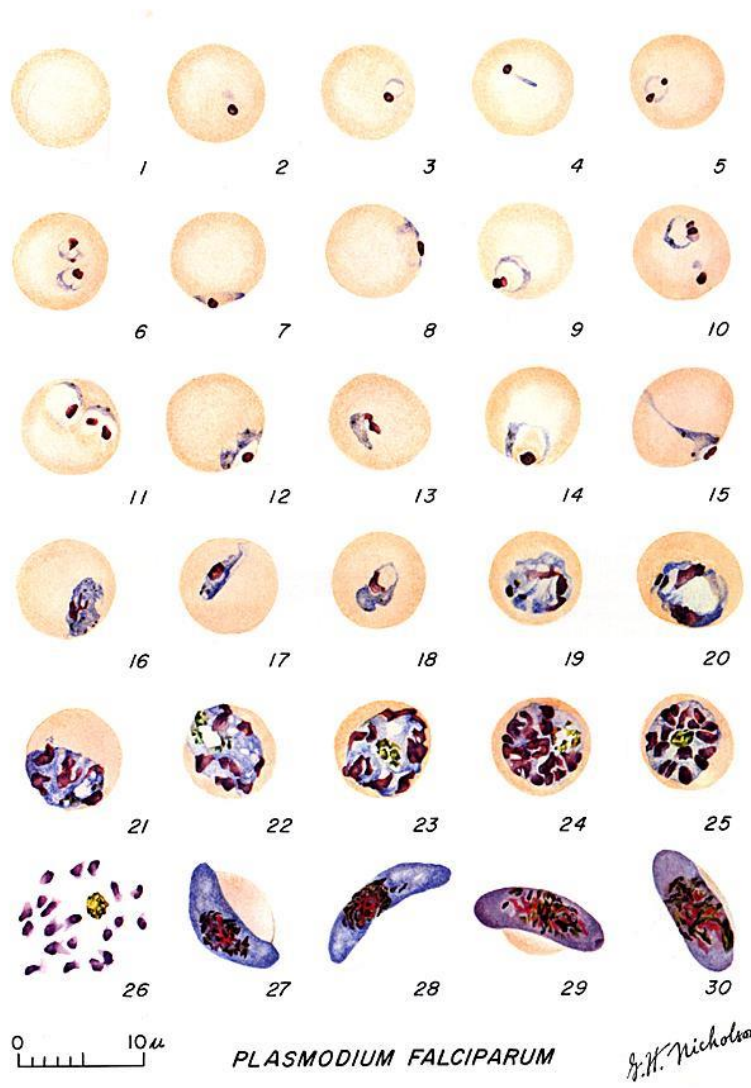


Figure 1-3: (1) Normal RBCs. (2-18) Trophozoites (among these, 2-10 show ring-stage trophozoites). (19-26) Schizonts. Adapted from Coatney GR, Collins WE, Warren M, Contacos PG. The Primate Malaras. U.S. Department of Health, Education and Welfare, Bethesda, 1971.

A key host response to *P. falciparum* infection is the rigidification of the iRBCs, which serves as an anti-malarial defense in early infection, enabling specific clearance of the iRBCs by the spleen [8,19]. In the ring-stage, decreased deformability of RBCs is caused primarily by two proteins: Ring-infected Erythrocyte Surface Antigen (RESA) and Knob-Associated His-Rich Protein (KHARP) [18]. RESA may stabilize the iRBC membrane against thermal shock while KHARP produces 100 nm-diameter knob-like protrusions that become the anchoring point for the membrane-embedded cytoadherence protein, *P. falciparum* Erythrocyte Membrane Protein 1 (PfEMP1). PfEMP1 is responsible for adhesion to endothelial cells [18], which is one of the mechanisms by which late-stage iRBCs evade clearance by the spleen. As the malaria parasite matures within RBCs, iRBCs become progressively stiffer [20] and as infection progresses, uninfected RBCs (uRBCs) also stiffen (Figure 1-4), which has been found to correlate with the onset of severe malaria [3].

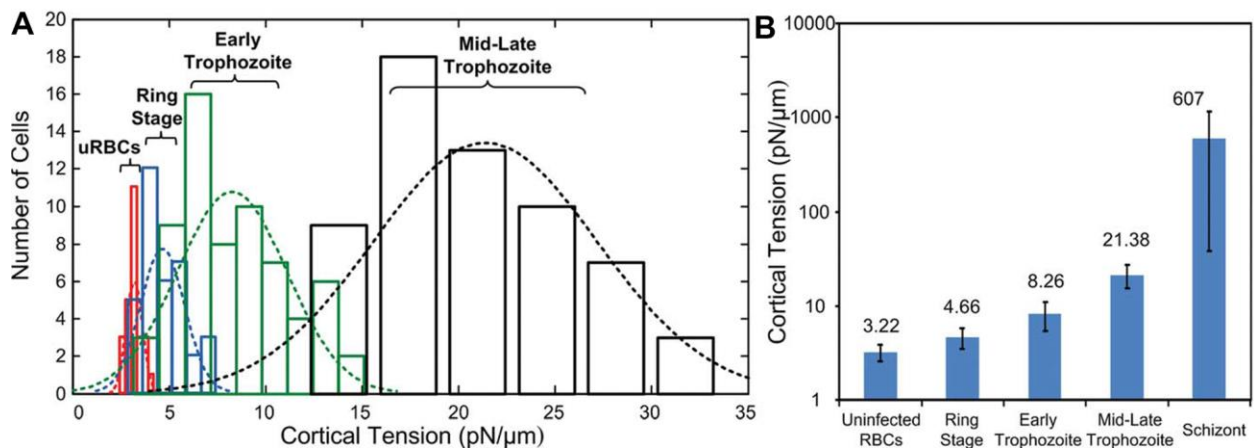


Figure 1-4: (A) Histogram and (B) bar graph showing that *Plasmodium falciparum* iRBCs stiffen as parasites mature, adapted from Quan Guo's work [21]

Currently, the gold standard for malaria detection is still microscopy analysis of Giemsa stained iRBCs fixed on a glass slide. Giemsa stain colors the chromatin in DNA purple and since RBCs do not contain DNA, uninfected RBCs remained red in color [22]. Even though this technique is very sensitive [23], this technique is time consuming and requires highly skilled technicians to count the large number of uninfected RBCs and to differentiate parasitized RBCs from other artefacts. Another conventional technique to detect malaria infection is the antigen-based Rapid Diagnostic Tests (RDTs), which works by detecting antigens, such as HRP-2, which is released by *P. falciparum*-iRBCs [24]. Even though RDTs are fast (< 20 minutes), this

technique does not detect the parasitemia level of the sample, which is key diagnostic information for patients with severe malaria infection. Furthermore, HRP-2 antigens have been known to persist in the blood circulation even after the parasites have been cleared from the host, resulting in false positive results [24–26]. Therefore, changes in RBC deformability in malaria infection is a promising alternative to providing a rapid, label-free, reagent-free and sensitive tool for the presence and status of malaria infection.

## **1.2 Review of previous techniques**

This section reviews the previous techniques for measuring RBC deformability. Traditional techniques such as ektacytometry [27–30], micropore filtration [31,32], micropipette aspiration (MPA) [33–35], atomic force microscope (AFM) [36,37] and optical tweezers [38–40] are reviewed briefly in this section. Recent microfluidic techniques involve deforming individual cells using mechanical structures such as wedging in tapered constriction [9] and measurement of transit time [41–43] or transit pressure [44–46] through micro-scaled constrictions.

### **1.2.1 Traditional techniques**

Traditional technologies used to measure RBC deformability are summarized in Table 1-1 and can be divided into bulk flow and single cell techniques. Bulk flow techniques, such as ektacytometry [27–30] and micropore filtration [31,32] provide a measure of the average deformability of the entire RBC population and hence, are not suitable in situations where the target cells constitute a small percentage of the cell population.

In ektacytometry, the deformability of a RBC population is expressed as the elongation index (EI), which is a measure of the shear-induced elongation of the RBC population. This technique requires expensive and specialized equipment to operate. Micropore filtration measures the time taken, expressed as the deformability index (DI), for a population of RBCs to pass through a membrane filter with a diameter smaller than the diameter of RBCs. One of the drawbacks of this technique is its tendency to clog due to the presence of other blood components such as white blood cells and platelets [47,48]. Furthermore, there is no mechanism to ensure consistent pressure difference is applied to each cell, resulting in a less accurate deformability measurement.

Table 1-1: Traditional techniques used to measure RBC deformability. Deformability parameters are described in: Elongation Index EI; Deformability Index DI; Shear Modulus  $\mu$ ; Young's Modulus E)

Category		Bulk-flow		Single-cell		
Technique		Ektacytometry	Micropore filtration	MPA	AFM	Optical Tweezer
Deformability Parameter		EI	DI	$\mu$	E	$\mu$
Cell Types		Stored RBCs	Sickled RBCs	Malaria iRBCs	RBCs	Thalassemic RBCs
Throughput (cells/hour) (Highest value reported)		Population of RBCs	Population of RBCs	40	20	40
<b>Drawbacks</b>	<b>General</b>	Only measures average deformability of RBC population		<ul style="list-style-type: none"> <li>• Time-consuming</li> <li>• Skilled technicians</li> <li>• Specialized equipment</li> <li>• Low throughput</li> </ul>		
	<b>Specific to Technique</b>	Specialized equipment	<ul style="list-style-type: none"> <li>• Clogging issue</li> <li>• Inconsistent pressure on each cell</li> </ul>	<ul style="list-style-type: none"> <li>• Pressure measurement vulnerable to fluctuations in environment</li> <li>• Open air condition results in quick evaporation of fluid reservoir and leads to frequent recalibration</li> </ul>	N/A	<ul style="list-style-type: none"> <li>• Surface treatment</li> <li>• Requires the shape of cells to be isotropic</li> </ul>
<b>References</b>		[27–30]	[31,32]	[33–35]	[36,37]	[38–40]

Traditional single cell techniques include MPA [33–35], atomic force microscope [36,37] and optical tweezers [38–40]. In general, all of these single-cell techniques require the use of specialized equipment and skilled technicians. Another drawback is the low cell throughput due to the time-consuming process (Table 1-1). MPA measures single cell deformability from the mean displacement of a RBC along a glass micropipette when it is partially suctioned into the micropipette. The relationship between the suction pressure and the mean displacement is then expressed as the cell's shear modulus,  $\mu$ . Atomic force microscopy determines RBC deformability by measuring the force required to deform the surface of the RBC and consequently, deflects the tip of the cantilever. An indentation versus force curve provides the Young's Modulus (E) of each RBC. With optical tweezers, microparticles are attached onto both sides of the RBC membrane, one of which is fixed while the other one is controlled by a highly focused laser to elongate each RBC. A force-displacement curve between two locations on the RBC membrane can be obtained, resulting in a measure of RBC deformability, which is expressed as the elastic shear modulus,  $\mu$ , of the membrane.

## **1.2.2 Microfluidic techniques**

The previously described technologies are limited by either their inability to evaluate single cells, their costly equipment, their delicate experiment process or their throughput. Microfluidic technologies can be used to address these challenges due to their low-cost, portable and high-throughput processing. Furthermore, microfabrication and microfluidic technologies combine the ability to pattern pores comparable in size to the smallest human capillaries with the ability to precisely control the flow of minute volumes of liquid. Recently, a number of micro-scale structures have been developed on a microfluidic platform to study the deformability of single cells, which include wedging in tapered constriction [9] and measurement of transit time [41–43] or transit pressure [44–46] through micro-scaled constrictions. All of these technologies are created to mimic the *in vivo* situations of splenic filtration of red cells and red cells circulating in capillaries.

### ***1.2.2.1 Wedging in tapered constrictions***

This microfluidic device contains a row of tapered constrictions, each made at an angle of  $\sim 5^\circ$  and an opening of  $\sim 1 \mu\text{m}$  (Figure 1-5) [9]. Individual RBCs are suctioned into the

constrictions due to a flow that runs parallel to them. The area-to-volume ratio can be calculated from the position of the cells and geometry of the constrictions, which defines the RBCs deformability. Even though this device is easy to operate, the optical measurement of the cells position is of sub-micrometer accuracy, limiting the sensitivity of this device.

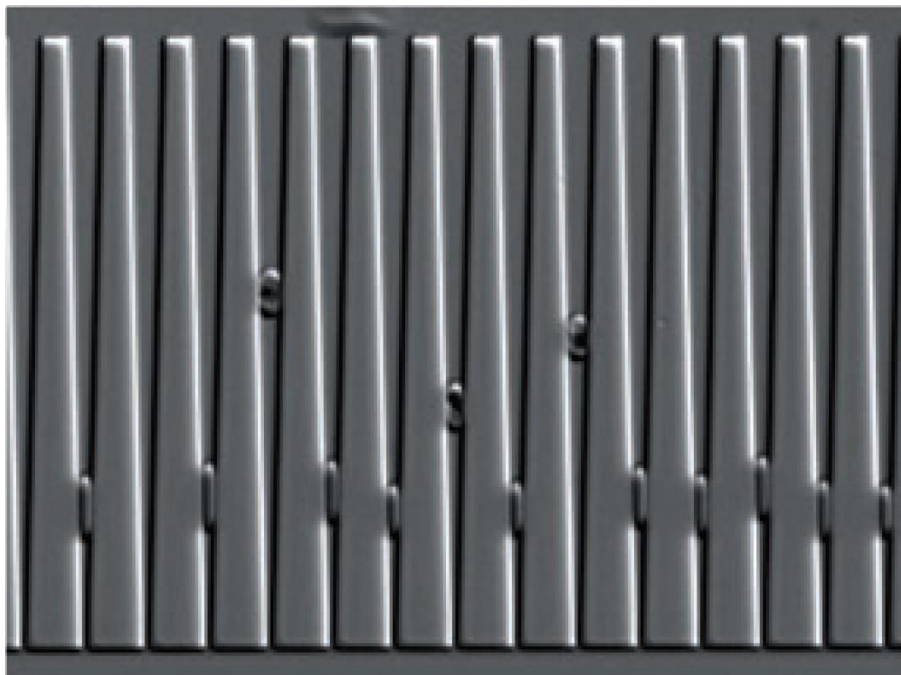


Figure 1-5: Wedged RBCs in tapered constrictions. RBCs move to different locations based on their deformability [9].

### ***1.2.2.2 Transit time through micro-scale constrictions***

RBC deformability can be measured by measuring the transit time of individual RBCs through micro-scale constrictions. An example of this method, also called the deformability-based flow cytometer [42], uses arrays of triangle-shaped pillars, with constrictions smaller than the diameter of RBCs (Figure 1-6A). As a result, RBCs with different deformability travel with different velocity through these pillars. Fluorescence measurements of each RBC are simultaneously acquired, resulting in an automated and high-throughput device that is capable of measuring the deformability of 1000 – 10,000 individual RBCs. However, this device does not incorporate any mechanism to ensure that consistent pressure difference is applied to each cell.

Zheng et al. [43] demonstrated a microfluidic system that simultaneously use both mechanical and electrical characterization of single RBCs, enabling a high throughput of 100 –

150 cells/s (Figure 1-6B). In this system, the cell transit time through the constriction was measured automatically by detecting the changes in the electrical resistance between the two electrodes placed on either side of the constriction as cells pass through it. However, this system is prone to clogging since they rely on pushing many RBCs through a single micro-scale constriction.

Both of these technologies are also difficult to parallelize because of the need to monitor the deformation process using a fluorescence measurement or to integrate electrical sensors on a disposable microfluidic chip.

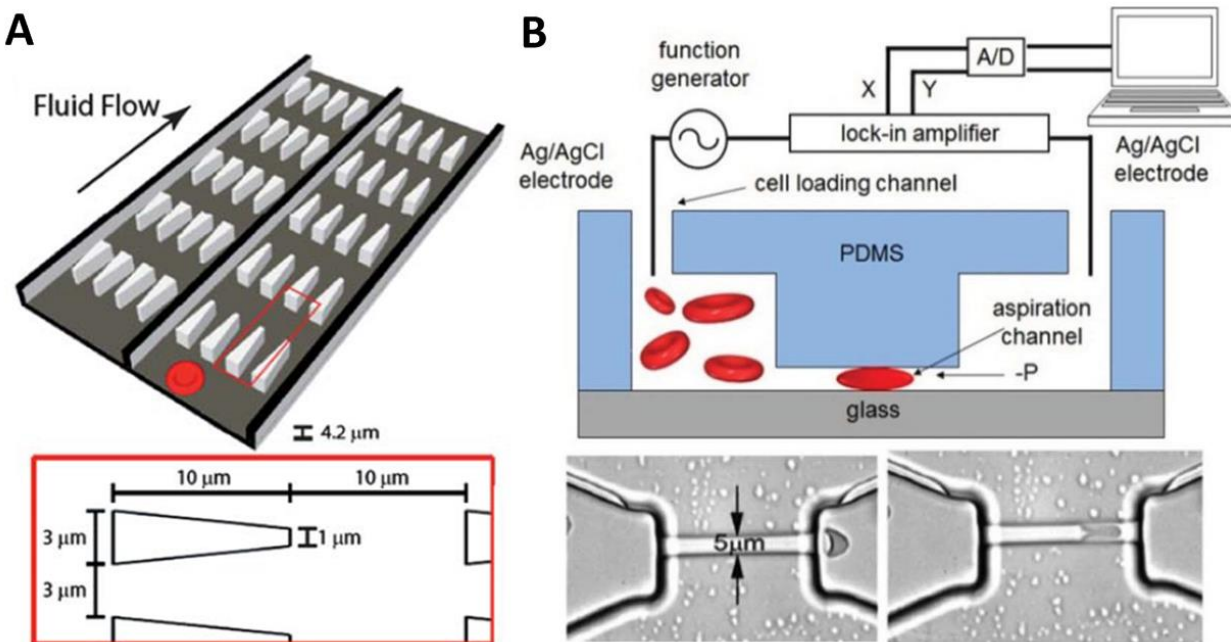


Figure 1-6: (A) Deformability-based flow cytometer with triangular pillar arrays [42]. (B) Schematic of microfluidic system for electrical and mechanical characterization of RBCs [43].

### 1.2.2.3 Transit pressure through micro-scale constrictions

Another way to measure RBC deformability using micro-scale constrictions is to measure the transit pressure required to squeeze single cells through a micro-scale constriction. An example of such a device is illustrated in Figure 1-7A, where it contains one row of constrictions with different constriction sizes (Figure 1-7B).

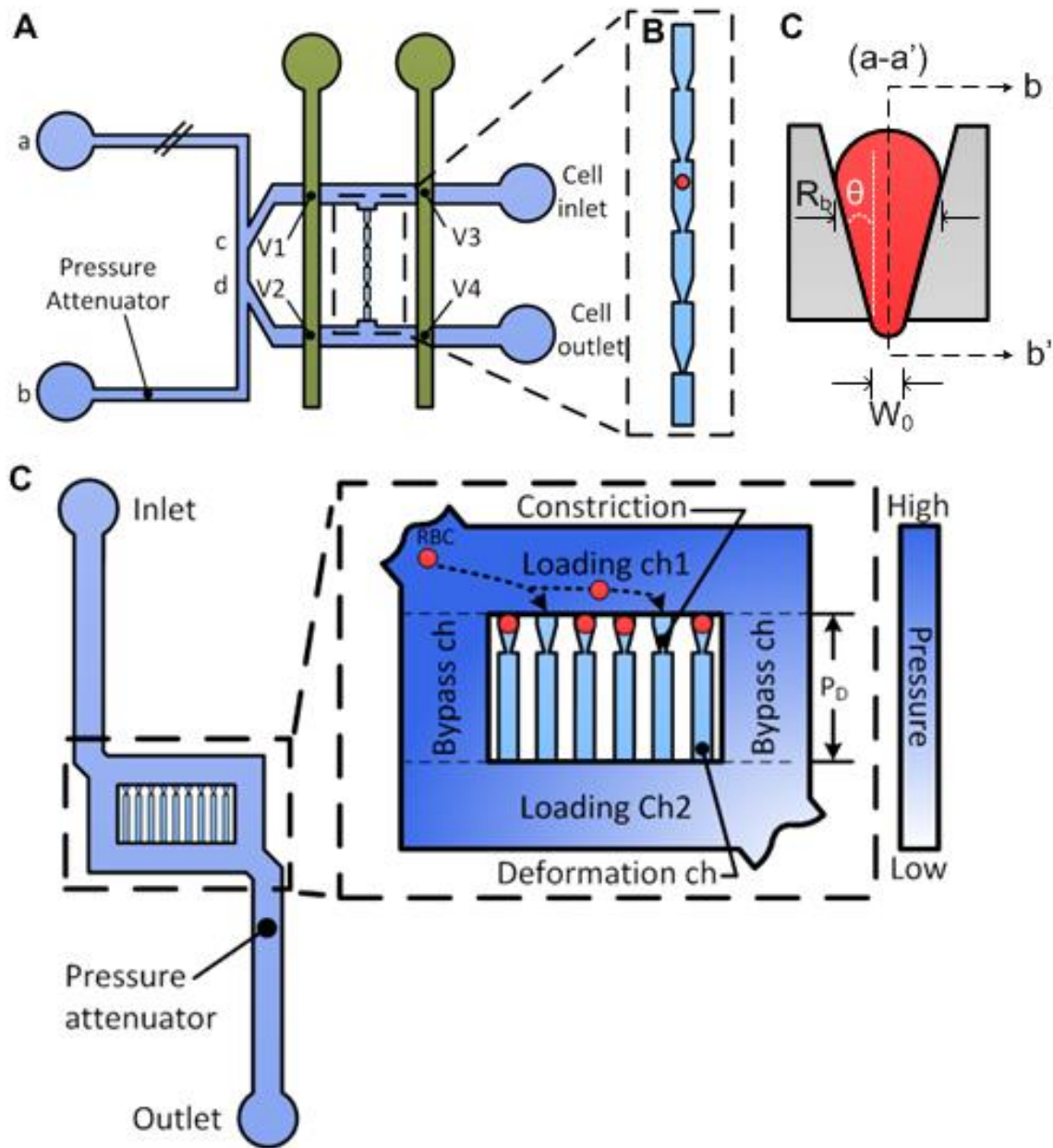


Figure 1-7: (A) Overview of the transit pressure device developed by Guo *et al.* [45] (B) Magnified view of the row of constrictions. (C) Geometric representation of a RBC deforming through a funnel constriction. (D) Multiplexed version of the transit pressure device [46].

The deformability of each cell is defined by the cortical tension ( $T_c$ ) (Equation 1-1), which is calculated from the pressure applied ( $P_D$ ) and the geometry of the constrictions used (Equation 1-2).

$$T_c = \frac{P_D}{\frac{2}{W_0} - \frac{1}{R_b}} \quad \text{Equation 1-1}$$

$$R_b = \sqrt{\frac{\frac{\pi R_0^2 h_0}{H_0} + \frac{W_0^2 \cos\theta}{4 \sin\theta} - \frac{\pi W_0^2}{8}}{\frac{\pi}{2} + \frac{\cos\theta}{\sin\theta}}} \quad \text{Equation 1-2}$$

where  $P_D$  is the applied pressure difference on the cell,  $W_0$ ,  $H_0$  and  $\theta$  is the funnel pore size, thickness and taper angle (Figure 1-7C),  $R_0$  is the radius of the RBC and  $R_b$  is the radius of the trailing edge of a RBC as it deforms.

This device showed high sensitivity for measuring single RBC deformability, but since RBCs need to be individually captured using valves on a second PDMS layer, the process is time-consuming and requires skilled technicians. As a result, the throughput of this device is relatively low, ~40 RBCs in a typical experiment that takes ~3 hours. In addition, the device fabrication is arduous since it requires a two-layer alignment. A multiplexed version of this device, termed multiplexed fluidic plunger (Figure 1-7D), improves the throughput considerably with a measurement speed of ~100 RBCs per hour [46].

However, both of these techniques rely on the measurement of  $T_c$  and in turn, optical measurement of the constriction geometry to determine the deformability of each cell, which is a tedious and time-consuming process. They also require video microscopy to monitor the deformation process that eventually limits the throughput and parallelizability of the device. Due to the high sensitivity of these techniques and the potential for improvement, the work presented in this thesis is based on these two previous ideas [45,46].

### 1.3 Design concept and research goals

The use of RBC deformability in biological assays is currently limited by two key challenges. First, pathological cells typically comprise only a small fraction of the overall cell sample, and therefore a large number of single cells must be sampled in order to obtain useful data. Second, to assay specific biological properties, multiple positive and negative controls need to be processed in parallel. While recent microfluidic techniques improve the throughput in

measuring single RBC deformability, none of them show the ability to assay multiple samples in parallel.

To address these issues, this thesis focuses on the development of a novel microfluidic mechanism here termed trans-dispersion, which captures the advantages of gel electrophoresis. This mechanism enables sensitive, high-throughput and massively parallel measurements of individual RBCs that is readily adaptable for use in clinical settings. The research goals of this thesis are as follows:

1. To design and develop the trans-dispersion mechanism for measuring the deformability of individual RBCs.
2. To verify the ability of this mechanism to consistently measure RBC deformability while overcoming constriction occupancy error.
3. To validate the sensitivity of the device using oxidatively-damaged RBCs as compared to other techniques.
4. To increase the throughput of the device in measuring the deformability of individual RBCs
5. To measure changes in RBC deformability associated with malaria parasitism.
6. To validate the parallelizability of this device by assessing the efficacy of multiple anti-malarial drugs.

## Chapter 2: Device Principle, Design and Operation

Gel electrophoresis is a fundamental technology enabling modern molecular biology and genetics. This process involves migrating DNA or protein molecules in agarose gel using an electric field, where the final positions of the molecules in the gel indicate their size relative to known controls. Trans-dispersion mechanism is an analogous process for red blood cells (RBCs), where individual cells are transported through a series of micro-scale constrictions in a microchannel using pressure-driven flow (Figure 2-1). The final positions of RBCs indicate their deformability, similar to intensity bands in a DNA gel, thereby enabling repeatable, high-throughput, and parallelized measurements of RBC deformability.

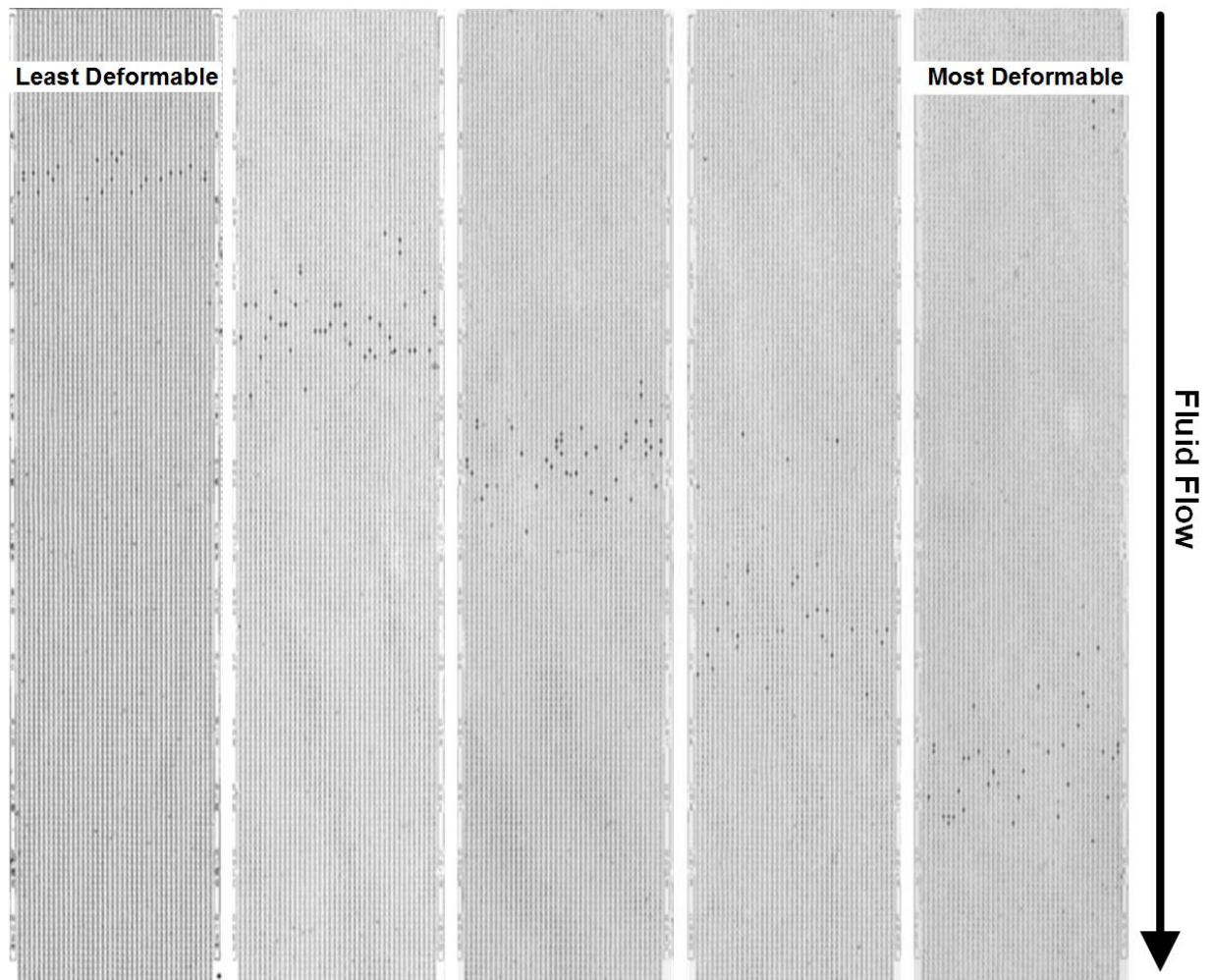


Figure 2-1: The trans-dispersion mechanism. Position of the cells along the device is indicative of their transit speed and hence, their deformability. More deformable cells will travel further along the device than less deformable cells.

Chapter 2 details the principle, design and operation of trans-dispersion mechanism. Section 2.1 describes the fluidic plunger mechanism. Section 2.2 and 2.3 detail the design of the trans-dispersion mechanism, including its functional requirements, challenges and how the trans-dispersion design addresses them. Section 2.4 describes device operation by detailing the measurement process (section 2.4.1), the optimization of pressure waveform applied to deform the cells (section 2.4.2) and the design of the manifold to parallelize the trans-dispersion array (section 2.4.3). Section 2.5 details the various parameters of each trans-dispersion prototype based on the target cell. Finally, section 2.6 describes the relationship of the work outlined in this thesis to previous works from our group.

## 2.1 Fluidic plunger mechanism

At a single cell level, trans-dispersion mechanism incorporates the design of the fluidic plunger mechanism described previously by Quan Guo from our group [49]. This mechanism infuses a single RBC into a microchannel containing a funnel-shaped constriction whose geometry was carefully designed to ensure that consistent forces are applied to each cell. Funnel pore size ( $W$ ) and funnel thickness ( $H_0$ ) are the two major factors that determine the design of the funnel constriction. The pore size of the funnel is smaller than the diameter of RBC to achieve optimal cell compression (Figure 2-2). The thickness of the deformation microchannel is also designed to match the average thickness of RBCs and orient them into planar configuration (Figure 2-2), enabling the cells to form a temporary seal as they deform through the constriction

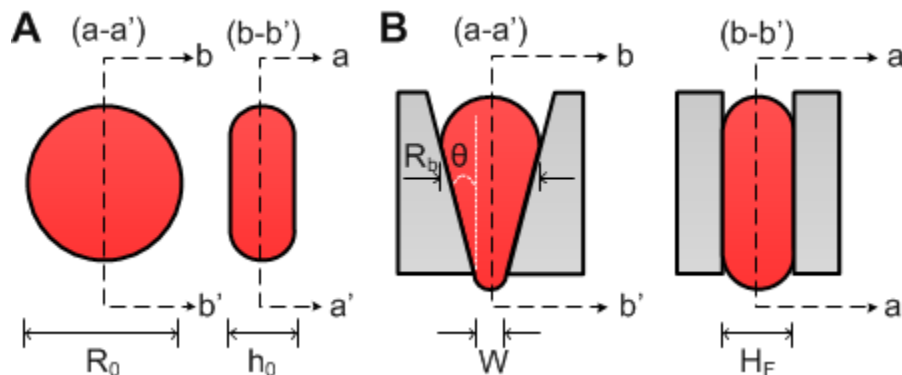


Figure 2-2: Top and side sections of (A) a RBC at rest and (B) a RBC deforming through a microscale constriction [50].

As we showed previously [46,51], the fluidic plunger mechanism forms a temporary seal between the deformed cell and the constriction, allowing an pressure difference applied across the length of the microchannel to be focused across each cell. Hence, this mechanism effectively acts as a plunger to remotely deliver a precisely controlled pressure on the cell (Figure 2-3). A similar process takes place as a cell transits through a constriction in the deformation microchannel. As shown in Figure 2-3C, when the cell moves freely in the funnel microstructure without deformation, its position changes rapidly. However, as the cell is deformed through the narrowest parts of the constriction, the position of the cell is nearly stationary, which confirms the existence of a temporary seal, and allowing the applied pressure to focus across the cell. Finally, as a part of the cell membrane crowns through the constriction, the cell is pulled rapidly through the constriction because of a phenomenon known as Haine’s jump [52].

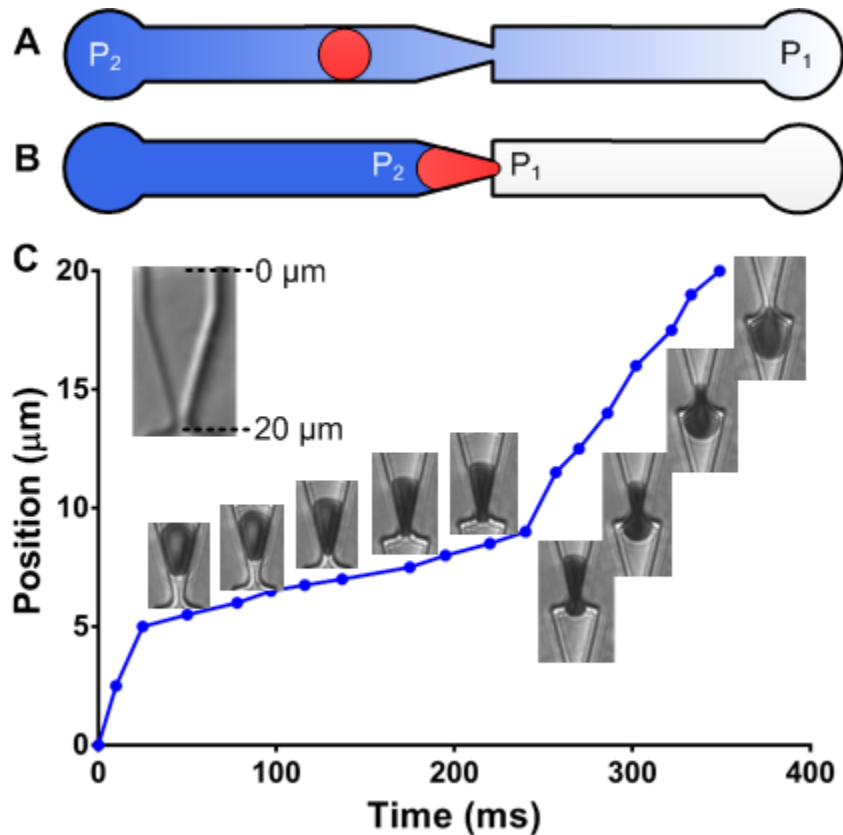


Figure 2-3: Fluidic plunger mechanism (A) The applied pressure is distributed across the microchannel when the cell is not deformed through the constriction [46]. (B) The applied pressure focuses across the cell when the cell is deformed through the constriction. (C) When a constant pressure is applied, the position of the cell along the funnel (insert) shows that the cell acts as a temporary seal against the constriction as it being deformed.

## 2.2 Functional requirements for the trans-dispersion mechanism

### 2.2.1 Motivation

The design of the trans-dispersion mechanism is inspired by gel-electrophoresis to achieve two main goals: 1) Maximize sensitivity to RBC deformability and 2) Maximize the number of individual RBCs measured simultaneously. To maximize sensitivity to RBC deformability, the cellular trans-dispersion mechanism repeatedly deforms each RBC multiple times using a series of micro-scale constrictions. To measure many RBCs simultaneously, this process is performed in parallel.

The cellular trans-dispersion process arranges the funnel-shaped constrictions in series, forming a single deformation microchannel, and achieves deformability-based transport of RBCs by repeated application of the fluidic plunger mechanism (Figure 2-4). Each deformation microchannel consists of several funnels arranged in series ( $N_F$ ). Similar to transport of molecules in gel electrophoresis, each RBC undergoes repeated deformations through hundreds of micro-scale constrictions using a pressure-driven flow in order to average over variations in constriction geometry. Furthermore, the final position of the cell along the deformation microchannel indicates its deformability, enabling a simple position-based measurement of RBC deformability.

To maximize the throughput of cells, trans-dispersion array multiplexes the single-cell transport by arranging the deformation microchannels in parallel (Figure 2-4). Each trans-dispersion array consists of a number of parallel deformation microchannels ( $N$ ).

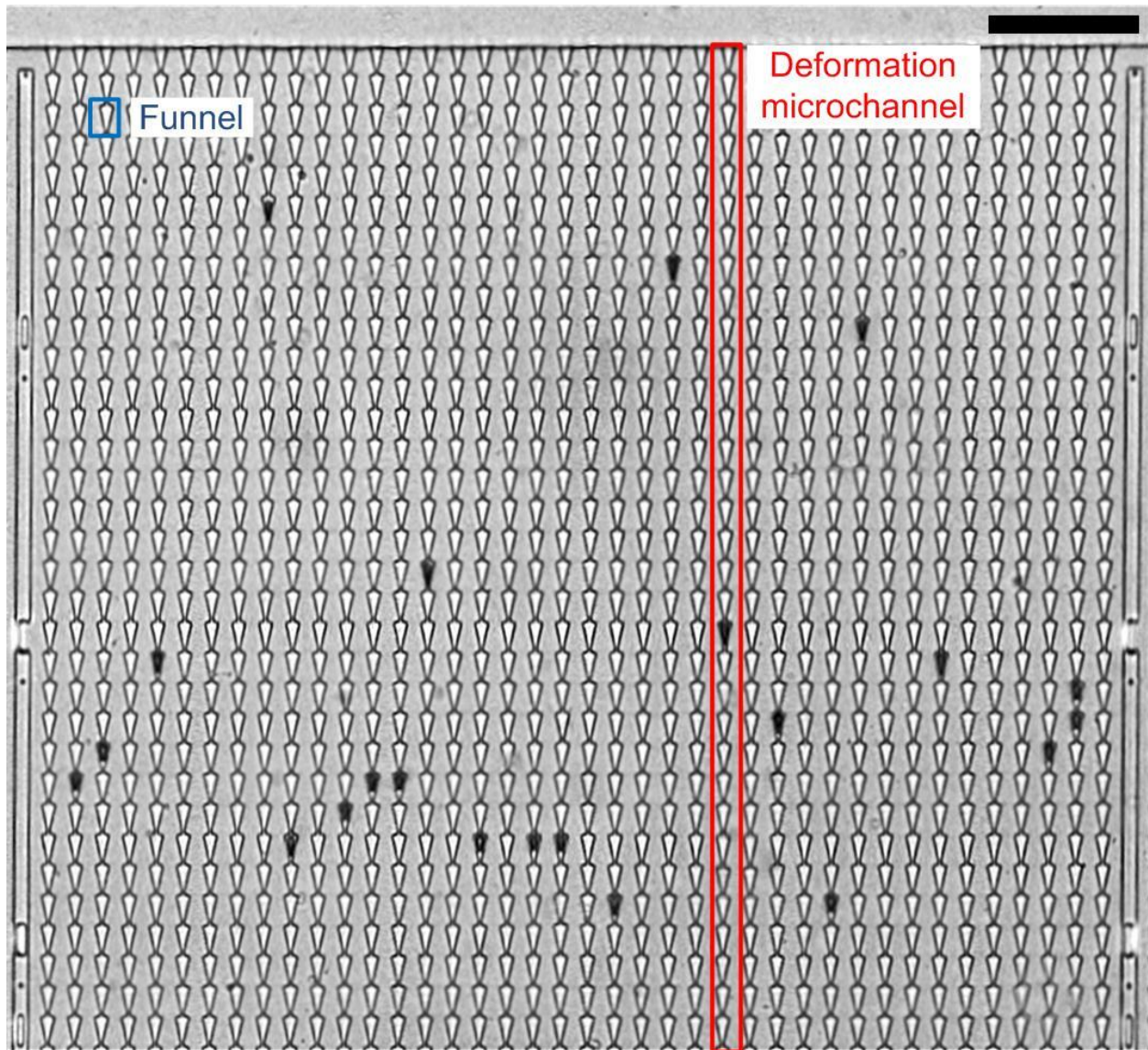


Figure 2-4: Micrograph of a zoomed-in section of the trans-dispersion device, showing  $N_F$  individual funnels (blue box) connected in series to form  $N$  parallel deformation microchannels (red box) (scale bar =  $75 \mu\text{m}$ ).

## 2.2.2 Constraints and challenges

### 2.2.2.1 Device size and camera field of view

The sensitivity and throughput of the trans-dispersion mechanism can be increased by increasing the number of funnels in series ( $N_F$ ) and the number of parallel deformation microchannels ( $N$ ), respectively. However, since the final positions of RBCs along the deformation microchannel are analyzed using image analysis software, significant effort is

required in the image capture process and image analysis software if the position of the RBCs exceeded the field of view of the camera. Therefore, a practical limit to both  $N_F$  and  $N$  is the field of view of the microscope camera.

### **2.2.2.2 Multi-cell loading**

One challenge in cellular trans-dispersion design is the possibility of multiple cells loading into the same deformation microchannel. Since trans-dispersion mechanism continuously deforms each RBC as it passes through each constriction, the presence of multiple cells will affect the fluid flow in the deformation microchannel. Therefore, the pressure drop in the deformation microchannel is not focused on a single cell but is distributed inconsistently amongst the multiple cells. The worst-case pressure difference occurs when more deformable cells enter the deformation microchannel first, followed by the less deformable cells. The stiffer cells take more time to deform through the constrictions, blocking the fluid flow for the more deformable cells ahead of them. These softer cells travel slower than they should be and therefore, their final positions become an invalid representation of their deformability.

### **2.2.2.3 Multiplexing error**

Another key challenge in multiplexing cellular trans-dispersion is to ensure a consistent pressure is applied across each deformation microchannel independent from the number of deformation microchannels occupied with cells. The pressure applied across the deformation microchannels ( $P_D$ ) varies with the number of deformation microchannels occupied with cells (Figure 2-5). This phenomenon could be explained by considering the fluid flow in the loading and deformation microchannels in the following two situations: 1.) When the deformation microchannels contain no cells, fluid streamlines in the loading microchannels are evenly distributed across the deformation microchannels (Figure 2-5A). 2.) When one or more of the deformation microchannels are occupied with cells, the fluid flow is blocked in that channel. Consequently, fluid streamlines in the loading microchannel are skewed into the remaining unblocked deformation microchannels (Figure 2-5B). The difference between these two situations results in an inconsistency in the flow inside the deformation microchannels, and the

resulting deformation pressure,  $P_D$ . An equivalent hydrodynamic circuit of these two cases is shown in Figure 2-5, where:

- $P_{ab}$ : Pressure across loading and bypass microchannels.
- $P_D$ : Deformation pressure.
- $R_D$ : Hydrodynamic resistance of individual deformation microchannel.
- $R_L$ : Hydrodynamic resistance of loading microchannels.
- $R_{eq}$ : Equivalent hydrodynamic resistance of bypass and loading microchannels.

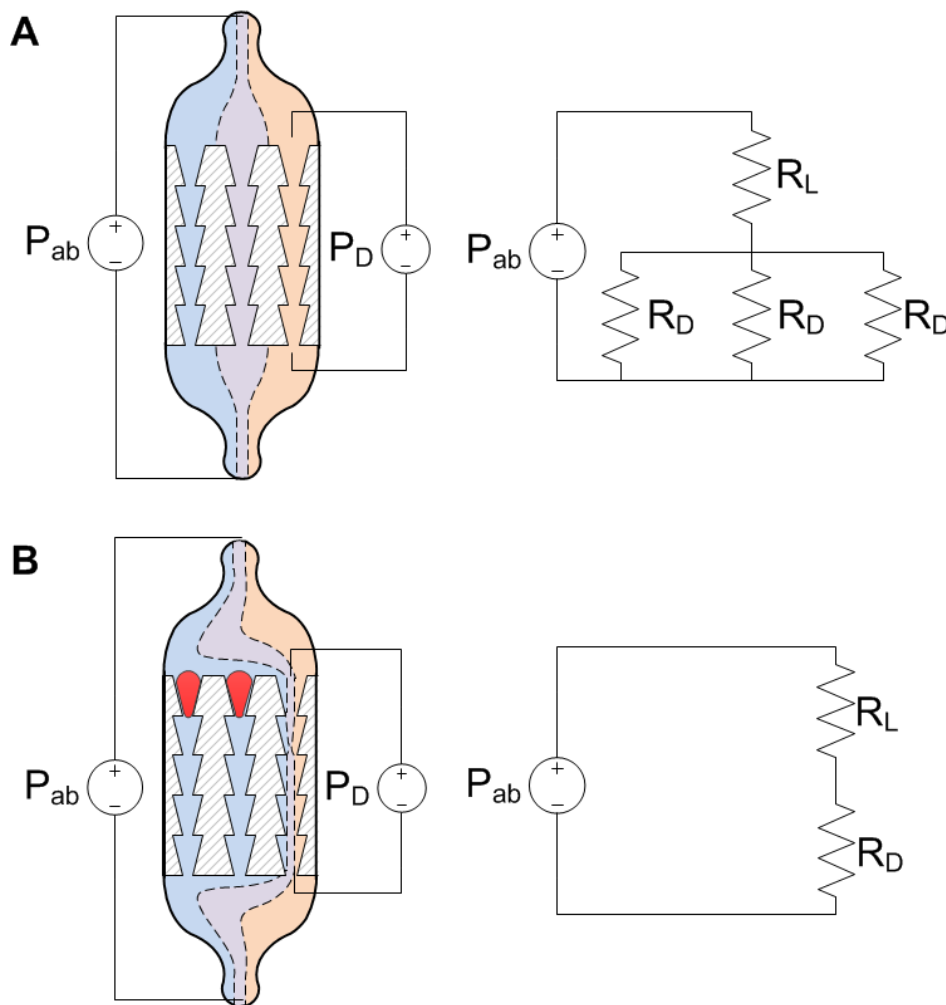


Figure 2-5: Graphic representation of fluid streamlines in the loading and deformation microchannels and its associated hydrodynamic circuit when: (A) All deformation microchannels are unoccupied with cells and (B) only one deformation microchannel is unoccupied.

The potential error on the pressure across the deformation microchannels ( $P_D$ ) due to the microchannel occupancy can be estimated by considering the worst-case pressure difference, which occurs when the deformation microchannels are occupied with a single cell ( $P_{D,1}$ ) and when the deformation microchannels are completely occupied with cells ( $P_{D,N}$ ) and is estimated by Equation 2-1.

$$\text{Multiplexing Error (E}_M\text{)} = \frac{P_{D,N}}{P_{D,1}} - 1 \quad \text{Equation 2-1}$$

Hence, to ensure a consistent pressure is applied across each deformation microchannel, this multiplexing error needs to be minimized.

#### ***2.2.2.4 Spatial position of deformation microchannels***

Another challenge in generating consistent pressure drop in each deformation microchannel is due to the potential variance caused by the spatial position of deformation microchannels across the loading microchannel. Since fluid in the loading microchannels flows into multiple deformation microchannels, different deformation microchannels might experience different pressures depending on their spatial position. Hence, the trans-dispersion device has to be designed to minimize the error due to the spatial position.

#### ***2.2.2.5 Loading rate of cells***

To maximize the number of cells that can be measured simultaneously, sufficient RBCs have to be loaded into the deformation microchannels. From experimental observations, several factors affect the loading rate of RBCs into the deformation microchannels: 1.) Hydrodynamic resistance of the loading and individual deformation microchannel. 2.) Flow rate of RBCs along the loading microchannel. 3.) Concentration of RBCs in the device.

If the hydrodynamic resistance of deformation microchannel ( $R_D$ ) is too high relative the hydrodynamic resistance of the loading microchannel ( $R_L$ ), RBCs will not load into the deformation microchannel (Figure 2-6). The probability of RBCs entering the deformation microchannels is increased if the flow rate of RBCs in loading microchannel is low since cells

settle down and form part of the bottom streamlines that reach the deformation microchannels, which is possible since RBCs have a fast sedimentation rate [53]. Another factor that affects the loading rate of cells into deformation microchannels is the concentration of cells in the sample. If the concentration is too low, the probability of cells in the correct streamline for entering deformation microchannel is reduced.

#### **2.2.2.6 Synchronized measurement**

When RBCs are loaded into the first funnel of the deformation microchannel, there is a possibility that the RBC will transit through the constriction with a small pressure, which would affect the final positions of the cells along the deformation microchannel and hence, the deformability measurement. As such, it is necessary to ensure that all of the RBCs loaded into the deformation microchannels experience a synchronized deformation process. To avoid the loaded RBCs from transiting through the constriction, the cells are loaded into the deformation microchannels at a pressure that is insufficient for them to transit through the constriction.

### **2.3 Design of trans-dispersion device**

This section details how the design of trans-dispersion mechanism satisfies the functional requirements and addresses the challenges outlined in the previous section.

Trans-dispersion array multiplexes the single-cell transport by arranging the deformation microchannels in parallel, which are then supported by loading and bypass microchannels to form a rectangular detour around the deformation microchannels (Figure 2-6A). This rectangular detour is connected at two opposing corners to a long pressure attenuator microchannel. The pressure is applied to the ends of the pressure attenuator microchannel, which acts as the fluid reservoirs. Single cells are transported from the fluid reservoirs through the pressure attenuator, bypass and loading microchannels into the entrance of each deformation microchannel. An equivalent hydrodynamic circuit is shown in Figure 2-6B, where:

- $P$ : Applied pressure.
- $P_{ab}$ : Pressure across loading and bypass microchannels.
- $P_D$ : Deformation pressure.

- $R_D$ : Hydrodynamic resistance of individual deformation microchannel.
- $R_B$ : Hydrodynamic resistance of bypass microchannels.
- $R_L$ : Hydrodynamic resistance of loading microchannels.
- $R_{eq}$ : Equivalent hydrodynamic resistance of bypass and loading microchannels.
- $N$ : Number of parallel deformation microchannels
- $N_F$ : Number of funnels in series within each deformation microchannel

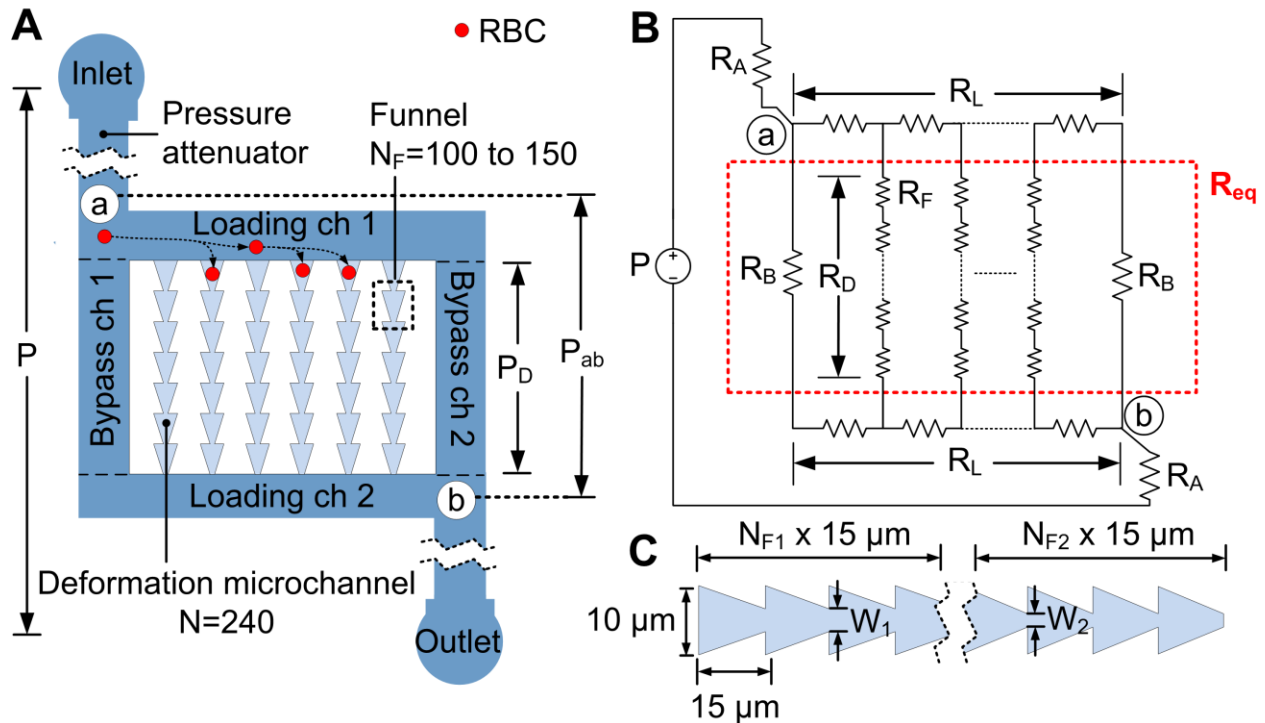


Figure 2-6: (A) Structure and components of the multiplexed trans-dispersion mechanism with individual RBCs loading into the deformation microchannels. (B) An equivalent hydrodynamic circuit of the multiplexed trans-dispersion mechanism. (C) Detailed design of deformation microchannel.

### 2.3.1 Deformation microchannel

The sensitivity of cellular trans-dispersion depends on several factors: the funnel pore size ( $W$ ), the thickness of the deformation microchannel ( $H_F$ ) and the number of funnels ( $N_F$ ) in each deformation microchannel. The funnel pore size should be smaller than the diameter of RBCs to achieve optimum cell compression while the thickness of the deformation should match the thickness of RBCs to ensure that the RBCs will form a temporary seal against each constriction as they deform. Depending on the target cell, this work uses a microchannel

thickness ( $H_0$ ) between 3.7 – 4.5  $\mu\text{m}$  and constriction pore sizes ( $W$ ) between 1.5 – 2.5  $\mu\text{m}$ , as detailed in Table 2-3 in section 2.5.

The length of the funnel ( $L_F$ ) and the width of the funnel ( $W_F$ ) are designed such that the horizontal cross-section area (a-a' of Figure 2-2) of the funnel allows the RBCs to deform back to their discoid shape in a planar configuration. However, if these dimensions are too large, RBCs will move freely for a longer duration between constrictions, increasing the probability of multiple cells loading in the same deformation microchannel (section 2.2.2.2). The horizontal cross-section area of a funnel with  $L_F$  of 15  $\mu\text{m}$ ,  $W_F$  of 10  $\mu\text{m}$  and  $W$  of 2  $\mu\text{m}$  is 90  $\mu\text{m}^2$ , while RBC has a cross-section area of  $\sim 50 \mu\text{m}^2$ . Hence, these geometries were deemed sufficient to allow RBCs to deform back to its original shape while limiting the probability of multi-cell loading.

During microfabrication process (section 3.1), deformation microchannels have to be aligned with the remaining microstructures. This alignment process would be easier if  $L_F$  of the first funnel in the deformation microchannel is longer. However, longer  $L_F$  increases the probability of multiple cells loading. Hence,  $L_F$  of the first funnel was chosen to remain as 15  $\mu\text{m}$ . When there was no pressure applied, this dimension would only fit a single RBC in the first funnel.

Besides the funnel pore size and thickness of deformation microchannel, the number of constrictions (funnels) in a single deformation microchannel also plays an important role in device sensitivity (Figure 2-6C). Higher number of constrictions theoretically leads to higher sensitivity since the cells have to undergo more deformations. However, as mentioned in section 2.2.2.1, device size and analysis time becomes the practical limitation for this factor. Funnel number between 100 and 150 results in sufficient device sensitivity while containing the deformation microchannel region in one field-of-view.

In addition to using deformation microchannels with a single pore size, multiple pore sizes can be used to resolve cell samples containing different ranges of deformabilities (Figure 2-6C). Specifically, both one-stage and two-stage prototypes were tested in this work. A one-stage device has the same constriction size for all funnels while two-stage devices have a larger

constriction size in the first half of the deformation microchannel. Larger constriction size has to be placed in the beginning of the deformation microchannel otherwise cells with different deformability will be captured in the beginning and cannot be sufficiently separated.

### 2.3.2 Loading microchannels

As explained in section 2.2.2.3, the key design challenge for loading microchannels is to ensure that the multiplexing error is minimized. To estimate the potential error due to microchannel occupancy on the pressure across the deformation microchannels ( $P_D$ ) for a device with  $N$  deformation microchannels, the worst-case pressure difference is considered, which occurs when the deformation microchannels are occupied with a single cell and when the deformation microchannels are completely occupied with cells, which can be estimated as follows:

Deformation microchannels occupied with a single cell:

$$P_{D,1} \approx P_{ab} \left( \frac{R_D}{R_D + (N - 1)2R_L} \right) \quad \text{Equation 2-2}$$

Deformation microchannels completely occupied:

$$P_{D,N} = P_{ab} \quad \text{Equation 2-3}$$

where  $N$  is the number of parallel deformation microchannels,  $R_D$  and  $R_L$  is the hydrodynamic resistance of the deformation microchannels and loading microchannel, respectively. The multiplexing error ( $E_M$ ) is evaluated as the pressure difference between these two extreme cases (Equation 2-4):

$$E_M = \frac{P_{D,N}}{P_{D,1}} - 1 = (N - 1) \frac{2R_L}{R_D} \quad \text{Equation 2-4}$$

Hence, to minimize the multiplexing error, the hydrodynamic resistance of loading ( $R_L$ ) and deformation microchannels ( $R_D$ ) must follow the condition of Equation 2-5. Maximizing the ratio of  $R_D/R_L$  based on a target  $N$  can minimize this error.

$$\frac{R_D}{(N - 1)} \gg R_L$$

Equation 2-5

To define an acceptable error threshold, Table 2-1 examines the natural variability (NV) in cell deformability, where NV is defined as the percentage uncertainty (ratio of standard deviation and mean) of a single cell population while Table 2-2 examines the differences in deformability caused by disease pathology. Since both NV in cell deformability and the difference in deformability caused by disease pathology is typically >5%, a multiplexing error <5% is sufficient to ensure that consistent deformation pressure ( $P_D$ ) is applied in each deformation microchannel.

Table 2-1: Natural variability (NV) between RBCs of the same sample, where NV is defined as the percentage uncertainty of the sample (standard deviation/mean).

<b>Biological system</b>	<b>Technique</b>	<b>NV</b>	<b>Reference</b>
Healthy patients	Micropore Filtration	13%	[32]
Stored RBCs	Micropore Filtration	8%	[31]
Healthy patients	Optical Tweezer	16%	[39]
Healthy patients	AFM	10%	[37]
Healthy patients	Transit Pressure	8%	[6]

Table 2-2: Differences in deformability due to disease pathology between healthy and diseased samples in different biological systems where PV is defined as the percentage difference between these two states.

<b>Biological system</b>	<b>State studied</b>	<b>Technique</b>	<b>PV</b>	<b>Reference</b>
Iron deficiency	Healthy vs patients	Ektacytometry	11%	[13]
Sickle-cell disease	Steady vs Crisis	Micropore Filtration	19-33%	[54]
Thalassemia	Healthy vs patients	AFM	54%	[36]
Malaria	Healthy vs infected	Rheoscopy	18%	[55]
Malaria	Healthy vs uRBCs	MPA	14%	[56]
Malaria	uRBCs vs ring stage	Transit Pressure	31%	[21]

### 2.3.3 Bypass microchannels

As explained in section 2.2.2.4, spatial position of deformation microchannels across the loading microchannel might cause a variance in the pressure drop in each deformation microchannel. Since fluid in the loading microchannels flows into multiple deformation microchannels, different deformation microchannels might experience different pressures depending on their spatial position. To address this challenge, bypass microchannels which are parallel to the deformation microchannels are included in the design. Together with the loading microchannels, bypass microchannels form a symmetrical, rectangular detour that contains the deformation microchannels to bifurcate the fluid flow around the block (Figure 2-6). As such, the pressure gradient that forms at the starting points of the deformation microchannels is compensated by an identical pressure gradient at the end the deformation microchannels, providing identical pressure drops in each deformation microchannel across the loading microchannel (Figure 2-7A).

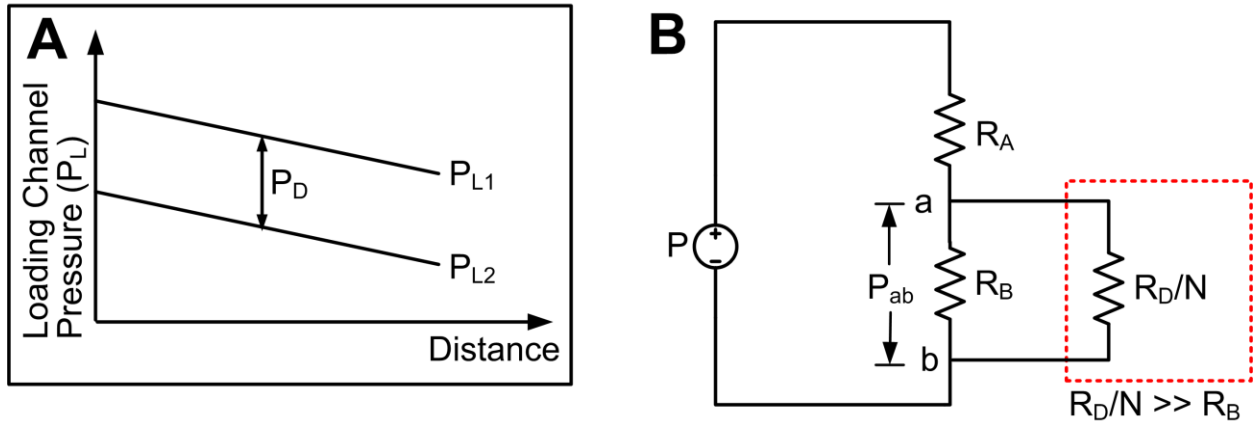


Figure 2-7: (A) Pressure in the two loading microchannels ( $P_L$ ) as a function of distance. (B) Hydrodynamic circuit illustrating the principle of pressure attenuation.

Bypass microchannels also ensure consistent applied pressure ( $P_{ab}$ ) across all deformation microchannels when deformation microchannels provide the dominant hydrodynamic resistance and hence, enabling  $P_{ab}$  to not be affected by cells in the deformation microchannels (Figure 2-7B). The  $P_{ab}$  error due to deformation microchannel occupancy is estimated by considering the worst-case pressure differences, similar to the two cases in estimating multiplexing error. Since the hydrodynamic resistance of the loading microchannel ( $R_L$ ) is negligible ( $<5\%$  of  $R_{D/N}$ ),  $R_L$  can be ignored.

Deformation microchannels occupied with a single cell:

$$R_{eq,1} \approx \frac{R_D R_B}{2R_D + (N - 1)R_B} \quad \text{Equation 2-6}$$

Deformation microchannels completely occupied:

$$R_{eq,N} = \frac{R_B}{2} \quad \text{Equation 2-7}$$

where  $N$  is the number of parallel deformation microchannels, and  $R_D$  and  $R_B$  is the hydrodynamic resistance of the deformation microchannels and bypass microchannel, respectively. The resulting error on  $P_{ab}$  due to deformation microchannel occupancy can be estimated as:

$$E = \frac{R_{eq,N}}{R_{eq,1}} - 1 = (N - 1) \frac{R_B}{2R_D} \quad \text{Equation 2-8}$$

By minimizing  $E$  to  $<5\%$ , which is much smaller than the natural variability of most biological systems (Table 2-1), this symmetrical bifurcation structure compensates for the different positions of the deformation microchannels by maximizing the ratio of  $R_D/R_B$  based on a target  $N$  (Equation 2-9).

$$\frac{R_D}{(N - 1)} \gg R_B \quad \text{Equation 2-9}$$

To validate the theoretical error due the occupancy of the deformation microchannel (section 2.3.2 and 2.3.2), COMSOL simulations were performed that take into account both the loading and the bypass microchannels. Both worst-case pressure differences were determined by simulating the flow in the device in the two following situation: 1.) The design contains all the microchannels, which is the closest estimate of the deformation microchannels occupied with a single cell i.e.  $P_{D,1}$  and 2.) The design doesn't contain any deformation microchannels, which is the case when deformation microchannels are completely occupied i.e.  $P_{D,N}$ . A pressure of 1 Pa was applied between the inlet and outlet, and the deformation pressure of each deformation

microchannel was determined in both situations ( $P_{D, 1}$  and  $P_{D, N}$ ). The error of these two cases is then represented by the difference of pressure drop of each deformation microchannel in these two extreme cases (Equation 2-4).

### 2.3.4 Pressure attenuator

Small pressures ranging between 1 to 25 Pa are typically required to deform single RBCs through a 1.5 to 2  $\mu\text{m}$  funnel-shaped constrictions. These small pressures are difficult to generate reliably using external instrumentation, which provides a minimum pressure of 30 Pa (0.3 mbar). Additional fluidic infrastructure, described previously as pressure divider fluidic circuit [51], is incorporated in this design to produce the necessary precise pressure on-chip. Briefly, a small segment of a long microchannel is branched to attenuate the pressure generated from an external source (Figure 2-7B). The pressure divider circuit attenuates the pressure applied across the long microchannel by a factor ( $\alpha$ ) equal to the hydrodynamic resistance ratio of the small segment, in this case the bypass microchannels ( $R_B$ ), and the long microchannel ( $R_A$ ) (Equation 2-10).

$$\alpha = \frac{R_A}{R_B} + 1 \cong \frac{R_A}{R_B} \quad \text{Equation 2-10}$$

Hence, higher pressure divider ratio increases the ability of this mechanism to apply precise pressure on individual RBCs and consequently, to detect small differences in deformability between individual RBCs. Furthermore, the pressure attenuator ratio can be increased to generate as small pressure as possible and consequently, decrease the fluid flow rate in the loading microchannel to allow for easier loading (section 2.2.2.5). We found that  $\alpha > 300$  is sufficient to ensure successful cell loading.

### 2.3.5 Optimization of the multiplexed trans-dispersion device

To ensure consistent pressure is applied on each RBC in the deformation microchannel, the hydrodynamic resistance of different microchannels must follow the design rules described by Equation 2-5 and Equation 2-9. Specifically, to minimize multiplexing error,  $R_D/N$  needs to be much larger than both  $R_L$  and  $R_B$ , which can be achieved by maximizing  $R_D$  or minimizing  $N$ ,  $R_L$  and  $R_B$ . Since a deformation microchannel in trans-dispersion consists of a series of funnel-shaped constrictions, maximizing  $R_D$  means maximizing the hydrodynamic resistance of a funnel

( $R_F$ ). Based on the hydrodynamic resistance equation in Equation 2-11, where  $\mu$  is the viscosity of the fluid,  $L$ ,  $w$  and  $h$  are the length, width and thickness of the microchannel,  $R_F$  can be maximized by reducing the thickness ( $H_F$ ) and the pore size ( $W$ ) of the funnel or by increasing the length ( $L_F$ ) of the funnel. Furthermore,  $R_D$  increases with the number of funnels arranged in series in the deformation microchannel ( $N_F$ ).

$$R \approx \frac{12 * \mu * L}{wh^3(1 - 0.630h/w)} \quad \text{Equation 2-11}$$

As explained in section 2.3.1,  $W$  and  $H_F$  are constrained by the geometry of target cell so as to form a temporary seal between the cell and the constriction. The minimum width of the funnel ( $W_F$ ) is limited by the diameter of target cell, which is  $\sim 8 \mu\text{m}$  in RBC. Hence,  $W_F$  is designed to be  $10 \mu\text{m}$ . The length of the funnel ( $L_F$ ) is also limited by the diameter of RBC to prevent multi-cell loading in the deformation microchannel, leading to a funnel length of  $15 \mu\text{m}$  to be chosen. The number of funnels ( $N_F$ ) in the deformation microchannel can be increased to maximize  $R_D$  and to increase device sensitivity but this increases  $R_B$ , device size and analysis time as well (section 2.2.2.1). Consequently,  $N_F$  of 100 or 150 funnels is found to be optimum choice for maximizing  $R_D$  and sensitivity without affecting device size and analysis time.

For throughput consideration, the number of deformation microchannels ( $N$ ) should be as high as possible to capture as many cells. However, the length of the loading microchannel ( $L_L$ ) and consequently,  $R_L$  increases with  $N$ . As a result,  $N$  of 240 was found to be sufficient throughput without compromising the error requirement. The minimum length of the bypass microchannel ( $L_B$ ) is also dependent on  $N_F$ . Hence, the design options to minimize  $R_L$  and  $R_B$  are then limited to increasing the width ( $W_L$ ,  $W_B$ ) and the thickness ( $H_L$ ,  $H_B$ ) of loading and bypass microchannels, respectively.

The thickness of these two microchannels is constrained by the design errors (2.3.2 and 2.3.3) and the loading rate of individual cells into deformation microchannels (section 2.2.2.5) while the width of these two microchannels is limited by the aspect ratio requirement that microchannel width to the thickness must not exceed  $\sim 10:1$  to prevent microchannel collapse. To satisfy all these requirements, the width ( $W_L$ ,  $W_B$ ) and the thickness ( $H_L$ ,  $H_B$ ) of these two

microchannels is set to 150  $\mu\text{m}$  and 20  $\mu\text{m}$ , respectively for normal RBCs and malaria detection prototypes. Device prototype for drug-treated iRBCs requires 25  $\mu\text{m}$  microchannel thicknesses to satisfy the multiplexing error requirement. A summary table for all these parameters in each device prototype can be found in section 2.5.

## **2.4 Device operation**

### **2.4.1 Measurement process**

The measurement process began by bringing the cells into rectangular detour surrounding the deformation microchannels. The external pressure applied on the fluid reservoirs is then calibrated by adjusting the pressure until the fluid flow ceases and consequently, the cells remain stationary within the device. The cells are then loaded into the mouth of each deformation channel via the loading microchannel at a pressure that is insufficient for them to transit until the majority of the deformation microchannels are filled with cells. This small pressure is approximately 0.1 Pa above the null pressure and the loading time typically takes less than 2 minutes. As shown in our previous work [46], each RBC has its own characteristic threshold transit pressure hence, a much higher constant pressure than the threshold pressure is applied to transit the cells along the deformation microchannel.

After the deformation process, the applied pressure is shut off and the final position of each cell in the deformation microchannel is fixed and can be captured using automated imaging similar to visualization of DNA bands after gel-electrophoresis. After the position of the cells is captured, the external pressure is turned on again to flush out the cells. In some cases, for example in malarial-infected RBCs, a reverse pressure is first applied to flush out the cells captured in the beginning of the deformation microchannel. This approach enables high-throughput cell deformability studies to be performed at the single cell level since video recording is not required. This process takes  $\sim 10$  minutes and can be repeated as many times as necessary to obtain the necessary data points.

### **2.4.2 Applied pressure waveform**

A key parameter in trans-dispersion mechanism is the applied pressure waveform across the device. This parameter affects the transit speed of cells along the deformation microchannel

and consequently, their deformability. With pressure attenuator circuit incorporated in the design, the range of applied pressure is wide. The applied pressure needs to be sufficiently higher than the threshold transit pressure of normal RBCs to transit RBCs reliably. On the other hand, trans-dispersion device is more sensitive in separating cells with different deformability when the applied pressure is low since each cell is given enough time to deform back to its original shape after it is squeezed through each constriction. However, a low applied pressure also increases processing time since cells will take more time to transverse along the deformation microchannel.

With this consideration, it is hypothesized that a downward stepwise pressure waveform is the best course of action. Once the majority of deformation microchannels are loaded with RBCs, a much higher pressure than the threshold pressure,  $P_1$  is applied for a period of time and then reduced to  $P_2$  (Figure 2-8A) to optimize for both measurement sensitivity and processing time. A downward stepwise pressure waveform is found to be better than an upward waveform to prevent non-transiting cells (cells that cannot transit beyond the first funnel) from escaping when the pressure waveform is brought down to the null pressure.

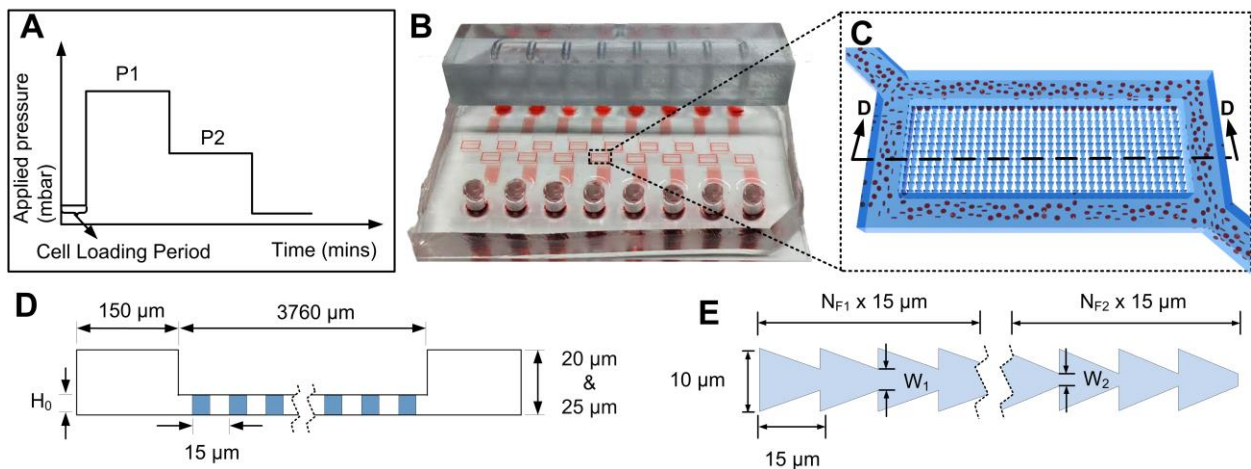


Figure 2-8: (A) Pressure waveform applied across the device. (B) The trans-dispersion chip with 8 parallel trans-dispersion arrays. (C) 3D model of the trans-dispersion array. (D) Cross-section of the device showing the geometry of bypass, loading and deformation microchannel. (E) Detailed design of the deformation microchannel, where  $N_F$  is the number of constrictions and  $W$  is the constriction diameter. A two-stage device will have different pore size where  $W_{0,1}$  is greater than  $W_{0,2}$ .

### **2.4.3 Manifold to multiplex array**

Since trans-dispersion does not require video microscopy, a single trans-dispersion chip (Figure 2-8B) can consist of several individual and independent trans-dispersion arrays (Figure 2-8C). Depending on the device prototype, one chip consists of 4 or 8 independent arrays of trans-dispersion device with their own fluid reservoirs. An external pressure source is applied through a 4- or 8-fold pressure manifold fabricated using stereolithography (FineLine Prototyping, MN, US) (Figure 2-8B). The pressure manifold is inserted into the fluid reservoir for each array, enabling on-chip sample loading and hence, minimizing the sample volume required for each experiment. More importantly, since the fluid reservoirs are independent of each other, different samples can be loaded into each array and tested simultaneously.

### **2.5 Device prototypes based on target cells**

Each trans-dispersion prototype is designed with a specific target cell in mind. The width ( $W_B$ ,  $W_L$ ) of bypass and loading microchannels are designed to be 150  $\mu\text{m}$  and remain constant in all these four prototypes (Figure 2-8D). The length ( $L_F$ ) and width ( $W_F$ ) of the funnel is 15  $\mu\text{m}$  and 10  $\mu\text{m}$ , respectively (Figure 2-8E). The number of deformation microchannels ( $N$ ) of 240 also remains constant in these four prototypes. The remaining device geometries are detailed in Table 2-3.

Table 2-3: Details of device geometries based on the target cells

Target Cells	Normal RBCs	<i>P. falciparum</i> ring-stage iRBCs	<i>P. falciparum</i> late-stage iRBCs	Antimalarial drug-treated iRBC
Manifold	4	8	8	8
Device Type	One-stage	Two-stage	Two-stage	Two-stage
Number of funnels in a deformation microchannel ( $N_F$ )	100	1 <sup>st</sup> stage:75 2nd stage: 75	1 <sup>st</sup> stage:75 2nd stage: 75	1 <sup>st</sup> stage:75 2nd stage: 75
Pressure attenuator ratio ( $\alpha$ )	500	500	500	300
Pore Size, $W$ ( $\mu\text{m}$ )	1.7	1 <sup>st</sup> stage: 1.5 2nd stage: 1.2	1 <sup>st</sup> stage: 2.0 2nd stage: 1.5	1 <sup>st</sup> stage: 2.4 2nd stage: 1.9
Thickness of deformation microchannel $H_F$ ( $\mu\text{m}$ )	$3.8 \pm 0.1$	$3.7 \pm 0.1$	$3.9 \pm 0.1$	$4.4 \pm 0.1$
Thickness of Bypass, $H_B$ and Loading Microchannel, $H_L$ ( $\mu\text{m}$ )	20	20	20	25
$R_D$ (Pa.s/m <sup>3</sup> )	3.91E+17	6.57E+17	4.12E+17	2.15E+17
$R_L$ (Pa.s/m <sup>3</sup> )	7.12E+13	8.41E+13	8.41E+13	4.40E+13
$R_B$ (Pa.s/m <sup>3</sup> )	4.26E+12	1.07E+13	1.07E+13	6.48E+12
$E_M$	4.36%	3.06%	4.87%	4.90%
$E$	0.26%	0.39%	0.62%	0.72%
Loading Ratio	0.02%	0.01%	0.02%	0.02%

## 2.6 Relationship to previous work

Two previous students, Quan Guo and Marie-Eve Myrand-Lapierre contributed to the development of this trans-dispersion project. The single fluidic plunger mechanism was designed by Guo Quan and achieved sufficient sensitivity to differentiate malarial-infected RBCs from uninfected RBCs with a throughput of ~10 cells per hour [21]. Marie-Eve Myrand-Lapierre multiplexed the single fluidic plunger mechanism and achieved a throughput of ~100 cells per hour [46].

However, to be clinically viable, a device with a much higher throughput and ability for parallelized sample processing is needed. The two key advantages of trans-dispersion mechanism over the fluidic plunger mechanism is the use of repeated deformation to minimize the effect of pore size variations and the potential to dramatically increase the number of deformation microchannels and the number of constrictions in each deformation to achieve a high throughput and sensitivity. The original contributions presented in this document are described below:

1. Achieved a more sensitive measurement by the use of repeated deformations in a single deformation microchannel
2. Achieved higher throughput by eliminating the need for video microscopy
3. Achieved multiple sample processing by the manifold design
4. Optimized hydrodynamic resistance of microchannels to minimize error and maximize throughput and sensitivity
5. Characterized the optimal operating conditions of the mechanism on device-to-device basis for different target cells
6. Characterized the sensitivity of the device by detecting the changes in RBC deformability due to the fixation of glutaraldehyde
7. Detected malarial-infected RBCs
8. Assessed the antimalarial drug-efficacy by the changes in RBC deformability

## Chapter 3: Material and Methods

This chapter describes all the materials and methods used in the experiments of this thesis. To fabricate the microfluidic devices, photolithography (section 3.1) and soft-lithography (section 3.2) are carried out. Section 3.3 describes how different biological samples, such as healthy RBCs (section 3.3.1), oxidatively damaged RBCs (section 3.3.2), *P. falciparum*-infected RBCs (iRBCs) (section 3.3.3) and drug-treated iRBCs (section 0) are prepared. Section 3.4 details the experimental process while section 3.5 and 3.5 describe the analysis carried out on the experimental data.

### 3.1 Fabrication of silicon masters/photolithography

Master wafers for the trans-dispersion devices were fabricated on silicon wafer substrates using the photolithography process, illustrated in Figure 3-1. This process prints a pattern from a photomask onto a light-sensitive photoresist, SU-8 (MicroChem, Newton, MA, USA), a chemical that changes its solubility when exposed to UV light. SU-8 is a negative photoresist that becomes insoluble when it is exposed to UV light. As such, the photomask used, is an opaque sheet with a transparent pattern.

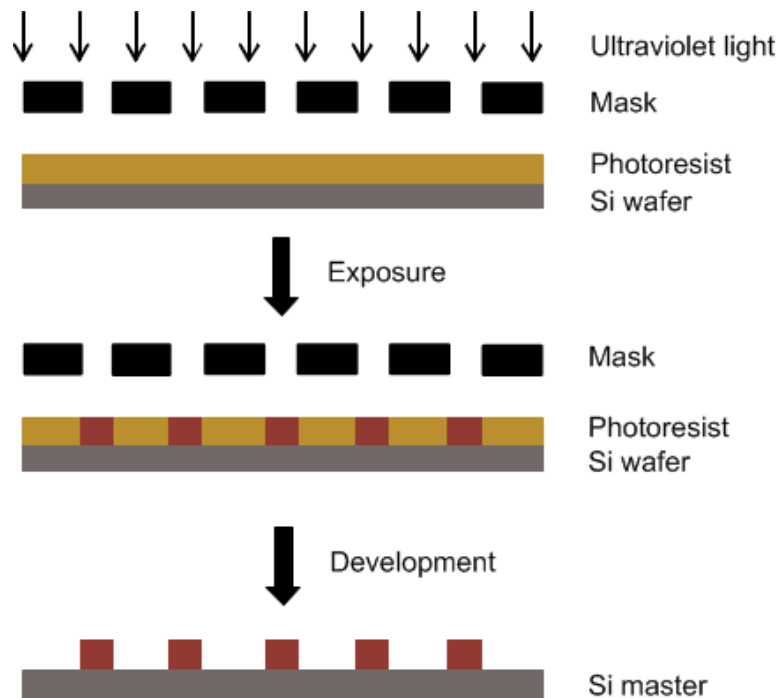


Figure 3-1: Schematic of the photolithography process

The features on the wafer consist of three layers of photoresist with different thickness. The first layer contains the deformation microchannels and was fabricated using SU8-3005 (MicroChem, Newton, MA, USA) or SU8-3005 thinned with cyclopentanone to create devices with thicknesses ranging from 3.7  $\mu\text{m}$  to 4.5  $\mu\text{m}$ , depending on the hypothesized rigidity of target cells (Table 3-1). SU8-2007 was used to fabricate the second layer with  $\sim 7$   $\mu\text{m}$  thickness. The second layer serves as an alignment layer so that the thin, first layer can be visualized when the third layer was laid on top of it. SU8-3025 was used to fabricate the last layer that contained the remaining microstructures with  $\sim 20$   $\mu\text{m}$  thicknesses. The patterns for the microstructures were drawn using DraftSight. The thicknesses of the microstructures were measured using a profilometer (Alpha Step 200). The fabrication processes of these three layers were detailed below:

1. A 100 mm blank silicon wafer was cleaned with acetone, methanol and then isopropanol after which they were dried with nitrogen gas.
2. The cleaned wafer was baked at 200°C for 5 minutes to completely dehydrate it.
3. SU-8 3005 was spun at different speeds to produce different thicknesses of deformation microchannel depending on the target cells (Table 3-1). SU8-2007 was spun at 3000 rpm for 30s while SU8-3025 was spun at 4000 rpm for 30s.
4. The wafer with SU8-3005 photoresist was soft-baked at 95°C for 2 minutes for SU8-3005 or at 65°C, 95°C and 65°C for 1:2:1 minutes and 1:5:1 minutes for SU8-2007 and SU8-3025 respectively.
5. When applicable (second and third layer), the mask was aligned with previous features on the wafer.
6. The wafer was exposed to UV light in a mask aligner (Canon) for 30 – 40s, 55s and 60s for SU8-3005, SU8-2007 and SU8-3025 respectively.
7. The exposed wafer was then given a post-exposure bake (PEB) at 95°C for 2 minutes for SU8-3005 or at 65°C, 95°C and 65°C for 1:2:1 minutes and 1:4:1 minutes for SU8-2007 and SU8-3025 respectively.
8. The baked wafer was developed for 1-2 minutes with SU8 developer. It was then washed with isopropanol and dried with nitrogen.

9. After the wafer was dried, the wafer was further baked on a hotplate to further stabilize the structures. The hotplate temperature is gradually ramped from 40°C to 200°C at a rate of 60°C per hour, held at 200°C for one hour, and then gradually cooled to 40°C at a rate of 200°C per hour.

Table 3-1: Spin speed settings of SU8 photoresists to produce the desired layer thickness

Target Cells	Photoresist	Spin Speed (rpm)	Thickness (μm)
RBCs	SU-8 3005 and thinner at 2:1 ratio	600	3.7 ± 0.1
<i>P. falciparum</i> ring-stage iRBCs	SU8-3005	6000	3.7 ± 0.1
<i>P. falciparum</i> late-stage iRBCs	SU8-3005	4000	3.9 ± 0.1
Antimalarial drug-treated iRBC	SU-8 3005 and thinner at 3:1 ratio	800	4.4 ± 0.1

### 3.2 Fabrication of PDMS devices/soft-lithography

Microfluidic devices were made using soft lithography of polydimethylsiloxane (PDMS) silicone, as illustrated in Figure 3-2. To minimize degradation of the master silicon wafer, polyurethane-based (Smooth-Cast ONYX, Smooth-On) molds were fabricated as a replica of the master wafers via a process described by Desai et al [57]. Microfluidic devices were made by mixing Sylgard-184 PDMS (Ellsworth Adhesives) base at a ratio of 10:1 (w/w) to its hardener, after which the mixture was poured into the replica mold and degassed for 15 minutes. The device was then baked for 2 hours at 65 °C and reservoir holes were punched on the device using a 4 mm hole punch (Technical Innovations, Angleton, TX, USA). A thin layer of RTV615 PDMS (10:1 ratio of base to hardener) was spin-coated onto a blank wafer and baked for 1 hour at 65°C. The microfluidic device and the PDMS coated wafer were bonded together after oxidizing them separately in oxygen plasma chamber (Harrick Plasma, Ithaca, NY) for 80s. For the final step, the resulting device was bonded to a 50 x 75 mm glass slide (Fisher Scientific).

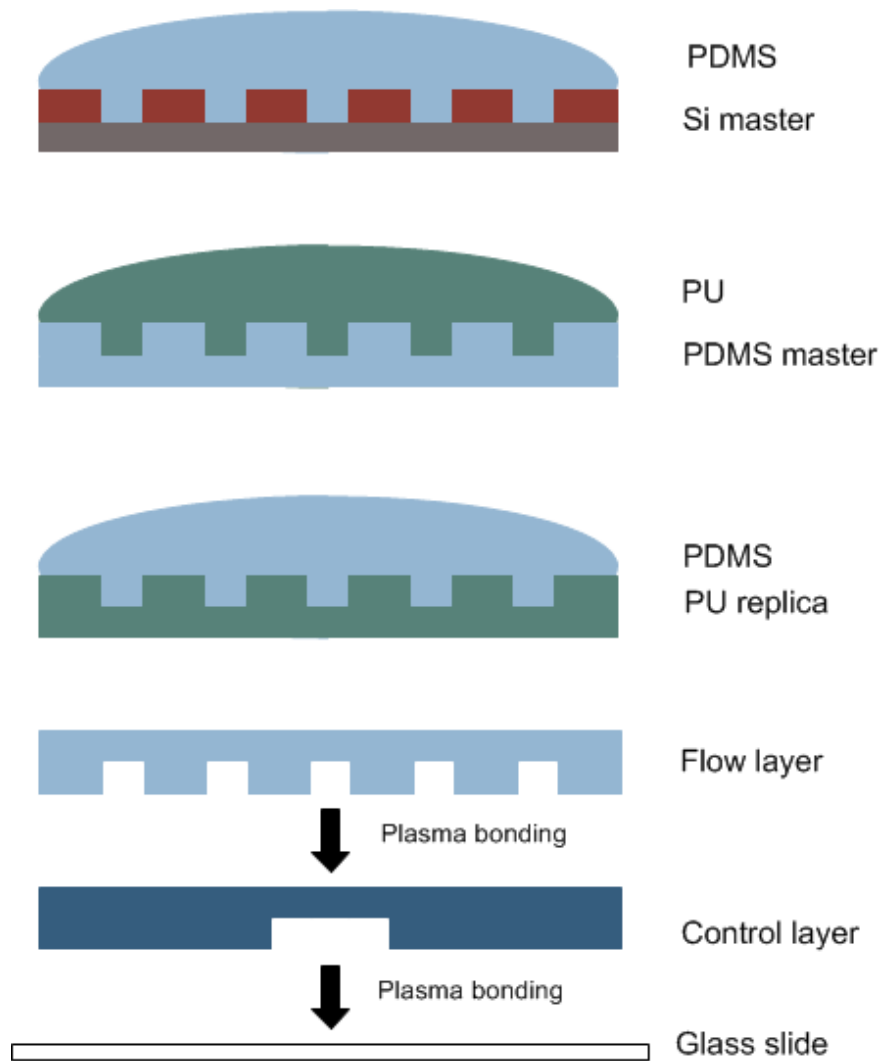


Figure 3-2: Schematic of the soft lithography process.

### 3.3 Sample preparation

#### 3.3.1 Healthy RBCs

Device validation was performed using normal fresh whole blood obtained from consenting donors by finger-prick (Unistik 3, Owen Mumford, Fisher) or venipuncture. The whole blood was washed 3 times with PBS and was diluted to 20% hematocrit in a buffer solution containing Phosphate Buffered Saline (PBS, Gibco) and 0.2% Pluronic F127 (Sigma). Pluronic was added to reduce the effect of friction within the device [58].

### 3.3.2 Oxidatively damaged RBCs

Device sensitivity experiments were performed using whole blood that was chemically treated to reduce deformability by mild fixation using glutaraldehyde (GTA). GTA is known to rigidify RBCs by cross-linking proteins in the cell membrane. By increasing the GTA concentration, a sample with a known trend in deformability profile is obtained. GTA was added to RBCs at 5% hematocrit at a concentration between 0.0005-0.002% and incubated at room temperature for 30 minutes. After the incubation period, the sample was washed 3 times with PBS and finally, the GTA-treated blood samples were diluted to 20% hematocrit in PBS with 0.2% Pluronic added to it.

### 3.3.3 Culture and synchronization of *P. falciparum* malaria

RBCs infected with *P. falciparum* (3D7 strain) were prepared using standard *in vitro* culture methods. The *P. falciparum* 3D7 strain was obtained from Prof. Petra Rohrbach (McGill University, Canada). Donor RBCs with A+ and O+ blood type were obtained with informed consent from Canadian Blood Services and were used to maintain the *P. falciparum* culture. The culture was incubated in an hypoxic chamber (3% O<sub>2</sub> and 5% CO<sub>2</sub>) at 37°C and was suspended at 5% hematocrit in complete RPMI-1640 culture media (Invitrogen) containing 25mM HEPES (Sigma), 0.5% (wt/vol) AlbuMAX I (Life Technologies), 100µM hypoxanthine (Sigma), 12.5µg/ml gentamicin (Sigma) and 1.77mM sodium bicarbonate (Sigma). Cultures were grown in 75-cm<sup>2</sup> culture flasks (Sigma). Before each experiment, parasitemia level was measured using Giemsa staining (Sigma-Aldrich) [59], in which the Giemsa stain was diluted at a 1:2 volume ratio with PBS. Infected RBCs (iRBCs) were then diluted using uninfected blood to the desired parasitemia level. The uninfected blood followed the same incubation period as the iRBC sample and was used as the control for every experiment involving malaria detection.

Cultures were synchronized by sorbitol lysis to obtain iRBCs at specific stages of parasite growth as described by Radfar, et al [59]. Briefly, cultures were checked using Giemsa stain to judge the parasitemia status and hence, the synchronization window. When the cultures contained >50% of the ring-stage parasites, the cultures were treated with 5% Sorbitol (Sigma) at 9-10 volumes of the RBC pellet volume (Figure 3-3). The cultures were incubated at 37°C for 8 minutes in a water bath. After incubation, they were washed 3 times with RPMI medium. After

synchronization, the cultures were incubated in a hypoxic chamber for at least one parasite life-cycle (~48 hours) before they were harvested. Giemsa stain was used to count the parasitemia level before diluting the iRBC sample with uninfected blood to the desired parasitemia level. Cultures were synchronized using Sorbitol treatment once a week.

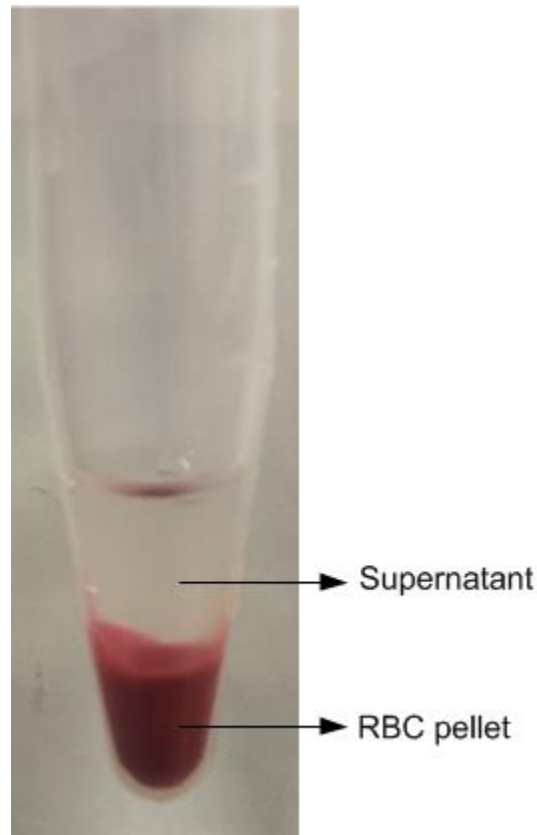


Figure 3-3: Illustration of the RBC pellet after centrifugation.

### 3.3.4 Purification of *P. falciparum*-infected RBCs and drug treatment

Purified iRBCs were obtained by passing the culture sample through a LS column (Miltenyl Biotec) surrounded by Neodymium Super Magnets (Applied Magnets) (Figure 3-4) [60]. Malarial parasites feed on hemoglobin and release an iron-containing heme, which is converted by the parasites into a crystalline form, called hemozoin. Since these iron-containing hemozoin was present in late-stage iRBCs, they were held in the magnetic column and could be extracted from the column using a syringe. Columns were washed once with 5 ml RPMI medium, after which the column was transferred into a 15 ml Falcon tube (Fisher Scientific) and eluted again with 5 ml RPMI medium.

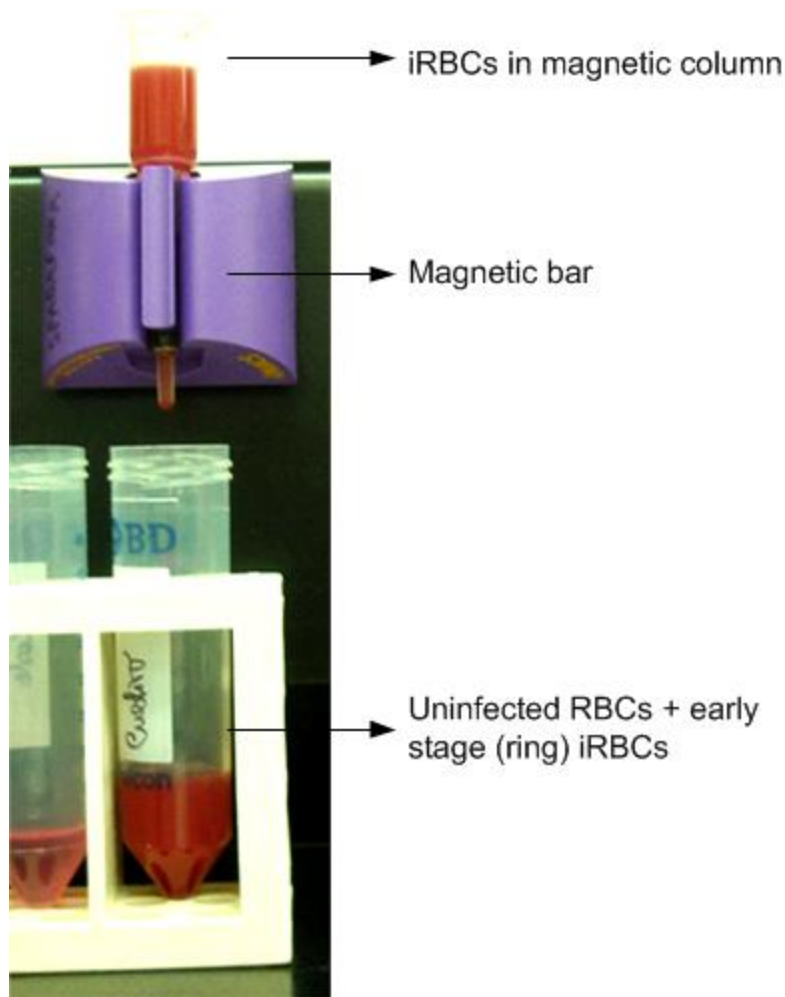


Figure 3-4: Magnetic purification of iRBCs to obtain late-stage iRBCs only

The purified iRBCs were resuspended in RPMI medium and incubated for 30 minutes in the hypoxic chamber, after which the parasites were treated with various anti-malarial drugs at different concentrations for 4 hours. Known drugs were tested at concentrations  $>EC_{50}$  of each drug:  $1\mu\text{M}$  chloroquine,  $1\mu\text{M}$ ,  $20\text{nM}$  pyrimethamine,  $100\mu\text{M}$  proguanil,  $10\text{nM}$  artesunate,  $8\text{nM}$  artemether,  $20\text{nM}$  dihydroartemisinin,  $100\mu\text{M}$  tetracyclines,  $250\text{nM}$  atovaquone,  $1.08\mu\text{M}$  dihydroisoquinolone - SJ733 and  $3.6\text{nM}$  for spiroindolone NITD 246 [61–64]. Since drugs were diluted in DMSO, untreated iRBCs were treated with 0.01% DMSO and acted as the control.

### 3.4 Experimental setup and protocol

Instrumentation for the cell transport dispersion device consisted of an optical imaging system, a pneumatic pressure control system and a personal computer (PC) (Figure 3-5). The

imaging system included an inverted microscope (Nikon) to observe the microfluidic device using a 4X objective and a high-resolution camera (Graftek Imaging, TX, US). The camera system acquired images to observe the cell loading process and captured the final position of the cells after transporting them in the deformation microchannel. A low microscope magnification and a high camera resolution were used to detect as many cells as possible in each camera frame. The pneumatic pressure control system applied a variable pressure to the sample and fluid reservoirs in order to first load the sample cells and then transport them through the deformation microchannels. The variable pressure was generated using a Fluigent (Paris, France) pressure control system and was controlled from the PC.

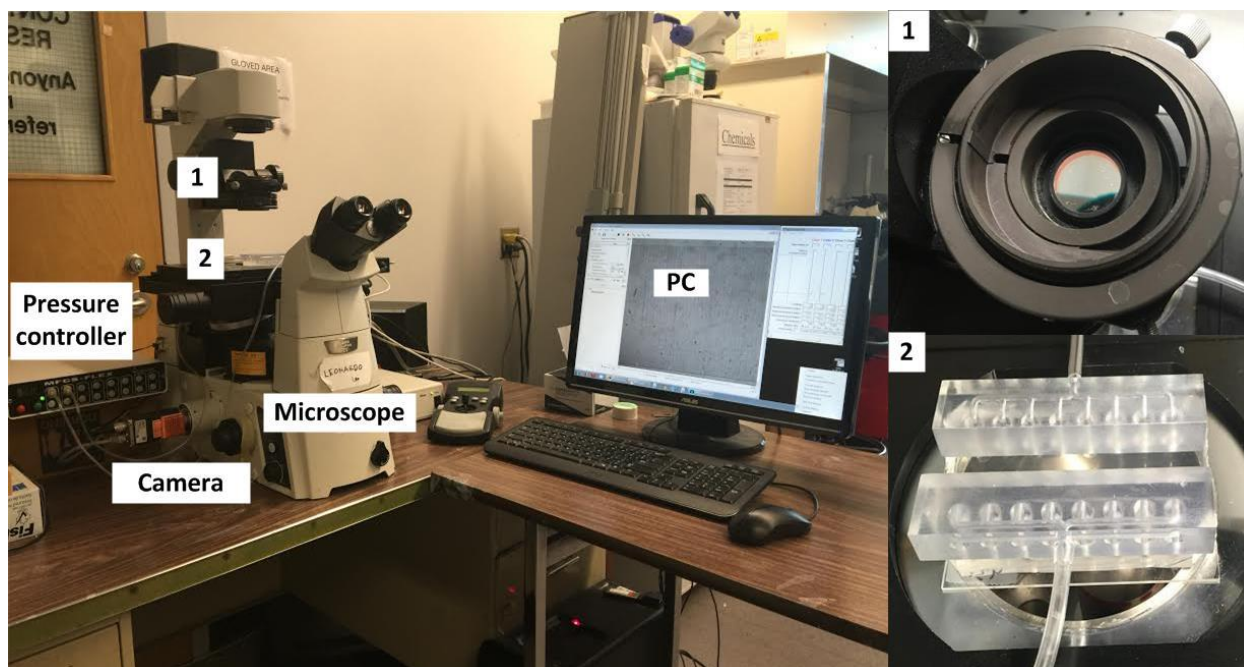


Figure 3-5: A photograph of the experimental system. The PC controls the pressure controller system and captures the final positions of the cells using the microscope and the camera. (1) Bandpass filter. (2) Photograph of the trans-dispersion device with manifold.

To begin an experiment, buffer solution was loaded into both fluid reservoirs to fill up the device. Once all the microchannels were filled, a small amount of RBCs (1-2  $\mu\text{l}$ ) was carefully placed at the entrance of the network in the outlet reservoir and was brought towards the deformation area using reverse pressure. RBCs were prevented to flow all the way to the inlet to prevent buffer contamination. Once sufficient deformation microchannels were loaded with RBCs, the measurement process described in section 2.4.1 began. There were several reasons for this reverse loading: first, the probability of multiple cells loading into one deformation

microchannel would be decreased when buffer quickly cleared the RBCs after the deformation pressure was applied; second, the amount of sample required was reduced since there was no need to fill the whole fluid reservoir area; third, there was no need to continuously replace the buffer in the inlet reservoir even when the sample was changed if RBCs were prevented from reaching this area, reducing the risk of introducing debris into the device.

Image processing software, developed in-house by Jeong-Hyun Lee, was used to measure the final position of the cells after the deformation pressure waveform was applied (Figure 3-6). A bandpass filter (Edmund Optics, US) was used to produce sharper image contrast between RBCs and the microchannels for easier detection by the image processing software. The filter only passes light with a wavelength of 420 nm, which is absorbed by RBCs, making RBCs appear black. Users set the reference positions within the device image. These reference positions refer to the beginning and the end of alignment markers that were incorporated for every 40 parallel deformation microchannels. These alignment markers also contained dots for every 10 funnels along the deformation microchannel to increase software accuracy in detecting the cells position. Using these reference positions, the software could adjust a slightly crooked image.

Next, this software detected RBCs by allowing users to set a reference RBC, after which it would automatically recognize cells similar to this reference RBC (Figure 3-6, red squares). Similarity between detected cells and reference cells was 94.5% on default but could be changed from 91% to 98%. For higher measurement accuracy, the software also gave users the ability to manually select the cells that the software might miss (Figure 3-6, yellow squares). A potential source of error occurs when multiple cells enter one deformation microchannel. The image processing software removes these cells from the final measurement.

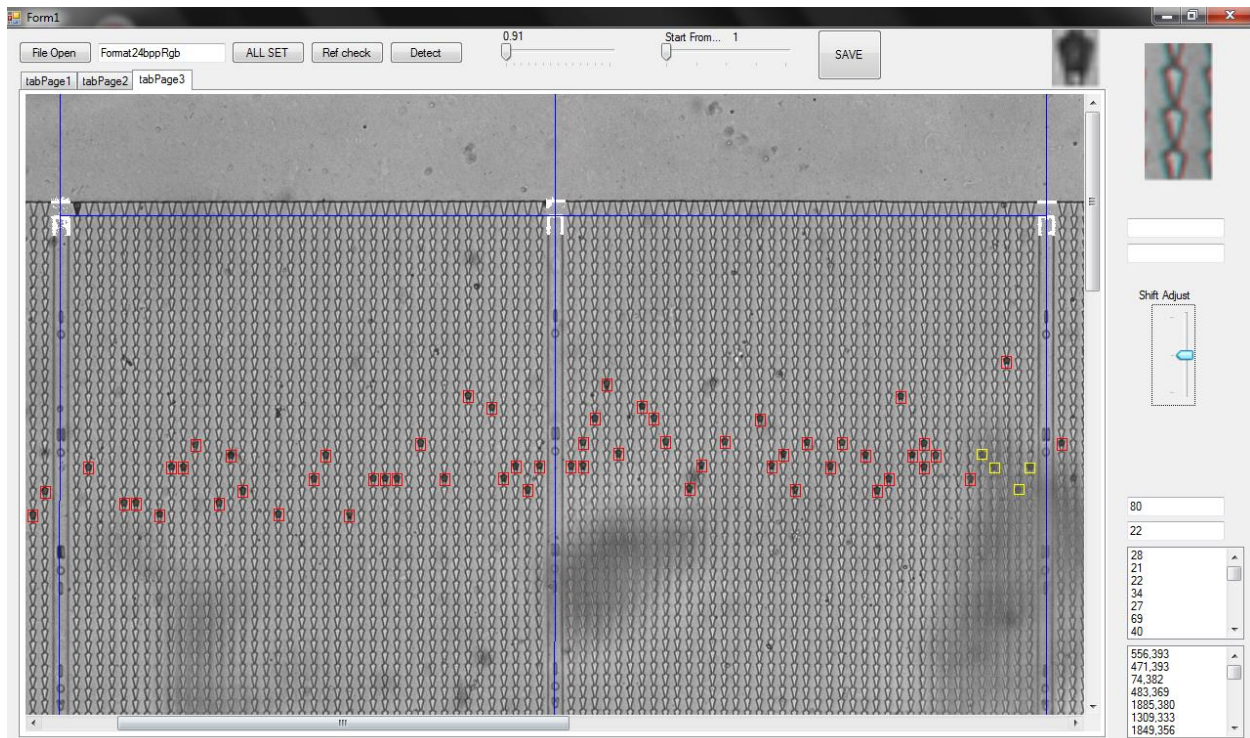


Figure 3-6: Image processing software used to automatically detect RBCs. Red squares indicate automatic detection by the software while yellow squares indicate manual selection by the user.

For each device prototype fabricated, the sizes of 120 randomly chosen funnels in each device was measured using software developed in-house by Richard Ang (Figure 3-7). The software detected the edges of the constrictions, which were visualized under fluorescence microscopy with a 60X objective. The average constriction size variation within a device was found to be less than 5%, provided that there was no defect in the deformation microchannel.

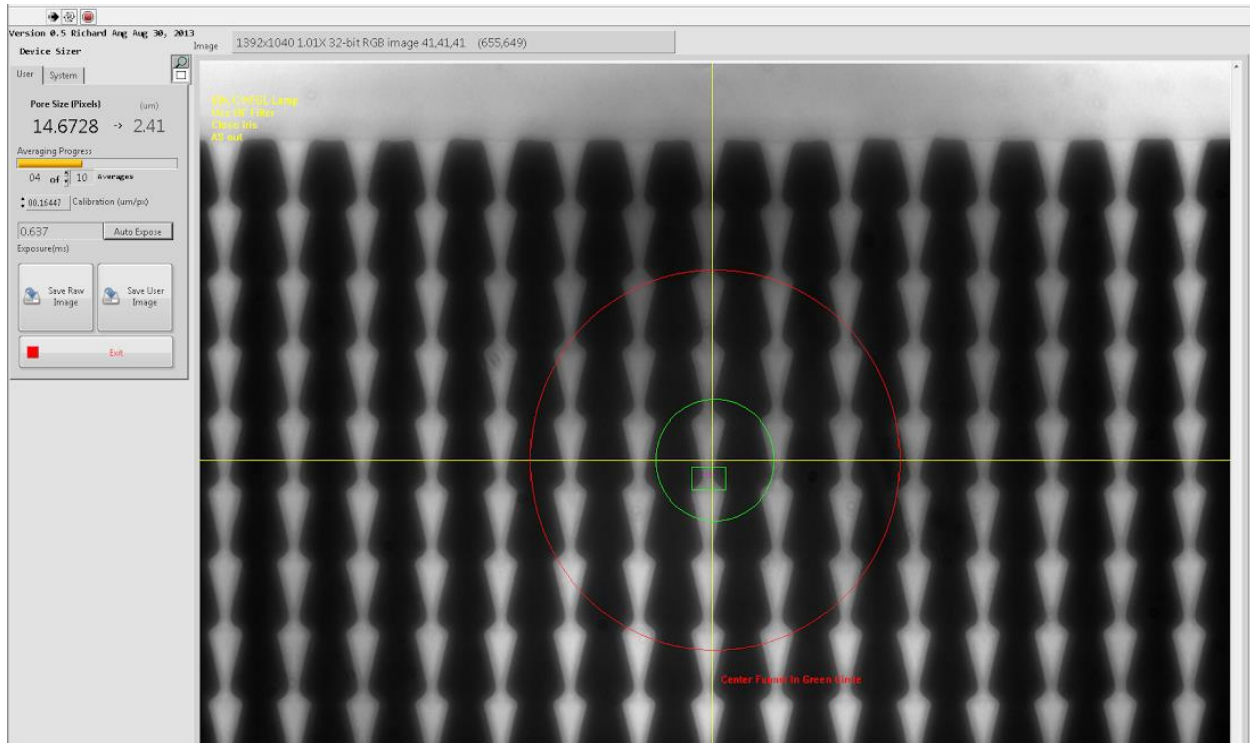


Figure 3-7: Interface of the software used to measure the constriction size.

### 3.5 Data analysis

Due to inherent variability in donors, each experiment was normalized to a sample, which was designated as the control of that experiment (Table 3-2). Data normalization is performed by dividing the position (indicating the deformability) of each cell to the mean and median of the control sample. Samples were normalized to the mean of the control when the expected distribution of the cells is Gaussian, such as with the device validation experiments outlined in section 4. Parasitized RBCs were also normalized to the mean-value since iRBCs form a very small subpopulation in the sample, resulting in an overall Gaussian distribution. However, iRBCs treated with antimalarials was normalized to the median of the control since the expected population distribution is not Gaussian. This normalized deformability measurement is usually denoted as normalized position of the cells along the deformation microchannel.

Table 3-2: Summary of data analysis process for each experiment.

Thesis Section	Experiment	Sample Designated as Control	Normalized To
4.3	Repeated deformations	2 minutes at 100 mbar	Mean-value
4.4	Applied pressure waveform	Untreated RBCs at 25 mbar	Mean-value
4.5	Multiplexing error	Nearly empty	Mean-value
4.6	Oxidatively damaged RBCs	Untreated RBCs	Mean-value
5.1	<i>Plasmodium falciparum</i> iRBCs	Uninfected RBCs	Mean-value
		Individual sample to produce the cumulative distribution	Mean-value
5.2	Antimalarial-treated iRBCs	DMSO-treated late-stage iRBCs	Median-value

The small subpopulation of malaria-iRBCs (unsynchronized or ring-stage) becomes progressively stiffer as the parasites mature and also causes bystander injury on the uninfected, exposed RBCs. Hence, to capture the effect of this key subpopulation and to eliminate the effect of uninfected RBCs in the deformability measurement, each sample was normalized to the mean of individual sample, after which the least deformable subpopulation was emphasized in the data analysis by sorting the cells according to its normalized position. The mean of 1% to 100% of the least deformable population fraction was then plotted to obtain a cumulative distribution profile of each sample, which is referred to as the deformability profile of that sample.

### 3.6 Statistical analysis

When more than two groups of samples were investigated, an ANOVA (Analysis of Variance) test was performed, after which an unpaired t-test was used to compare two groups of interest. Mean with the standard deviation (SD) was plotted for healthy and oxidatively damaged RBCs while median with interquartile range (IQR) was plotted for parasitized RBCs and trophozoites treated with DMSO or drugs. Linear regression was used in 4.1, 4.3 and 5.1.3, while non-linear regression was used in section 4.4 to determine the relationship between two parameters. The coefficient of determination ( $r^2$  for linear regression and  $R^2$  for non-linear regression) was used to indicate how good the data fits the statistical model. All statistical analysis was done using GraphPad Prism v6 software (Graphpad Software, US).

## Chapter 4: Device Characterization

Chapter 4 describes the characterization process of the trans-dispersion mechanism. Section 4.1 describes how the flow direction in the device was selected. Section 4.2 briefly validates the trans-dispersion mechanism for measuring the deformability healthy red blood cells (RBCs) from various donors while section 4.3 details how repeated deformations minimize the effect of pore-size variances on the deformability measurement of RBCs. Section 4.4 and 4.5 validates the device mechanism by assessing the optimized applied pressure waveform and the multiplexing error. Section 4.6 and 4.7 discusses the sensitivity and throughput of the mechanism. Unless specified, all the experiments in this section were conducted using the prototype intended for normal RBCs, a one-stage device with a pressure divider ratio of 500:1, deformation microchannel thickness ( $H_0$ ) of  $3.7\mu\text{m}$  and average pore size of  $1.7\mu\text{m}$ .

### 4.1 Direction of fluid flow

The first parameter to consider when determining the optimum operating condition for trans-dispersion is the direction of fluid flow in the deformation microchannels. Forward and reverse flows are defined as the flow direction along and against the taper direction of the funnel, respectively (Figure 4-1).

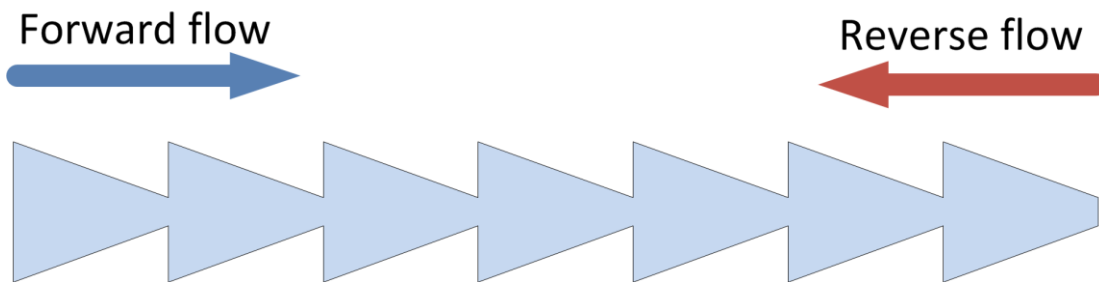


Figure 4-1: Illustration of the two possible fluid flow directions in the deformation microchannel.

As mentioned previously [21], the stiffness of each cell is directly proportional to the threshold pressure required to push it through the constriction. Hence, the linearity between the threshold pressure and the velocity (Figure 4-2) can be used to determine whether a forward or reverse flow should be used for a more consistent measurement of RBC deformability in the trans-dispersion device.

To determine this correlation, video recordings were taken for ~10 cells to determine the threshold pressure required to push each cell through the first constriction. A pressure of 75 mbar was then applied and the final position of these cells was then captured to calculate the speed of each cell. The result of this experiment (Figure 4-2) shows that forward flow had better linearity ( $r^2=0.66$ ) than the reverse flow ( $r^2=0.24$ ). Hence, forward flow was chosen as the default flow direction from this point on. It should be noted that this was a result of triplicate experiments using 3 different donors, which reduces the  $r^2$  value of the experiments.

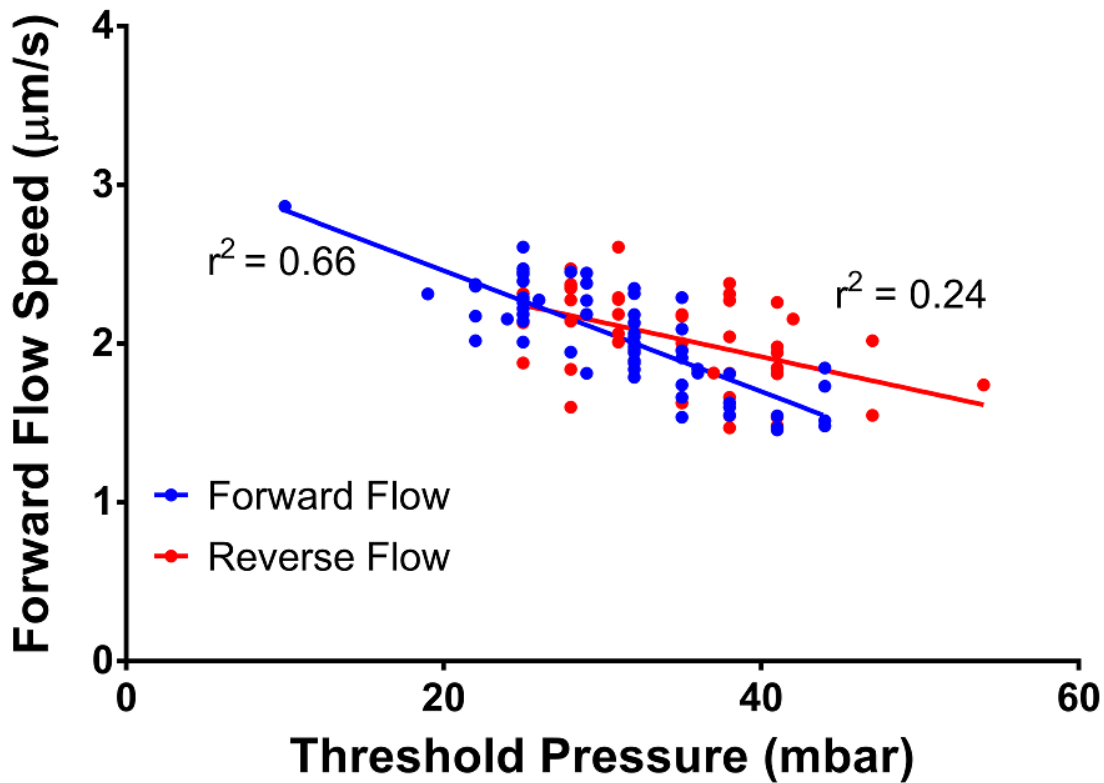


Figure 4-2: Correlation between the threshold pressure and the speed of each cell shows that forward flow produces a more consistent measurement of transit speed ( $r^2=0.66$ ,  $n=62$ ) than the reverse flow ( $r^2=0.24$ ,  $n=49$ ).

## 4.2 Healthy RBCs

To first validate the use of the trans-dispersion mechanism in measuring the deformability of RBCs, fresh healthy RBCs are obtained by finger-prick from donors, after informed consent, in order to assess donor variability. These normal RBCs were measured using a one-stage device with a pressure divider ratio of 500:1, deformation microchannel thickness ( $H_0$ ) of 3.7 µm and average pore size of 1.8 µm.

The result (Figure 4-3) shows that there is indeed an inherent variability between donors, which may be caused by several factors such as metabolism [65], diet and exercise [66,67] or exposure to pharmacologic agents [68,69]. As expected, the scatter plot of fresh RBCs has a normal distribution, validating that the trans-dispersion mechanism can be used to assess healthy RBC deformability. To overcome this donor variability, subsequent experiments would be normalized to the mean or median value of a corresponding control (Table 3-2) when different donors were used.

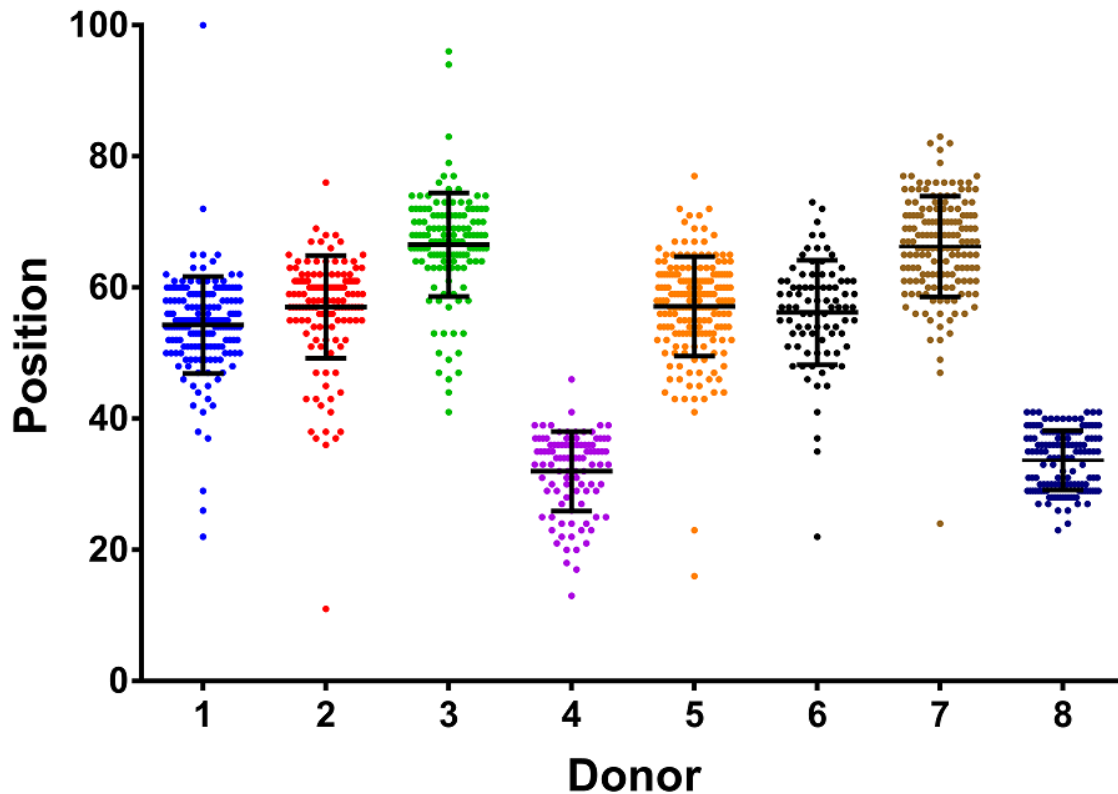


Figure 4-3: Measured deformability of different donors shows variability between donors ( $n \geq 99$ ).

### 4.3 Repeated deformations

To first establish that repeated deformation of RBCs through micro-scale constrictions is an elastic and memoryless process, the position of single cells as a function of time for different applied pressures was measured. For 300 mbar applied pressure, RBCs would escape the deformation microchannel when the pressure was applied longer than 6 minutes, hence limiting the data collection up to this time point. The linearity of these results ( $r^2 \geq 0.94$ ) demonstrates that this process does not change the properties of the RBCs and that the transport process is

sufficiently consistent to overcome the variations in constriction geometry (Figure 4-4). This experiment is performed in triplicate with different donors and as such, each donor data is normalized to the mean value of the 2 minutes data point at 100 mbar for the purpose of eliminating donor variance.

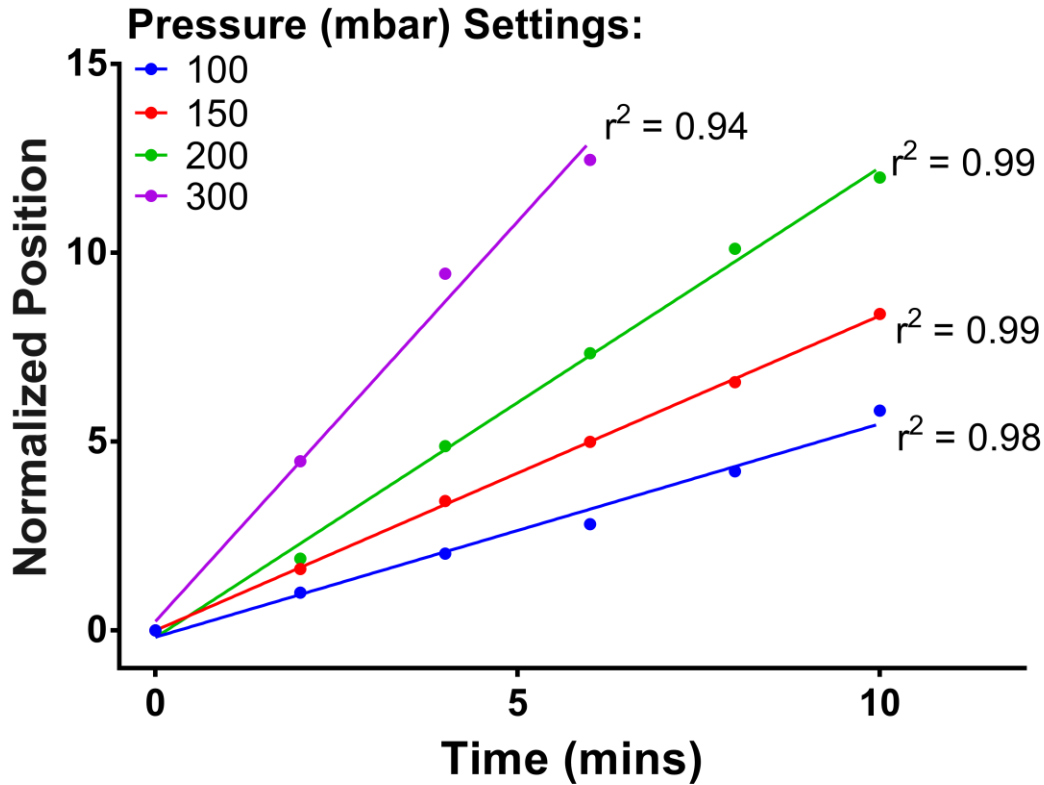


Figure 4-4: Constant speed is observed in 4 test parameters, which indicates the elastic properties of RBCs undergoing repeated deformations and the averaging effect of constriction geometry variations ( $n \geq 125$ ). Experiment is performed in triplicate with three different donors and each donor data is normalized to their corresponding 2 minutes at 100 mbar data point.

#### 4.4 Optimization of applied pressure waveform

One of the key challenges for the operation of the trans-dispersion mechanism is in determining the applied pressure waveform that will yield the highest sensitivity measurements of RBC deformability. To evaluate this, the deformability profiles of RBC samples treated with small amounts of glutaraldehyde (GTA) were measured. GTA is a common fixative agent, which induces cross-linking and stabilization of proteins in the red blood cell membrane and thus artificially reduces their deformability in a concentration dependent manner [70].

The experiment was performed using 0% and 0.0005% glutaraldehyde-treated RBCs at constant pressures of 25, 50, 75, 100, 150, 200, 300 and 600 mbar. The applied pressure was shut off when the first cell reached the 90<sup>th</sup> funnel. The same running time was applied for both samples to assess the ability of the trans-dispersion mechanism in resolving the change in RBC deformability between these two samples.

The result (Figure 4-5) shows that the device’s sensitivity experiences exponential decay ( $R^2 = 0.97$ ) with applied pressure. This decay is expected, because with a high pressure, RBCs are mainly kept at their deformed, ‘bullet’ shape for the majority of the time. This phenomenon is illustrated in Figure 4-6, where at 75 mbar, the RBC is given sufficient time to deform through each constriction and recover to its normal, discoid shape while at 600 mbar, the RBC barely has the time to recover before being deformed in the next constriction, hence decreasing the device’s sensitivity. Each sample is normalized to the mean value of the untreated sample at 25 mbar for the purpose of eliminating donor variance.

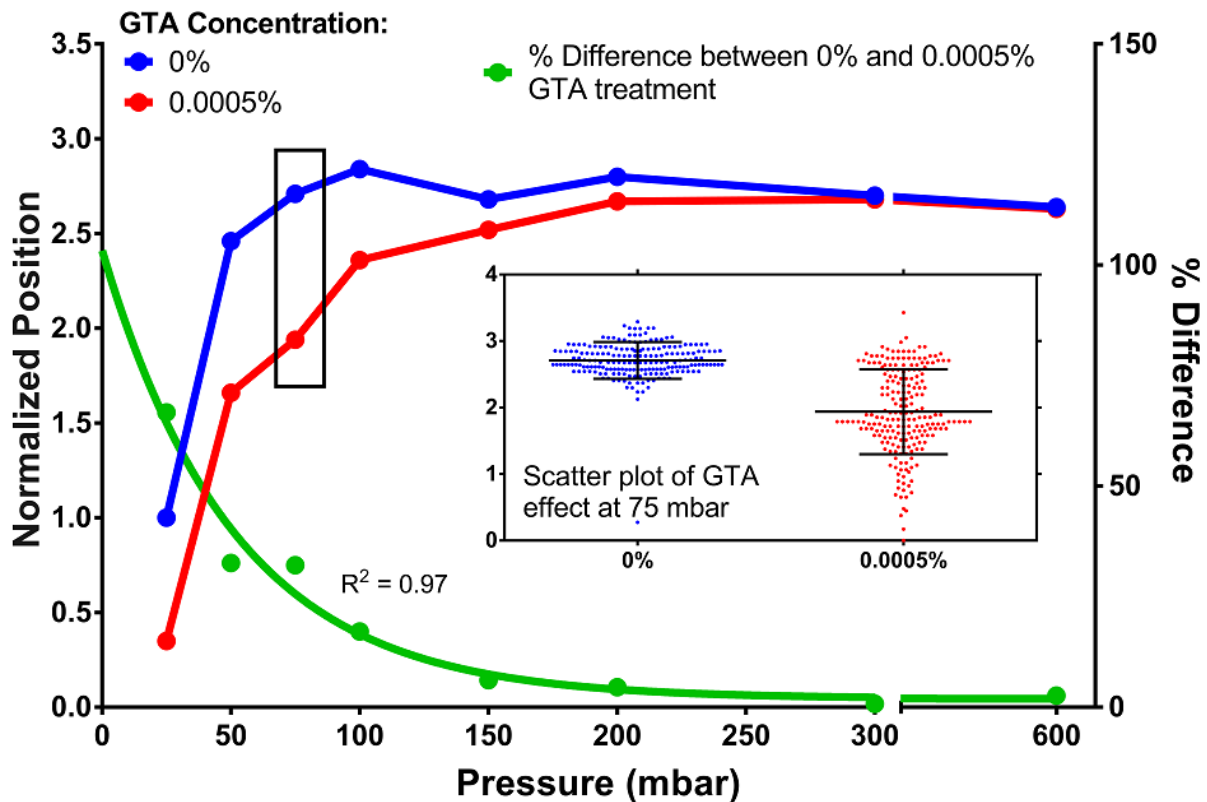


Figure 4-5: The applied pressure waveform is optimized by measuring the % difference between the mean-value of 0% and 0.0005% GTA-treated samples to maximize the sensitivity of the trans-dispersion mechanism ( $n \geq 102$ ).

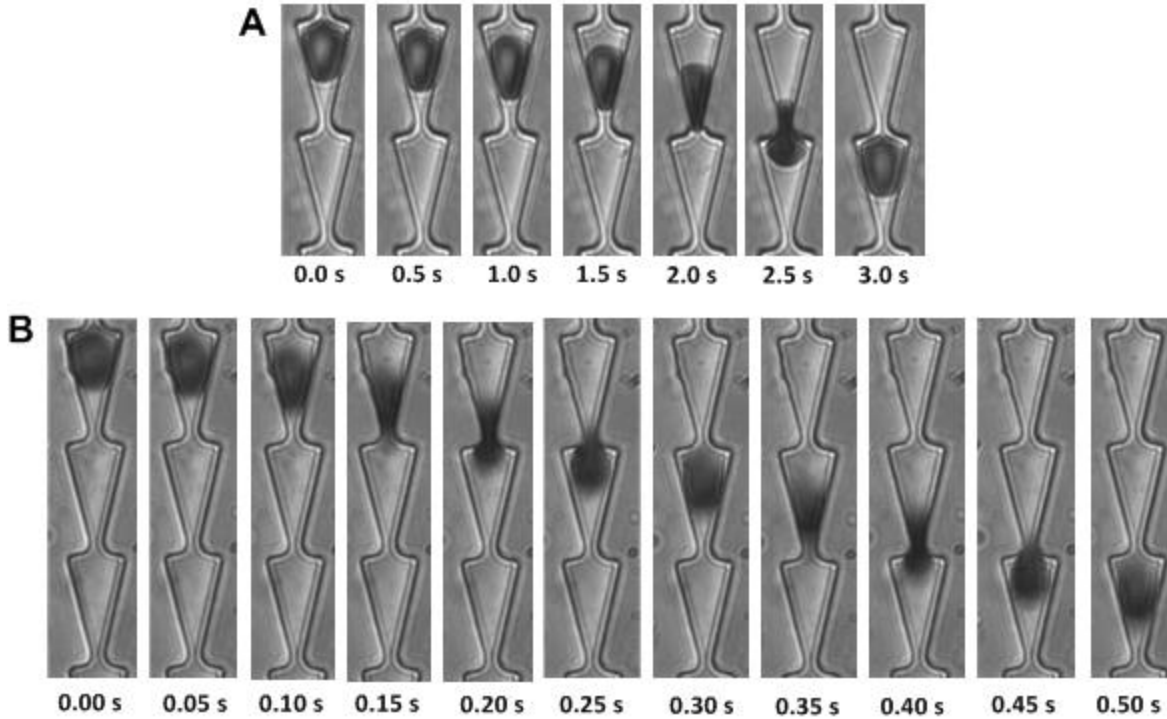


Figure 4-6: Shape of an RBC during deformation process: (A) at 75 mbar, the RBC goes back to its normal discoid shape after each deformation; (B) at 600 mbar, the RBC remains in its deformed, “bullet” shape, resulting in a loss of device capability to resolve the difference in RBC deformability.

Hence, an applied pressure waveform of 150 and 75 mbar was selected. These two pressures could resolve RBC deformability between 0% and 0.0005% GTA-treated samples by 6 and 32% respectively. Since the limit of detection of other microfluidic device is 0.0005% GTA or higher, this concentration was chosen for this experiment to ensure that the applied pressure selected would detect as small a change in RBC deformability as possible in future experiments. The reason to apply a relatively high pressure (150 mbar), despite its low resolution, is to reduce experimental time.

These pressure values were then extrapolated using the hydrodynamic resistance of the deformation microchannels and the pressure attenuator ratio. This extrapolation could be achieved since the position of the cells in the deformation microchannels correlate linearly with the hydrodynamic resistance of the deformation microchannels (Figure 4-7A), which in turn is determined by its thickness (Figure 4-7B) and pore size (Figure 4-7C).

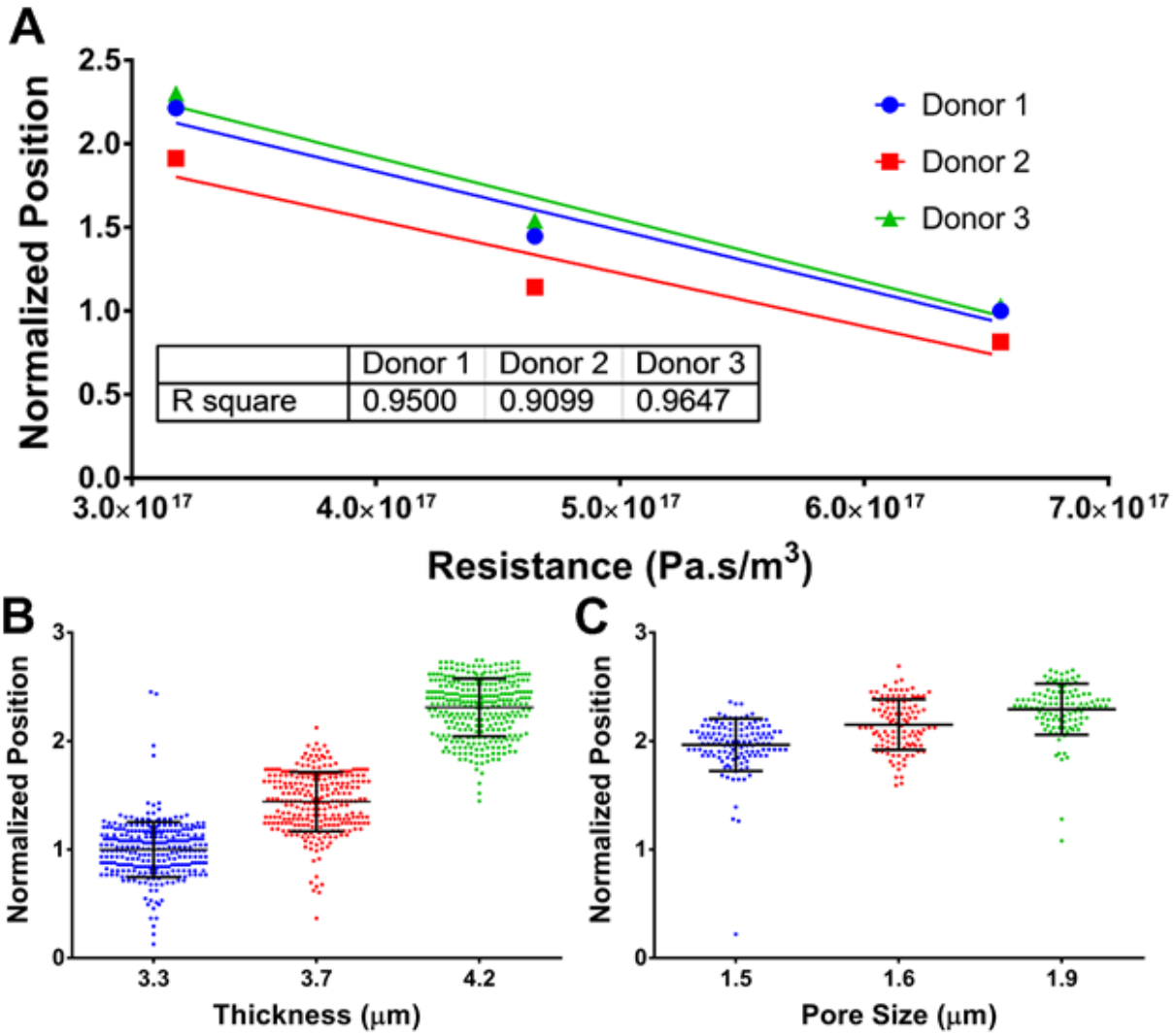


Figure 4-7: The optimized pressure waveform can be linearly extrapolated with the hydrodynamic resistance of the deformation microchannel since the normalized position of the cells linearly correlates with the resistance as shown in (A), when the applied pressure waveform is the same. The thickness of the deformation microchannel (B) is the dominant factor for its hydrodynamic resistance. However, the average pore size also changes the hydrodynamic resistance (C).

#### 4.5 Multiplexing error

To experimentally validate the ability of the trans-dispersion mechanism to remove the aforementioned multiplexing error in section 2.3.1 and 2.3.2, we measured the final positions of fresh RBCs for nearly empty (defined as  $\leq 10\%$  funnels occupied) and nearly full (defined as  $\geq 70\%$  funnels occupied) deformation microchannels. The distributions of the threshold pressures from these two cases are statistically identical ( $p=0.57$ ), which confirms the elimination of the multiplexing error.

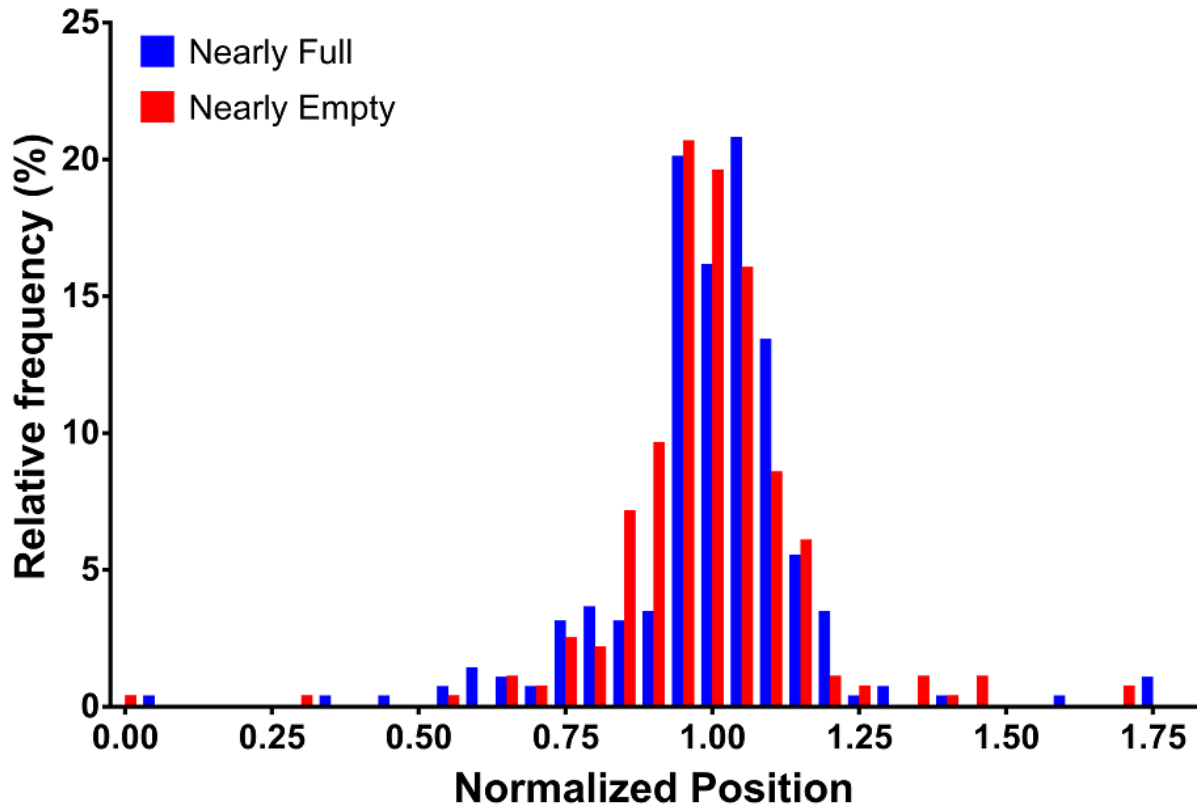


Figure 4-8: Distribution of the measured position with the deformation microchannel array nearly empty (<10% occupancy, n = 281) and nearly full (>70% occupancy, n = 583), which shows no distinction ( $p=0.57$ ). This triplicate sample was normalized based on the donor.

This validation was performed in triplicate on a trans-dispersion prototype with the highest theoretical multiplexing error of 4.9% (prototypes intended for drug-treated parasitized RBCs). Since the multiplexing error of the other prototypes used in this thesis is less than 4.5%, no further tests were carried out.

#### 4.6 Sensitivity

After determining the optimum pressure waveform to be applied for each prototype, the sensitivity of different prototypes of the trans-dispersion device was validated using the same glutaraldehyde (GTA) treatment of 0.0005% to 0.002%, as previously explained. The RBC deformability results obtained (Figure 4-9) can reliably differentiate between control and 0.0005% GTA-treated RBCs ( $p<0.0001$ ,  $n\geq 509$ ), similar to or better than the sensitivities of ektacytometry and other microfluidic methods [21,29,42].

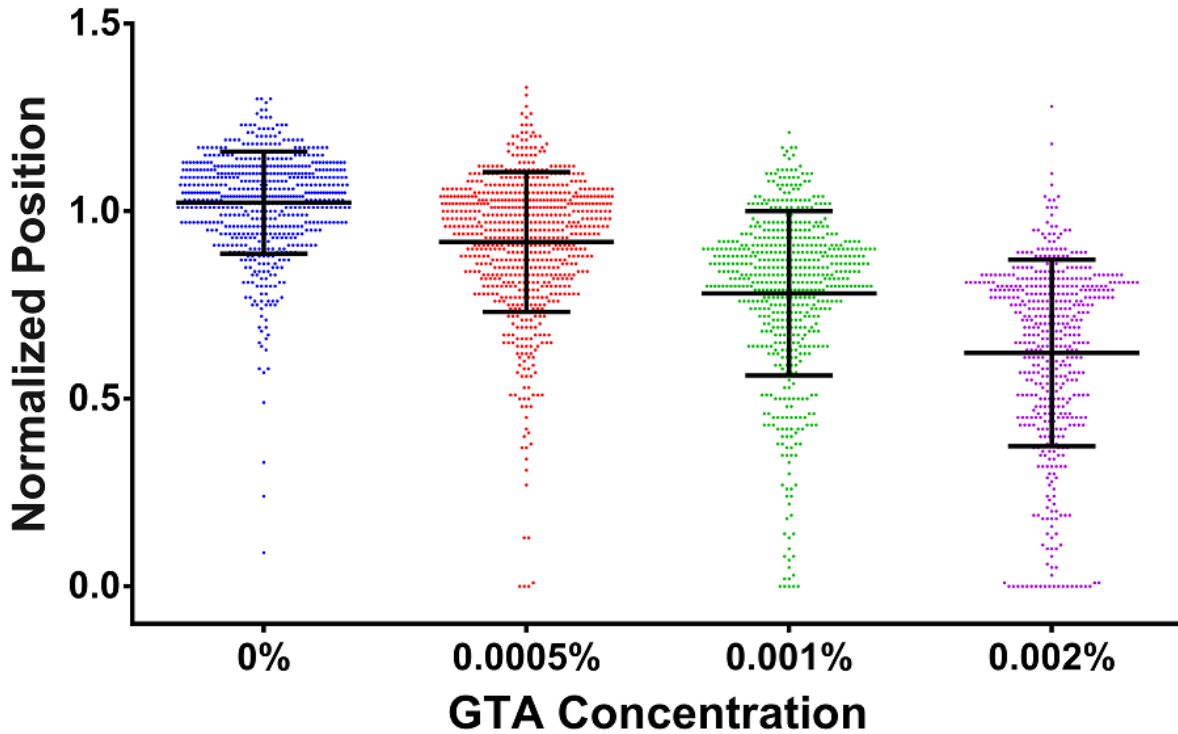


Figure 4-9: The sensitivity of all the trans-dispersion prototypes was evaluated with glutaraldehyde fixation using their individual optimized pressure waveform. Measured values are normalized to the mean of the control with  $n \geq 509$  at each test condition ( $p < 0.0001$ ).

#### 4.7 Throughput

A key advantage of the trans-dispersion mechanism is the ability and ease to parallelize the individual arrays of deformation microchannels, which dramatically increases the throughput of the device. For statistical significance, an equivalent of at least 15 target cells must be measured. Hence, to detect the small subpopulation of parasitized RBCs, the required sample size is defined by Equation 4-1. For example, at least 150 RBCs must be measured for an infected sample having a parasitemia of 10%.

$$n \geq \frac{15}{\text{parasitemia}} \quad \text{Equation 4-1}$$

With the manifold design incorporated into the trans-dispersion mechanism, this system can measure thousands of cells per experiment. More specifically, the 4-fold pressure manifold has a throughput of up to ~100 cells per minute while the 8-fold pressure manifold has a throughput of up to ~200 cells per minute.

## Chapter 5: Biological Applications

Chapter 5 evaluates the potential biological applications of the trans-dispersion mechanism. Section 5.1 presents the deformability profiles of *P. falciparum* infected red blood cells (iRBCs) at various parasitemia levels, including unsynchronized samples (5.1.1) and ring-stage synchronized samples (section 5.1.2). Section 5.2 presents the deformability profiles of iRBCs treated with various antimalarial drugs. Section 5.3 discusses the potential capability of using RBC deformability as a biomarker to detect malarial infection or to screen for alternative antimalarial drugs.

### 5.1 *P. falciparum*-infected RBCs

As explained previously in section 3.3.3, *P. falciparum* iRBCs can be synchronized and harvested to the desired stage in parasitemia growth. To evaluate the potential of the trans-dispersion mechanism in detecting sub-population of iRBCs, unsynchronized samples containing both early and late-stage *P. falciparum* iRBCs were analyzed at various parasitemia levels (section 5.1.1). Afterwards, RBCs infected with synchronized, early-stage parasites (ring-stage) were analyzed (section 5.1.2) at various parasitemia levels. Synchronized samples contained parasitized RBCs, of which greater than 80% of the parasites were of the desired parasite blood stage.

#### 5.1.1 Unsynchronized samples

To investigate the potential to use the trans-dispersion mechanism to detect malaria infection, the deformability of unsynchronized iRBC samples were tested from 0.2% to 5% parasitemia levels (Figure 5-1). The deformability profile of iRBCs become more similar to the control sample (with overlapping standard deviation) as the parasitemia level decreases, which is expected since the iRBCs subpopulation only consists of at most 5% of the whole population. Even then, the mean of the sample decreases with parasitemia level, with a significant 11% decrease in the 5% parasitemia sample as compared to the mean of the control ( $p < 0.0001$ ). An  $n \geq 500$  RBCs (3% parasitemia) for infected samples and  $n = 8575$  RBCs for uninfected sample were measured.

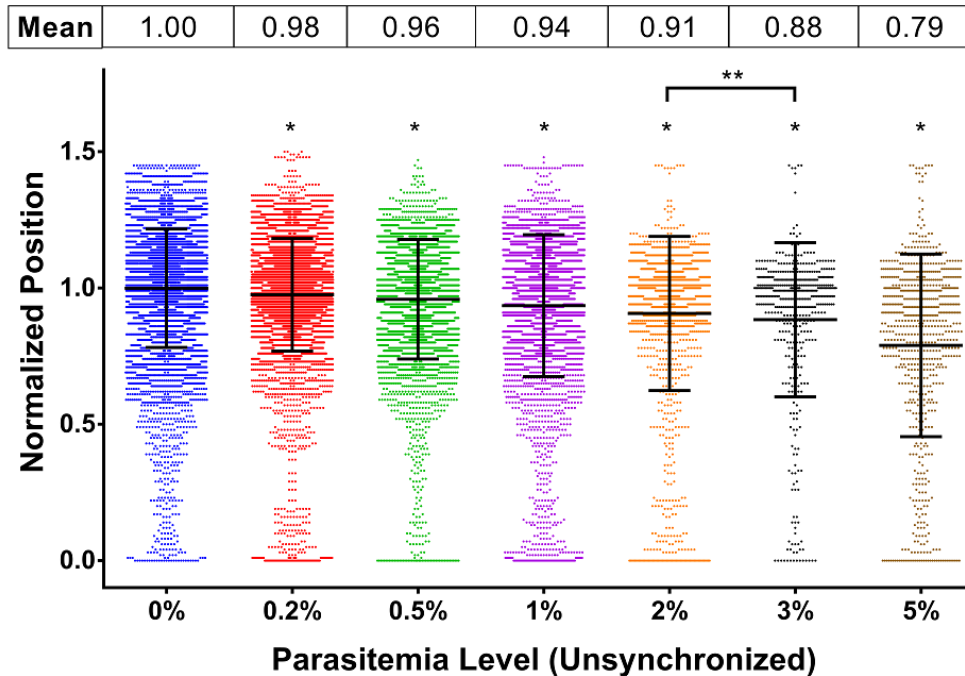


Figure 5-1: The deformability patterns of RBCs parasitized with unsynchronized *P. falciparum*. Each sample is normalized to the mean of the control. The normalized mean of the sample decreases with increasing parasitemia level, with  $p < 0.0001$  for (\*) with respect to control ( $n=8575$  for control and an  $n \geq 500$  for 3% parasitemia level). (\*\*) was not significant. The mean and standard deviation was shown for each sample.

The small subpopulation of malarial-iRBCs becomes progressively stiffer as the parasites mature and hence, to elucidate the effect of this key subpopulation on the deformability measurement, the least deformable subpopulations needed to be analyzed. These iRBCs release proteins that cause bystander injury to the nearby uninfected, exposed RBCs, and decrease the deformability of these uRBCs [3]. Thus, to eliminate the bystander injury effect and to emphasize the effect of the iRBC subpopulation, each sample was normalized to the mean of itself and then sorted according to its deformability measurement (normalized position). The mean of 1% to 100% of the least deformable population fraction was then plotted to obtain the deformability curves shown in Figure 5-2A. The zoomed-in version of the deformability curves shows that measurement sensitivity increases as the least deformable population fraction decreases. The deformability patterns of the 2% least deformable fraction shows that the trans-dispersion mechanism can differentiate between 0% and 0.2% parasitemia levels reliably, which is within the clinically relevant range [71] ( $p < 0.0001$ , Figure 5-2B). The 2% fraction was subsequently chosen as it marks the onset of severe malaria in a clinical setting [71].

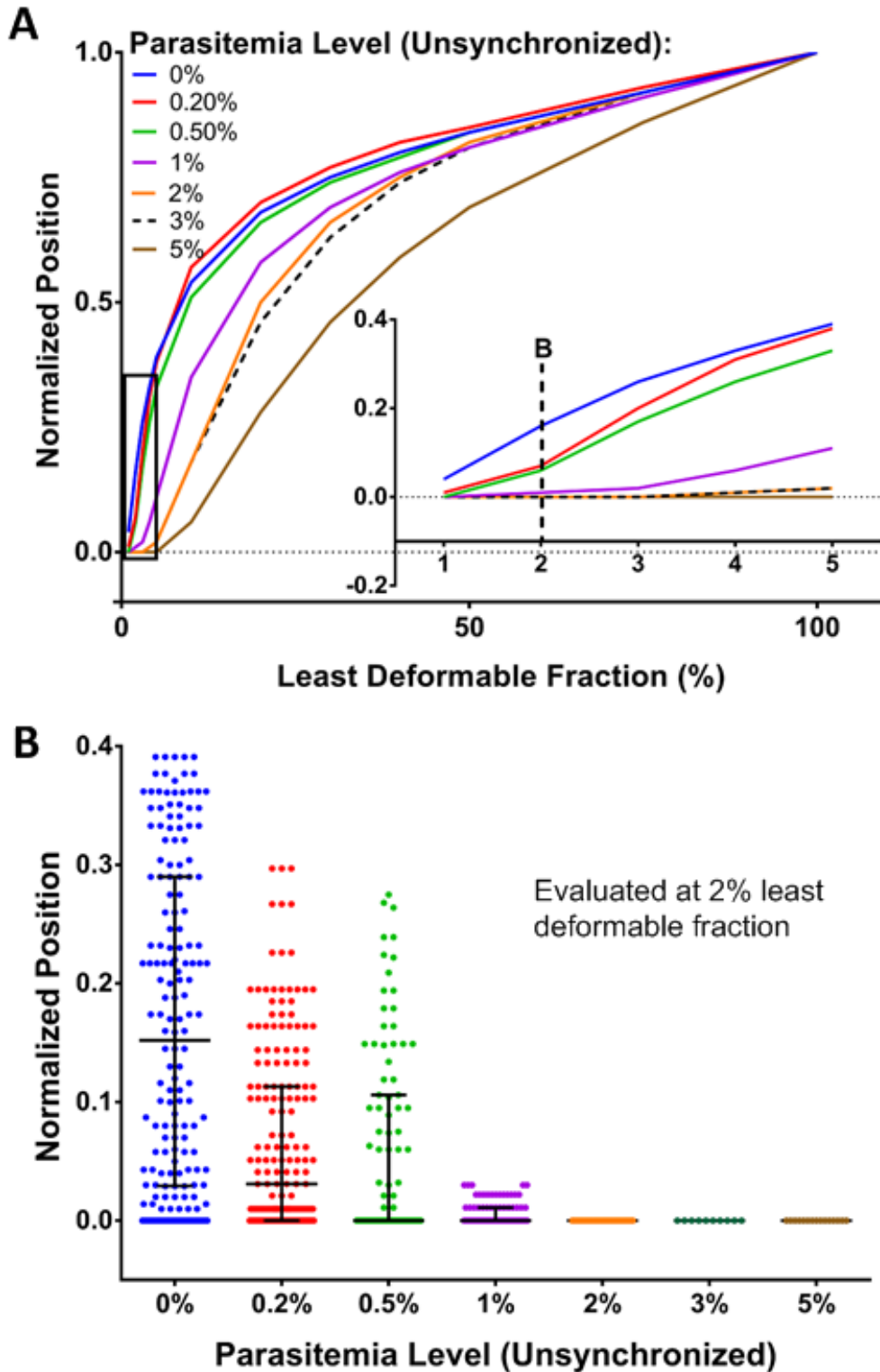


Figure 5-2: (A) The deformability profiles of RBCs parasitized with unsynchronized *P. falciparum* at increasing population fraction from least to most deformable. (B) Detailed deformability profile of (A) at 2% least deformable fraction shows significant difference between 0% and 0.2% parasitemia samples ( $p < 0.0001$ ).

### 5.1.2 Ring-stage synchronized sample

Diagnostically, ring-stage iRBCs are the most interesting stage in the malarial infection life cycle and thus, to successfully detect early malaria infection, we tested ring-synchronized iRBC samples ranging from 1% to 10% parasitemia levels (Figure 5-3), normalized to mean of the control. Similar to the unsynchronized samples, the mean of each sample decreases with increasing parasitemia, with a 9% decrease in mean deformability for 10% parasitemia samples compared to uninfected samples ( $p < 0.0001$ ). An  $n \geq 978$  (2% parasitemia) for infected samples and  $n = 9074$  for uninfected samples were measured.

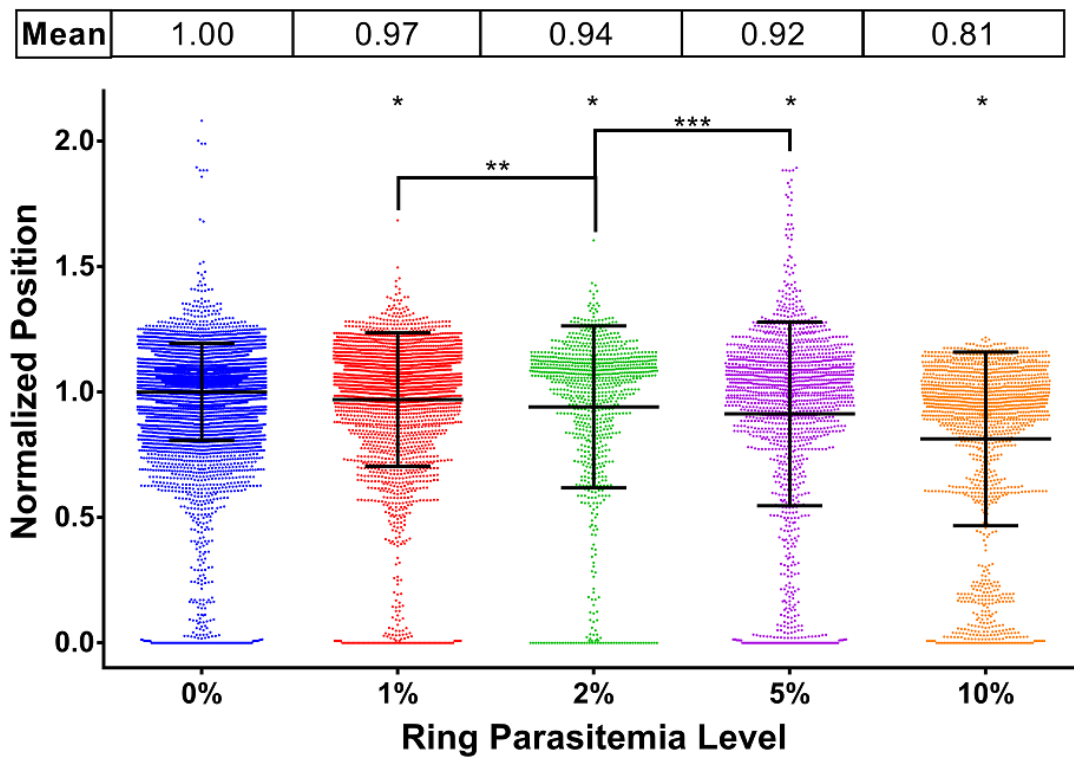


Figure 5-3: Deformability patterns of RBCs parasitized with synchronized *P. falciparum* at ring-stage show decreased mean normalized position occurring with increasing parasitemia level with  $p < 0.0001$  for (\*) ( $n = 9074$  for control and an  $n \geq 978$  for 2% parasitemia level). (\*\*) and (\*\*\*) is significant with  $p = 0.0053$  and  $p = 0.0479$  respectively.

Following the same analysis method as the unsynchronized sample, the cumulative distribution curves of parasitized RBCs from the least deformable to the most deformable population fraction show distinct separation from the controls (Figure 5-4). At the 2% least deformable population fraction, the scatter-plot shows that the trans-dispersion mechanism can significantly distinguish between 0% and 1% parasitemia levels ( $p < 0.0001$ , Figure 5-4).

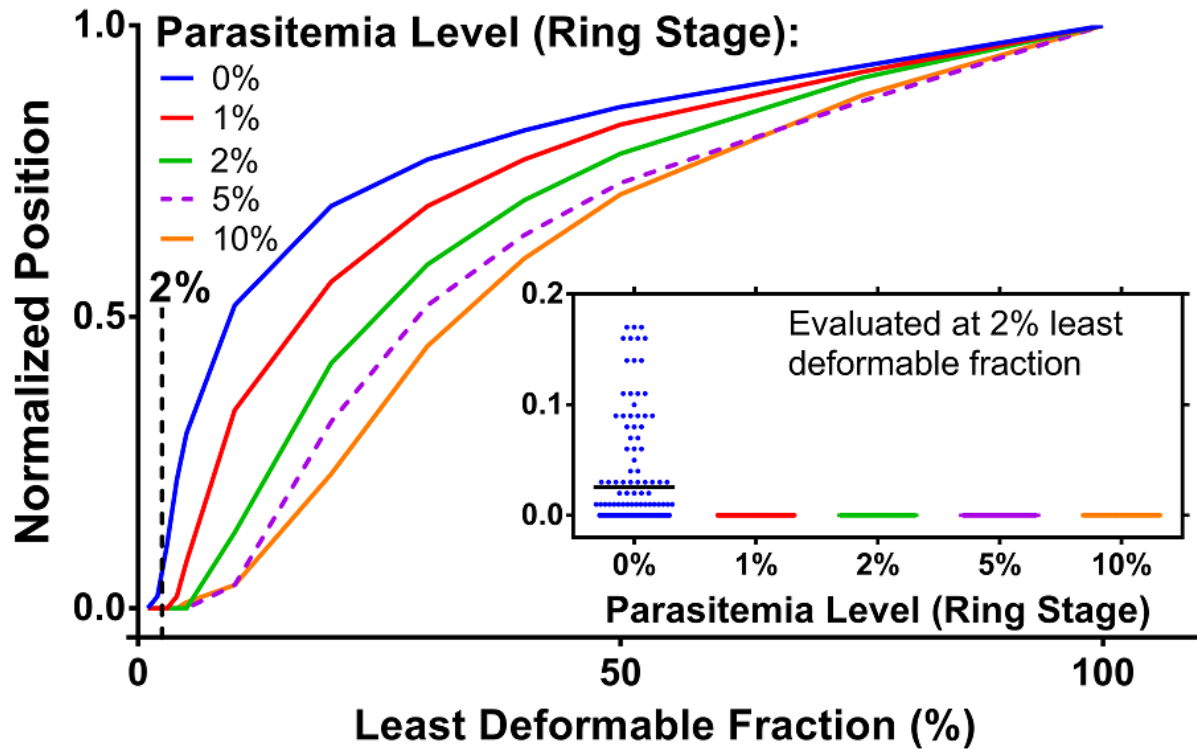


Figure 5-4: The deformability profiles of RBCs parasitized with ring-synchronized *P. falciparum* at increasing population fraction from least to most deformable. The detailed deformability profile evaluated at 2% least deformable population (insert) shows a significance difference between 0% and 1% parasitemia samples ( $p < 0.0001$ ).

### 5.1.3 Non-transiting cells

The trans-dispersion mechanism was designed to capture rigid iRBCs by not allowing these cells to transit beyond the first funnel (funnel 0). The percentage of these non-transiting cells shows a strong direct correlation with the parasitemia level, with  $r^2$  value of 0.92 and 0.95, (Figure 5-5) for both the unsynchronized and synchronized ring-stage samples. The device used to measure the unsynchronized sample has a bigger average pore size than the one used to measure the ring-stage, which explains why unsynchronized samples have a lower percentage of non-transiting cells and smaller  $r^2$  value since it is unable to capture the less deformable ring-stage iRBCs.

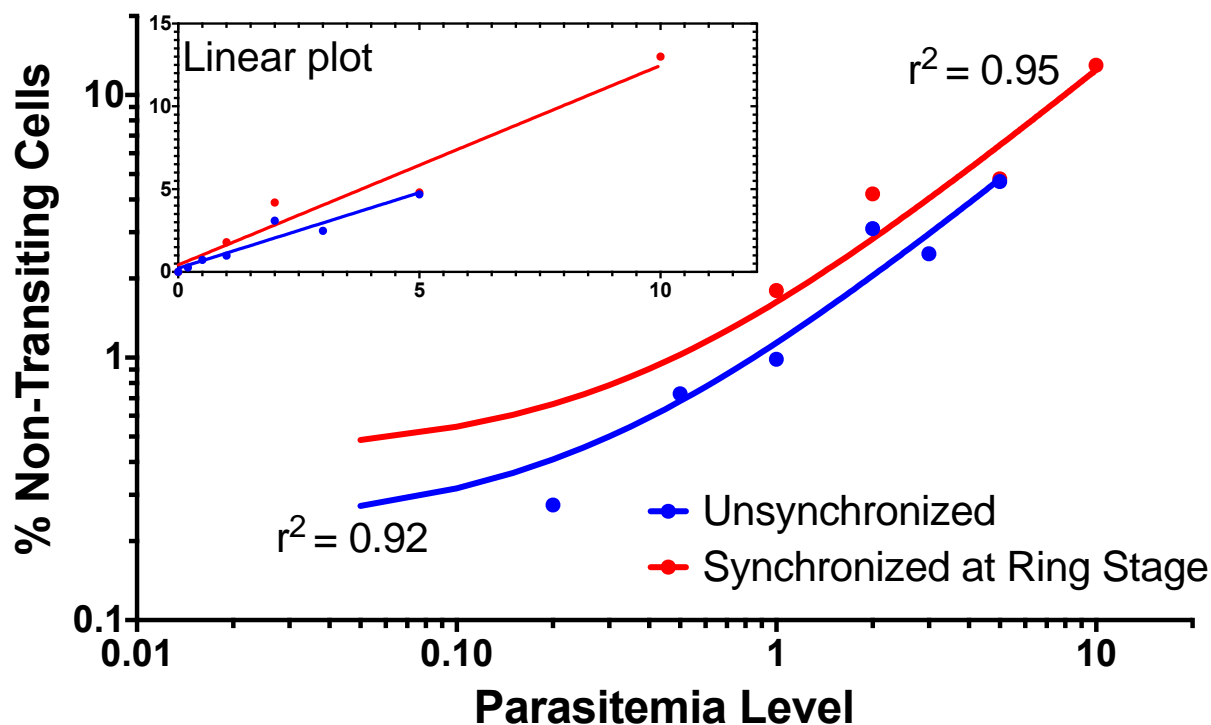


Figure 5-5: A strong, positive correlation between parasitemia level and percentage of non-transiting cells is plotted at log-log scale ( $r^2 \geq 0.92$ ) and (insert) at linear scale.

## 5.2 Antimalarial drug response

This work investigated the effect of 11 clinical antimalarial compounds, including chloroquine and artesunate, on purified trophozoite-iRBCs with drug concentrations  $\geq$  EC50. Eight samples, that include a control and 7 drug-treated iRBCs, were assessed simultaneously to validate the system's capability in multiplexing individual trans-dispersion arrays. Nearly all clinical antimalarial compounds tested, with the exception of tetracycline ( $p = 0.54$ ) and dihydroisoquinolone (DHIQ) SJ733 enantiomer ( $p=0.1$ ), reduced the deformability of *P. falciparum* infected RBCs compared to the control (Figure 5-6,  $p < 0.0001$ ) by at least 18%, as shown in Table 5-1.

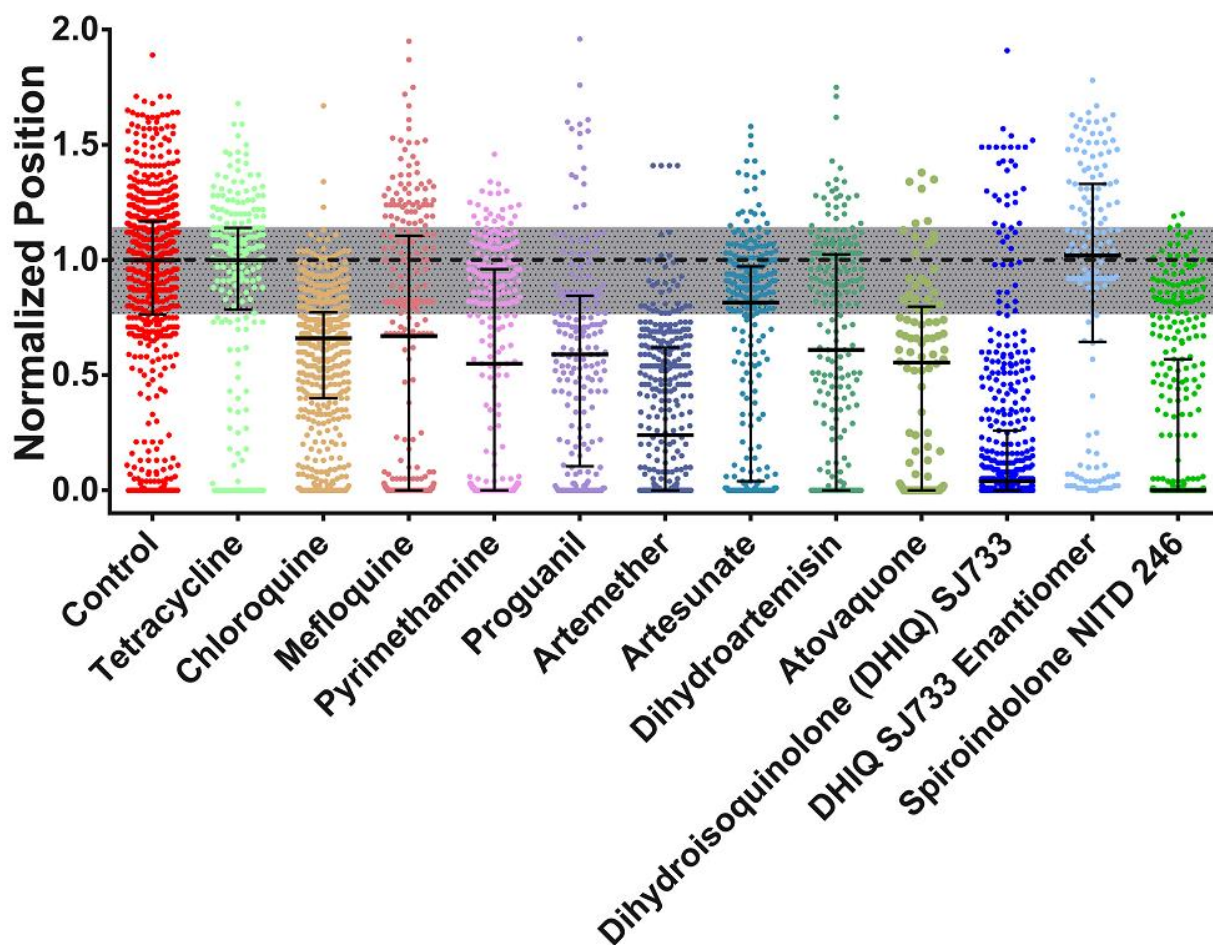


Figure 5-6: Evaluating antimalarial drug efficacy. Antimalarial drug response ( $> 4 \times \text{EC}_{50}$ ) in late-stage RBC infected with *P. falciparum* parasites show decreased deformability for all antimalarial drugs ( $p < 0.0001$ ) except tetracycline ( $p = 0.54$ ) and DHIQ enantiomer, which is DHIQ negative control ( $p = 0.1$ ) with  $n \geq 100$  (for atovaquone) for all samples.

All drug-treated samples were normalized to the median of the control. The control for this experiment was purified late-stage iRBCs treated with 0.01% DMSO. The p-value of each sample was evaluated using a Mann-Whitney t-test and showed significant difference for all samples, except for tetracycline and DHIQ negative control. The percentage change between the control and the drug-treated samples were also calculated, with artesunate giving the least effect of 18% change (Table 5-1). A minimum of  $n = 100$  (atovaquone) for infected samples and  $n = 616$  for control samples were measured.

Table 5-1: Individual concentrations and normalized deformability values for various antimalarial drug treatments (n = 616 for control and n≥100 for iRBCs).

Drug Name	Concentration (≥ 4 × EC50)	Number of RBCs	Median	% decrease vs. DMSO	p-value
Tetracyclines	100 μM	245	1.00	0	0.54
Chloroquine	1 μM	502	0.66	34	<0.0001
Mefloquine	1 μM	281	0.67	33	<0.0001
Pyrimethamine	20 nM	267	0.55	45	<0.0001
Proguanil	100 μM	205	0.59	41	<0.0001
Arthemether	8 nM	364	0.24	76	<0.0001
Artesunate	10 nM	270	0.82	18	<0.0001
Dihydroartemisinin	20 nM	233	0.61	39	<0.0001
Atovaquone	250 nM	100	0.56	44	<0.0001
Dihydroisoquinolone SJ733	1.08 μM	307	0.01	100	<0.0001
Dihydroisoquinolone SJ733 Enantiomer	1.08 μM	153	1.02	-2%	0.1
Spiroindolone NITD 246	3.6 nM	369	0.00	100	<0.0001

### 5.3 Discussion

One of the key advantages of the trans-dispersion mechanism is the ability to apply equal pressure difference in each deformation microchannel to transit each cell. The equal pressure difference is due to its self-compensating fluid network, described in section 2.3.3. The strong positive correlation ( $r^2 = 0.92$ ) between the proportion of non-transiting cells and the parasitemia level highlights the advantage of the self-compensating fluid network, which cannot be achieved in a simple filtration technique [32]. Hence, the trans-dispersion system can be potentially used to detect malaria infection biophysically, without the need for labels or reagents.

This work has demonstrated that, with the exception of tetracycline and DHIQ SJ733 enantiomer, 10 clinical antimalarial drugs, which act through different mechanisms, reduced the deformability of purified trophozoite-iRBCs. Tetracycline is a slow-acting compound that

requires more than 48h of incubation, which may explain why there was no decrease in deformability for iRBCs treated with tetracycline [63]. DHIQ SJ733 enantiomer is the negative control for DHIQ SJ733 drug, which explains why the deformability of iRBCs remains unchanged [64]. Previous studies showed that chloroquine and mefloquine destroys the integrity of parasite by enhancing the association of toxic heme to the RBC membrane [72]. In turn, heme is converted to hematin, which induces oxidative damage to RBC membrane and results in decreased RBC deformability [73]. Our system measured a 34% and a 33% reduction in deformability for chloroquine and mefloquine, respectively. We also tested the three major artemisinin derivatives (artesunate, artemether and dihydroartemisinin) that have been shown to reduce RBC deformability by stimulating reactive oxygen species (ROS) activation [74]. Amongst these tested artemisinin derivatives, artemether resulted in the least deformable iRBCs, where the deformability was reduced by 76%. The reduced deformability for drug-treated iRBCs is in agreement with other studies that showed rigidification of iRBCs after exposure to antimalarial drugs, such as chloroquine and artesunate [15,75]. The least deformable iRBCs resulted from the treatment with the novel antimalarial spiroindolone family, DHIQ SJ733 and NITD-246, showing a 100% reduction in deformability. The spiroindolone family increases the intracellular pH of the parasites [76] and in turn, affects the elastic properties of the RBC membrane, leading to significant decrease in iRBC deformability [77].

This work shows that most antimalarials result in loss of deformability of iRBCs, which may enhance parasite clearance by the spleen. In mice infected with *P. yoelii*, it was shown that chloroquine treatment correlated to increased circulatory clearance of iRBCs [75]. In addition, KAE609, another spiroindolone candidate, cleared parasites notably faster compared to artesunate in a phase II study in a total of 21 patients infected with *P. falciparum* and *P. vivax* in Thailand [78]. Collectively, our results suggest that RBC deformability can be used as a biomarker for antimalarial drug efficacy and thus, the trans-dispersion mechanism can potentially be used for screening novel antimalarial drugs.

The World Health Organization (WHO) defines malaria cases as severe when there is clinical or laboratory evidence of vital organ dysfunction. However, the WHO recommends a low threshold for starting parenteral treatment in patients even if laboratory results are not available [79]. Intravenous quinine and quinidine were the most widely used drugs in the

treatment of severe falciparum malaria [26] but in 2012, the WHO released a handbook that recommends artemisinin derivatives, especially intravenous artesunate, as the main treatment for severe malaria [79]. Even though intravenous artesunate was shown to reduce the mortality rate by 35% as compared to intravenous quinine, the mortality rate of 15% after intravenous artesunate treatment remains relatively high [80]. We have shown that antimalarials belonging to the spiroindolone family show a more significant decrease in deformability compared to the artemisinin family, which may suggest that other antimalarial drugs may be more effective in treating severe malaria. Furthermore, with the increasing widespread use of intravenous artesunate, recent studies show that *P. falciparum* resistance to artemisinin is prevalent across mainland Southeast Asia [81]. The effectiveness of artemisinin derivatives may also differ for each region, for example, in a study of Vietnamese adults [82], it was suggested that intramuscular artesunate was superior to intramuscular artemether, while another study in Papua New Guinea [83] showed that artemether-lumefantrine and dihydroartemisinin (DHA)-piperazine combination therapy was more effective than artesunate combination therapy. Therefore, our trans-dispersion mechanism can be potentially used for screening for a more effective drug-combination therapy in different regions or in cases where drug resistance is suspected.

## Chapter 6: Summary and Conclusions

### 6.1 Summary of thesis

This work has demonstrated a sensitive and label-free tool for high-throughput and highly parallel measurements of RBC deformability. Individual RBCs are flowed through a series of constrictions in a microfluidic channel where their transit speed is a function of their deformability. This process is analogous to DNA gel-electrophoresis, where the migration speed of DNA molecules depends on their size. The final position of each cell is determined using simple bright-field microscopy and automated image processing to produce a readout that is similar to the intensity bands in a DNA gel.

To ensure a sensitive and consistent measurement, the geometry of the constriction is sized such that the transiting cell forms a temporary seal with each constriction while supporting microchannels ensure consistent forces are applied to each deformation channel. The effect of constriction geometries is minimized due to repeated deformations of RBCs, enabling a more reliable and consistent measurement of RBC deformability. The multiplexed design of microchannels in parallel also ensures that a clogged microchannel does not significantly influence the pressure in other microchannels, unlike other filtration-based techniques. More importantly, the ability of trans-dispersion mechanism to multiplex individual and independent arrays enables a high-throughput and highly parallelized analysis of RBC deformability, in which multiple samples can be assessed simultaneously. While other deformability techniques might offer higher throughput, to the extent of our knowledge, none have shown the ability to measure simultaneous measurements of different samples. Based on this simple and efficient design, this microfluidic analysis can be performed without the need for specialized reagents, laboratory equipment or technical expertise.

Based on the treatment of glutaraldehyde-treated RBCs, the sensitivity of trans-dispersion mechanism is shown to be comparable or better than conventional techniques or other microfluidic techniques in measuring RBC deformability. This microfluidic system was also able to mechanically detect malarial infection by successfully identifying a small number of *P. falciparum* infected RBCs in a heterogeneous sample. Furthermore, this system was able to

simultaneously assess the efficacy of several antimalarial compounds for their ability to reduce iRBC deformability. The results show that rigidification of iRBCs can potentially be used to evaluate antimalarial drug efficacy as well as “new drug” screening.

## **6.2 Future work**

The trans-dispersion device is currently being used for other applications. An example is the study to monitor the changes in RBC deformability associated with cold storage of blood bags in transfusion medicine. In addition, this device is also used to characterize the RBC deformability associated with sickle cell disease. We are also collaborating with GlaxoSmithKline (Spain) to test ~20 additional antimalarial drugs in a blind study.

## References:

- [1] Chen LT, Weiss L. The role of the sinus wall in the passage of erythrocytes through the spleen. *Blood* 1973;41:529–37.
- [2] Weiss L, Tavassoli M. Anatomical hazards to the passage of erythrocytes through the spleen. *Semin Hematol* 1970;7:372–80.
- [3] Dondorp AM, Kager PA, Vreeken J, White NJ. Abnormal blood flow and red blood cell deformability in severe malaria. *Parasitol Today* 2000;16:228–32. doi:10.1016/S0169-4758(00)01666-5.
- [4] Suresh S, Spatz J, Mills JP, Micoulet A, Dao M, Lim CT, et al. Connections between single-cell biomechanics and human disease states: gastrointestinal cancer and malaria. *Acta Biomater* 2005;1:15–30. doi:10.1016/j.actbio.2004.09.001.
- [5] Elson EL. Cellular Mechanics as an Indicator of Cytoskeletal Structure and Function. *Annu Rev Biophys Biophys Chem* 1988;17:397–430. doi:10.1146/annurev.bb.17.060188.002145.
- [6] Kwan JM, Guo Q, Kyliuk-Price DL, Ma H, Scott MD. Microfluidic analysis of cellular deformability of normal and oxidatively damaged red blood cells. *Am J Hematol* 2013;88:682–9. doi:10.1002/ajh.23476.
- [7] Lee GYH, Lim CT. Biomechanics approaches to studying human diseases. *Trends Biotechnol* 2007;25:111–8. doi:10.1016/j.tibtech.2007.01.005.
- [8] Nash GB, O'Brien E, Gordon-Smith EC, Dormandy J a. Abnormalities in the mechanical properties of red blood cells caused by *Plasmodium falciparum*. *Blood* 1989;74:855–61.
- [9] Herricks T, Antia M, Rathod PK. Deformability limits of *Plasmodium falciparum*-infected red blood cells. *Cell Microbiol* 2009;11:1340–53. doi:10.1111/j.1462-5822.2009.01334.x.
- [10] Scott MD, Rouyer-Fessard P, Ba MS, Lubin BH, Beuzard Y.  $\alpha$ - and  $\beta$ -haemoglobin chain induced changes in normal erythrocyte deformability: comparison to  $\beta$  thalassaemia intermedia and Hb H disease. *Br J Haematol* 1992;80:519–26.
- [11] Barabino G a, Platt MO, Kaul DK. Sickle cell biomechanics. *Annu Rev Biomed Eng* 2010;12:345–67. doi:10.1146/annurev-bioeng-070909-105339.
- [12] Vayá A, Simó M, Santaolaria M, Todolí J, Aznar J. Red blood cell deformability in iron deficiency anaemia. *Clin Hemorheol Microcirc* 2005;33:75–80.
- [13] Yip R, Mohandas N, Clark MR, Jain S, Shohet SB, Dallman PR. Red cell membrane stiffness in iron deficiency. *Blood* 1983;62:99–106.

- [14] Reinhart WH. The influence of iron deficiency on erythrocyte deformability. *Br J Haematol* 1992;80:550–5.
- [15] Huang S, Undisz A, Diez-Silva M, Bow H, Dao M, Han J. Dynamic deformability of *Plasmodium falciparum*-infected erythrocytes exposed to artesunate in vitro. *Integr Biol (Camb)* 2013;5:414–22. doi:10.1039/c2ib20161e.
- [16] Snow RW, Guerra CA, Noor AM, Myint HY, Hay SI. The global distribution of clinical episodes of *Plasmodium falciparum* malaria. *Nature* 2005;434:214–7. doi:10.1038/nature03342.
- [17] Kantele A, Jokiranta TS. Review of cases with the emerging fifth human malaria parasite, *Plasmodium knowlesi*. *Clin Infect Dis* 2011;52:1356–62. doi:10.1093/cid/cir180.
- [18] Maier AG, Cooke BM, Cowman AF, Tilley L. Malaria parasite proteins that remodel the host erythrocyte. *Nat Rev Microbiol* 2009;7:341–54. doi:10.1038/nrmicro2110.
- [19] Safeukui I, Correas J-M, Brousse V, Hirt D, Deplaine G, Mule S, et al. Retention of *Plasmodium falciparum* ring-infected erythrocytes in the slow, open microcirculation of the human spleen. *Blood* 2008;112:2520–8. doi:10.1182/blood-2008-03-146779.
- [20] Cranston HA, Boylan CW, Carroll GL, Sutura SP, Williamson JR, Gluzman IY, et al. *Plasmodium falciparum* maturation abolishes physiologic red cell deformability. *Science* 1984;223:400–3. doi:10.1126/science.6362007.
- [21] Guo Q, Reiling SJ, Rohrbach P, Ma H. Microfluidic biomechanical assay for red blood cells parasitized by *Plasmodium falciparum*. *Lab Chip* 2012;12:1143–50. doi:10.1039/c2lc20857a.
- [22] Stockert JC, Blázquez-Castro A, Horobin RW. Identifying different types of chromatin using giemsa staining. *Methods Mol Biol* 2014;1094:25–38. doi:10.1007/978-1-62703-706-8\_3.
- [23] Häscheid T. Diagnosis of malaria: A review of alternatives to conventional microscopy. *Clin Lab Haematol* 1999;21:235–45. doi:10.1046/j.1365-2257.1999.00220.x.
- [24] Iqbal J, Sher a., Rab a. *Plasmodium falciparum* histidine-rich protein 2-based immunocapture diagnostic assay for malaria: Cross-reactivity with rheumatoid factors. *J Clin Microbiol* 2000;38:1184–6.
- [25] Bell DR, Wilson DW, Martin LB. False-positive results of a *Plasmodium falciparum* histidine-rich protein 2-detecting malaria rapid diagnostic test due to high sensitivity in a community with fluctuating low parasite density. *Am J Trop Med Hyg* 2005;73:199–203. doi:73/1/199 [pii].

- [26] Trampuz A, Jereb M, Muzlovic I, Prabhu RM. Clinical review: Severe malaria. *Crit Care* 2003;7:315–23. doi:10.1186/cc2183.
- [27] Bessis M, Mohandas N, Feo C. Automated ektacytometry: a new method of measuring red cell deformability and red cell indices. *Blood Cells* 1980;6:315–27.
- [28] Clark MR, Mohandas N, Shohet SB. Osmotic gradient ektacytometry: comprehensive characterization of red cell volume and surface maintenance. *Blood* 1983;61:899–910.
- [29] Baskurt OK, Hardeman MR, Uyklu M, Ulker P, Cengiz M, Nemeth N, et al. Comparison of three commercially available ektacytometers with different shearing geometries. *Biorheology* 2009;46:251–64.
- [30] Streekstra GJ, Dobbe JGG, Hoekstra a G. Quantification of the fraction poorly deformable red blood cells using ektacytometry. *Opt Express* 2010;18:14173–82.
- [31] Berezina TL, Zaets SB, Morgan C, Spillert CR, Kamiyama M, Spolarics Z, et al. Influence of storage on red blood cell rheological properties. *J Surg Res* 2002;102:6–12. doi:10.1006/jsre.2001.6306.
- [32] Reid H, Barnes A, Lock P, Dormandy J, Dormandy T. A simple method for measuring erythrocyte deformability. *Tech Methods* 1973:855–8.
- [33] Hochmuth RM. Micropipette aspiration of living cells. *J Biomech* 2000;33:15–22.
- [34] Hebbel RP, Leung a, Mohandas N. Oxidation-induced changes in microrheologic properties of the red blood cell membrane. *Blood* 1990;76:1015–20.
- [35] Evans E, Mohandas N, Leung a. Static and dynamic rigidities of normal and sickle erythrocytes. Major influence of cell hemoglobin concentration. *J Clin Invest* 1984;73:477–88. doi:10.1172/JCII11234.
- [36] Dulińska I, Targosz M, Strojny W, Lekka M, Czuba P, Balwierz W, et al. Stiffness of normal and pathological erythrocytes studied by means of atomic force microscopy. *J Biochem Biophys Methods* 2006;66:1–11. doi:10.1016/j.jbbm.2005.11.003.
- [37] Lekka M, Fornal M, Pyka-Fościk G, Lebed K, Wizner B, Grodzicki T, et al. Erythrocyte stiffness probed using atomic force microscope. *Biorheology* 2005;42:307–17.
- [38] Mills JP, Qie L, Dao M, Lim CT, Suresh S. Nonlinear elastic and viscoelastic deformation of the human red blood cell with optical tweezers. *Mech Chem Biosyst* 2004;1:169–80.
- [39] Hénon S, Lenormand G, Richert a, Gallet F. A new determination of the shear modulus of the human erythrocyte membrane using optical tweezers. *Biophys J* 1999;76:1145–51. doi:10.1016/S0006-3495(99)77279-6.

- [40] Dao M, Lim CT, Suresh S. Mechanics of the human red blood cell deformed by optical tweezers. *J Mech Phys Solids* 2003;51:2259–80. doi:10.1016/j.jmps.2003.09.019.
- [41] Adamo A, Sharei A, Adamo L, Lee B, Mao S, Jensen KF. Microfluidics-based assessment of cell deformability. *Anal Chem* 2012;84:6438–43. doi:10.1021/ac300264v.
- [42] Bow H, Pivkin I V, Diez-Silva M, Goldfless SJ, Dao M, Niles JC, et al. A microfabricated deformability-based flow cytometer with application to malaria. *Lab Chip* 2011;11:1065–73. doi:10.1039/c0lc00472c.
- [43] Zheng Y, Shojaei-Baghini E, Azad A, Wang C, Sun Y. High-throughput biophysical measurement of human red blood cells. *Lab Chip* 2012;12:2560–7. doi:10.1039/c2lc21210b.
- [44] Guo Q, McFaul SM, Ma H. Deterministic microfluidic ratchet based on the deformation of individual cells. *Phys Rev E* 2011;83:051910. doi:10.1103/PhysRevE.83.051910.
- [45] Guo Q, Duffy SP, Matthews K, Santoso AT, Scott MD, Ma H. Microfluidic analysis of red blood cell deformability. *J Biomech* 2014;47:1767–76. doi:10.1016/j.jbiomech.2014.03.038.
- [46] Myrand-Lapierre M-E, Deng X, Ang RR, Matthews K, Santoso AT, Ma H. Multiplexed fluidic plunger mechanism for the measurement of red blood cell deformability. *Lab Chip* 2015;15:159–67. doi:10.1039/C4LC01100G.
- [47] Stuart J. Review article Erythrocyte rheology 1985:965–77.
- [48] Buchan PC. Evaluation and modification of whole blood filtration in the measurement of erythrocyte deformability in pregnancy and the newborn. *Br J Haematol* 1980;45:97–105.
- [49] Guo Q. Microfluidic Device for Measuring Deformability of Single Cells. *UBC Library Arch* 2012.
- [50] Myrand-Lapierre M-E. Multiplexed Fluidic Plunger Mechanism for the Measurement of Red Blood Cell Deformability. University of British Columbia, 2014.
- [51] Guo Q, Park S, Ma H. Microfluidic micropipette aspiration for measuring the deformability of single cells. *Lab Chip* 2012;12:2687–95. doi:10.1039/c2lc40205j.
- [52] Haines WB. Studies in the physical properties of soil. V. The hysteresis effect in capillary properties, and the modes of moisture distribution associated therewith. *J Agric Sci* 1930;20:97. doi:10.1017/S002185960008864X.
- [53] Zhang XB, Wu ZQ, Wang K, Zhu J, Xu JJ, Xia XH, et al. Gravitational sedimentation induced blood delamination for continuous plasma separation on a microfluidics chip. *Anal Chem* 2012;84:3780–6. doi:10.1021/ac3003616.

- [54] Kenny MW, Meakin M, Worthington DJ, Stuart J. Erythrocyte deformability in sickle-cell crisis. *Br J Haematol* 1981;49:103–9.
- [55] Dobbe JGG, Streekstra GJ, Hardeman MR, Ince C, Grimbergen CA. Measurement of the Distribution of Red Blood Cell Deformability Using an Automated Rheoscope. *Clin Cytom* 2002;50:313–25. doi:10.1002/cyto.10171.
- [56] Glenister FK, Coppel RL, Cowman AF, Mohandas N, Cooke BM. Contribution of parasite proteins to altered mechanical properties of malaria-infected red blood cells. *Blood* 2002;99:1060–3. doi:10.1182/blood.V99.3.1060.
- [57] Desai SP, Freeman DM, Voldman J. Plastic masters-rigid templates for soft lithography. *Lab Chip* 2009;9:1631–7. doi:10.1039/b822081f.
- [58] Luk VN, Mo GC, Wheeler AR. Pluronic additives: A solution to sticky problems in digital microfluidics. *Langmuir* 2008;24:6382–9. doi:10.1021/la7039509.
- [59] Radfar A, Méndez D, Moneriz C, Linares M, Marín-García P, Puyet A, et al. Synchronous culture of *Plasmodium falciparum* at high parasitemia levels. *Nat Protoc* 2009;4:1899–915. doi:10.1038/nprot.2009.198.
- [60] Hackett S, Hamzah J, Davis TME, St Pierre TG. Magnetic susceptibility of iron in malaria-infected red blood cells. *Biochim Biophys Acta* 2009;1792:93–9. doi:10.1016/j.bbadis.2008.11.001.
- [61] Mu J, Myers RA, Jiang H, Liu S, Ricklefs S, Waisberg M, et al. *Plasmodium falciparum* genome-wide scans for positive selection, recombination hot spots and resistance to antimalarial drugs. *Nat Genet* 2010;42:268–71. doi:10.1038/ng.528.
- [62] Vivas L, Rattray L, Stewart LB, Robinson BL, Fugmann B, Haynes RK, et al. Antimalarial efficacy and drug interactions of the novel semi-synthetic endoperoxide artemisone in vitro and in vivo. *J Antimicrob Chemother* 2007;59:658–65. doi:10.1093/jac/dkl563.
- [63] Dahl EL, Rosenthal PJ. Multiple antibiotics exert delayed effects against the *Plasmodium falciparum* apicoplast. *Antimicrob Agents Chemother* 2007;51:3485–90. doi:10.1128/AAC.00527-07.
- [64] Jiménez-díaz MB, Ebert D, Salinas Y, Pradhan A, Lehane AM, Endsley AN, et al. (+)-SJ733, a clinical candidate for malaria that acts through ATP4 to induce rapid host-mediated clearance of *Plasmodium*. 2014. doi:10.1073/pnas.1414221111.
- [65] Handelman GJ, Levin NW. Red cell survival: relevance and mechanism involved. *J Ren Nutr* 2010;20:S84–8. doi:10.1053/j.jrn.2010.06.007.

- [66] Varlet-Marie E, Guiraudou M, Fedou C, Raynaud de Mauverger E, Durand F, Brun JF. Nutritional and metabolic determinants of blood rheology differ between trained and sedentary individuals. *Clin Hemorheol Microcirc* 2013;55:39–54. doi:10.3233/CH-131688.
- [67] Jenkins DJA, Kendall CWC, Nguyen TH, Teitel J, Marchie A, Chiu M, et al. Effect on hematologic risk factors for coronary heart disease of a cholesterol reducing diet. *Eur J Clin Nutr* 2007;61:483–92. doi:10.1038/sj.ejcn.1602551.
- [68] Clapp KM, Ellsworth ML, Sprague RS, Stephenson a H. Simvastatin and GGTI-2133, a geranylgeranyl transferase inhibitor, increase erythrocyte deformability but reduce low O(2) tension-induced ATP release. *Am J Physiol Heart Circ Physiol* 2013;304:H660–6. doi:10.1152/ajpheart.00635.2012.
- [69] Forsyth AM, Braunmüller S, Wan J, Franke T, Stone HA. The effects of membrane cholesterol and simvastatin on red blood cell deformability and ATP release. *Microvasc Res* 2012;83:347–51. doi:10.1016/j.mvr.2012.02.004.
- [70] Steck TL. Cross-linking the major proteins of the isolated erythrocyte membrane. *J Mol Biol* 1972;66:295–305. doi:10.1016/0022-2836(72)90481-0.
- [71] WHO. Determination of Parasitemia n.d.:1–4.
- [72] Loria P, Miller S, Foley M, Tilley L. Inhibition of the peroxidative degradation of haem as the basis of action of chloroquine and other quinoline antimalarials. *Biochem J* 1999;339 ( Pt 2):363–70. doi:10.1042/0264-6021:3390363.
- [73] Nuchsongsin F, Chotivanich K, Charunwathana P, Fausta OS, Taramelli D, Day NP, et al. Effects of malaria heme products on red blood cell deformability. *Am J Trop Med Hyg* 2007;77:617–22. doi:77/4/617 [pii].
- [74] Meshnick SR, Yang YZ, Lima V, Kuypers F, Kamchonwongpaisan S, Yuthavong Y. Iron-dependent free radical generation from the antimalarial agent artemisinin (qinghaosu). *Antimicrob Agents Chemother* 1993;37:1108–14. doi:10.1128/AAC.37.5.1108.
- [75] Huang S, Amaladoss A, Liu M, Chen H, Zhang R, Preiser PR, et al. In vivo splenic clearance correlates with in vitro deformability of red blood cells from Plasmodium yoelii-infected mice. *Infect Immun* 2014;82:2532–41. doi:10.1128/IAI.01525-13.
- [76] Spillman NJ, Allen RJW, Kirk K. Na<sup>+</sup> extrusion imposes an acid load on the intraerythrocytic malaria parasite. *Mol Biochem Parasitol* 2013;189:1–4. doi:10.1016/j.molbiopara.2013.04.004.
- [77] Kuzman D, Znidarcic T, Gros M, Vrhovec S, Svetina S, Zeks B. Effect of pH on red blood cell deformability. *Pflugers Arch* 2000;440:R193–4.

- [78] White NJ, Pukrittayakamee S, Phyo AP, Rueangweerayut R, Nosten F, Jittamala P, et al. Spiroindolone KAE609 for Falciparum and Vivax Malaria. *N Engl J Med* 2014;371:403–10. doi:10.1056/NEJMoa1315860.
- [79] World Health Organisation. Management of severe malaria. 2012.
- [80] Pasvol G. The treatment of complicated and severe malaria. *Br Med Bull* 2005;75-76:29–47. doi:10.1093/bmb/ldh059.
- [81] Ashley E a, Dhorda M, Fairhurst RM, Amaratunga C, Lim P, Suon S, et al. Spread of Artemisinin Resistance in Plasmodium falciparum Malaria. *N Engl J Med* 2014;371:411–23. doi:10.1056/NEJMoa1314981.
- [82] Phu NH, Tuan PQ, Day N, Mai NTH, Chau TTH, Chuong L V, et al. Randomized controlled trial of artesunate or artemether in Vietnamese adults with severe falciparum malaria. *Malar J* 2010;9:97. doi:10.1186/1475-2875-9-97.
- [83] Karunajeewa H a, Mueller I, Senn M, Lin E, Law I, Gomorrai PS, et al. A trial of combination antimalarial therapies in children from Papua New Guinea. *N Engl J Med* 2008;359:2545–57. doi:10.1056/NEJMoa0804915.